This Dissertation Committee for Bradley Allen Rowland
certifies that this is the approved version of the following dissertation:

COMPLEX QUANTUM TRAJECTORIES FOR BARRIER SCATTERING

Committee:

Robert E. Wyatt, Supervisor

Dmitri Makarov

Graeme Henkleman

Oscar Gonzalez

Kent Milfeld

COMPLEX QUANTUM TRAJECTORIES FOR BARRIER SCATTERING

by

Bradley Allen Rowland, B.S.; B.S.; M.A.

Dissertation

Presented to the Faculty of the Graduate School of
the University of Texas at Austin
in Partial Fulfillment
of the Requirements
for the Degree of

Doctor of Philosophy

The University of Texas at Austin
December 2007

Dedication

This dissertation is dedicated to Dr. Robert E. Wyatt, in honor of his Festschrift this year, his outstanding contributions to science, and for his tolerance, patience, and humanity.

Acknowledgements

I will begin by thanking my family, who have always been there for me, and encouraged me to constantly distinguish myself. In particular my parents' love and support have made sure that I had the opportunities to pursue my educational goals, and for that I'm eternally grateful. I would specifically like to thank my brother, who I have grown closer to over these years.

I would also like to thank the Wyatt Group: Lucas, Chia-Chun, and Julianne. Each of you have been very helpful during this experience. I wish you all the best of luck in your various endeavors, but I know you will not need it. I must also recognize Dr. Wyatt, whose patience, acceptance, and mentoring have meant the world to me.

My fellow graduate students: my ever prescient counselor (now Dr.) Thomas, Jesse, Mychel, the (unfortunately) defunct Physical Chemistry Dinner Group, and my favorite Yankee Emily. Thank you for the brilliant discussions, the adventures, the fine cuisine and beverage, and, of course, the friendship!

And finally, but certainly not lastly, I must recognize my closest friends, who have been there for me over these years through thick and thin. Again Dr. Thomas makes the list as perhaps my best friend thorough these years. I cannot forget Krista, who went through the trials and tribulations of graduate school (and Atlanta) and knew firsthand what was up. I'll never forget Ben and that wild road trip we took out to the Rose Bowl in 2004! And Michael, who has seen me through my whole time here at UT, a fellow explorer, and my dear friend, I thank you.

COMPLEX QUANTUM TRAJECTORIES FOR BARRIER SCATTERING

Publication No. ___________

Bradley Allen Rowland, Ph.D.
The University of Texas at Austin, 2007

Supervisor: Robert E. Wyatt

We have directed much attention towards developing quantum trajectory methods which can accurately predict the transmission probabilities for a variety of quantum mechanical barrier scattering processes. One promising method involves solving the complex quantum Hamilton-Jacobi equation with the Derivative Propagation Method (DPM). We present this method, termed complex valued DPM (CVDPM(n)). CVDPM(n) has been successfully employed in the Lagrangian frame to accurately compute transmission probabilities on 'thick' one dimensional Eckart and Gaussian potential surfaces.

CVDPM(n) is able to reproduce accurate results with a much lower order of approximation than is required by real valued quantum trajectory methods, from initial wave packet energies ranging from the tunneling case (E_o = 0) to high energy cases (twice the barrier height). We successfully extended CVDPM(n) to two-dimensional problems (one translational degree of freedom representing an Eckart or Gaussian barrier coupled to a vibrational degree of freedom) in the Lagrangian framework with great success. CVDPM helps to explain why barrier scattering from “thick” barriers is a much more well posed problem than barrier scattering from “thin” barriers. Though results in these two cases are in very good agreement with grid methods, the search for an appropriate set of initial conditions (termed an ‘isochrone) from which to launch the trajectories leads to a time-consuming search problem that is reminiscent of the root-searching problem from semi-classical dynamics. In order to circumvent the isochrone problem, we present CVDPM(n) equations of motion which are derived and implemented in the arbitrary Lagrangian-Eulerian frame for a metastable potential as well as the Eckart and Gaussian surfaces. In this way, the isochrone problem can be circumvented but at the cost of introducing other computational difficulties. In order to understand why CVDPM may give better transmission probabilities than real valued counterparts, much attention we have been studying and applying numerical analytic continuation techniques to visualize complex-extended wave packets as well as the complex-extended quantum potential. Numerical analytic continuation techniques have also been used to analytically continue a discrete real-valued potential into the complex plane for CVDPM with very promising results.

Table of Contents

List of Tables

List of Figures

Chapter 1: An Introduction to Quantum Trajectories and the Complex Quantum Hamilton-Jacobi Equation

I. Introduction

A. David Bohm and the Quantum Potential

David Bohm was a professor of physics at Princeton University when he taught a quantum mechanics course which gave birth to his classic text *Quantum Theory*[1]. The first hand experience of trying to explain (or even to understand) the subtle details of the quantum theory left Bohm with a desire to recast quantum mechanics into a form analogous to the classical mechanics based upon Newton's equations. In 1952 he published two papers[2,3] which seemed to achieve this goal, but not without introducing a non-local potential into the equations of motion. Bohm's work can be seen as an extension upon the much earlier pilot wave formulation of quantum mechanics as provided by Madelung[4] and de Broglie[5].

Bohm began his analysis with the assumption that the complex-valued wave function could be expressed in polar form (in one spatial dimension),

$$\Psi(x,t) = R(x,t)e^{\frac{iS(x,t)}{\hbar}} = e^{C(x,t)+\frac{iS(x,t)}{\hbar}}, \tag{1.1}$$

where *R(x,t)* and *S(x,t)* represent the real-valued amplitude and action functions, respectively. The amplitude can also be recast into exponential form, where *C(x,t)* will be a real-valued quantity. This is advantageous in the case where the density of the wave function is best expressed as the exponential of a polynomial (for example, *C(x,t)* for a

Gaussian will be a quadratic polynomial). Substituting this into the time-dependent Schrödinger equation (TDSE),

$$i\hbar\frac{\partial\psi(r,t)}{\partial t}=\frac{-\hbar^2}{2m}\nabla^2\psi(r,t)+V(r,t)\psi(r,t), \tag{1.2}$$

and separating the real and imaginary parts yields a pair of equations. The first equation governs the evolution of the density and can be cast into a conservative form,

$$\rho=\exp(2C)=R^2,$$

$$\frac{\partial\rho}{\partial t}=-\nabla\cdot(\rho v), \tag{1.3}$$

where v is defined (in the Lagrangian framework) by the de Broglie guidance condition,

$$v=\frac{1}{m}\nabla S(x,t), \tag{1.4}$$

and ρ is the given density along the trajectory. The second equation obtained is a variant of the Hamilton-Jacobi equation known as the quantum Hamilton-Jacobi equation. This equation governs the evolution of the action function *S(x,t).* The action function constantly updates the position and momentum of the trajectory using equation (1.4). This equation is given as

$$-\frac{\partial S(x,t)}{\partial t}=\frac{1}{2m}\nabla S(x,t)\cdot\nabla S(x,t)+V(x,t)+Q(x,t)\,, \tag{1.5}$$

where

$$Q(x,t)=-\frac{\hbar^2}{2m}\frac{\nabla^2\rho^{\frac{1}{2}}}{\rho^{\frac{1}{2}}}\,, \tag{1.6}$$

represents a non-local quantum potential. These equations have a structural similarity to equations governing fluid flow. For these reasons, this approach to quantum mechanics has been termed as the quantum hydrodynamic formulation (quantum hydrodynamic equations of motion (QHEM)). Holland[6] has provided much interpretation and definitive insight into the workings of QHEM in his excellent book *The Quantum Theory of Motion*[7].

Equations (1.3) and (1.5) introduce a "hidden variable" into the quantum mechanical scheme through the quantum potential. This term represents all the quantum effects observed in a system. An analysis of equation (1.6) shows that the quantum potential is proportional to the curvature of the amplitude function. A greater curvature corresponds to a larger quantum potential at that point (it is a measure of the curvature-dependent stress). For example, a one dimensional Gaussian on a zero potential ramp will diffuse into space over time. The quantum potential offers an explanation for this, as the curvature of the Gaussian function imparts a kinetic energy which serves to spread the Gaussian out. As the curvature tends to zero as the Gaussian flattens out the kinetic energy will correspondingly decrease, thus slowing the spreading.

The appearance (and scaling) of the quantum potential by a factor of ρ serves three interesting purposes. The first is that the quantum potential is invariant to scaling changes in ρ. Secondly, the appearance of ρ in the quantum potential introduces a dependence upon the initial wave packet into the dynamical evolution. Finally, the inclusion of this factor in the denominator makes for interesting behavior around poles. Nodes are defined in quantum theory as spatial points at which the amplitude of the wave function goes to zero. At these points, it is seen that the quantum potential would approach infinity and thus will make the equations ill behaved in those regions[8] (it is divergent). It should be noted that the polar *ansatz* of the wave function given in equation (1.1) with not be valid at the precise location of a node (as the density goes to zero at a node), but may still approximate the wave packet well *near* the node.

Inclusion of this quantum potential into the quantum Hamilton-Jacobi equation serves to introduce quantum effects along a classical trajectory. Note that no approximation is made; any system evolved according to these non-linear equations will have the inclusion of full quantum effects. It is important to note that the effects of non-locality are introduced through the use of spatial derivatives. Quantum Mechanics has traditionally been held as a non-local theory, but an examination of the TDSE does not readily reveal this fact. It was Bohm's insights that explicited the source of the non-locailty in the Schrödinger equation. Higher-order derivatives, in effect, incorporate information from surrounding local points, whereas a local force is only concerned with the information specifically at the point of interest (for example, in the TDSE the kinetic energy operator measures the curvature of the evolving wave packet and is able to account for the development of nodes at distant points). To see this, consider using finite differencing schemes to approximate derivatives. While maintaining the order of the differencing, increasing the degree of the derivative (i.e. from first to second) necessitates functional evaluations at more and more points in the domain. The incorporation of these points serves to draw in information from all other points.

One further point of mention—the Bohmian no-crossing rules[8]. Bohm's equations show that there are two no-crossing rules that Bohmian trajectories *must* obey. The first (derived from equation (1.3)) states that no two trajectories can cross in space-time. The second states that trajectories cannot pass through nodes. The reason for this is easy to see—as a trajectory approaches a node, the density carried by that trajectory will go to zero. After passing this node, the trajectory will have zero density and hence will be a 'ghost' trajectory which can be disregarded.

B. Synthetic Approaches to the QHEM

Quantum wave packet dynamics are of interest to chemical physicists, as they can be used to model photodissociation and femtochemical processes[9]. As all of chemistry, from biochemical reactions to the synthesis of new materials, is dependent upon the laws of quantum mechanics, and these problems are treated by solving the TDSE (equation (1.2)) with the appropriate potential energy surface with traditional methods—including fixed grid discretization (Eulerian), the pseudo-spectral method (PSM), and basis function expansions[10]. In problems with many degrees of freedom, numerical solutions to the TDSE may not possible. Traditional solutions to the TDSE suffer from many other deficiencies as well. Large grids (or basis sets) may need to be initialized in finite difference solutions of the TDSE, although there may not be anything of interest in regions of the grid (for example, when computing barrier transmission probabilities, the initial wave packet will be confined to one side of the barrier, while in the transmitted region there will be no density. We must still initialize and update densities on the whole grid, however). Grids also can suffer from boundary effects that may require the use of dampening potentials at the edges (if not handled properly, as the transmitted wave packet density approaches the edge of the grid there can be density reflected back to the reaction region which causes numerical instabilities). There is also the problem of exponential scaling with dimensionality with these methods.

One of the ways of handling these difficulties that has been examined recently are quantum trajectory methods[8]. Based on the prior work of David Bohm (discussed above), quantum trajectory methods require no grids, basis sets, or functional expansions. Results show that quantum trajectories scale linearly with the number of trajectories rather than exponentially by dimension as in traditional methods. The first viable quantum trajectory method (QTM) was introduced in 1999 by Lopreore and Wyatt[11]. In QTM, a correlated ensemble of trajectories are evolved in the Lagrangian frame (the grid points travel along at the velocity of the probability fluid). Spatial derivatives of the evolving wave packet are used to compute the quantum potential on the fly, thus allowing for a synthetic method. Because the trajectories are Lagrangian, there is no expectation that they should maintain an ordered grid as the solution evolves; this presents a difficulty as pseudospectral or finite difference methods employed to compute numerical derivatives must be founded on a regularly spaced grid. In order to circumvent this difficulty, an approach known as the Moving Weighted Least Squares method[8] (MWLS) is used with great success. Unfortunately, one of the main drawbacks to QTM is the appearance of nodes—if a node appears in the evolving wave packet, the calculation will come to an abrupt end as trajectories cannot pass through a node (the second of Bohm's no-crossing rules).

QTM has been extensively studied and applied to multidimensional dissociation and reactive scattering problems[12-14]. Because the node problem is very noxious to QTM, Babyuk and Wyatt have worked on addressing the node problem (through the use of the Covering Function Method)[15,16], using arbitrary Lagrangian-Eulerian (ALE) methods (which allow complete control over trajectory path) to steer trajectories away from developing nodes (another benefit to ALE methods is that one can maintain an ordered grid by which to compute traditional numerical derivatives and thus bypass the MWLS), A number of methods have been recently developed to deal with or to circumvent this problem (for example, see chapter 15 in reference 8). An alternative formulation known as Quantum Fluid Dynamics (QFD) was introduced by Rabitz and co-workers[17] around this same time.

For *non-stationary problems* where the wave function is *not known* in advance, there have been significant developments on the use of *real-valued quantum trajectories* for solving the QHJE for the action function. An alternative approach to the QTM, the derivative propagation method[18-25] (DPM), was developed by Trahan, Hughes, and Wyatt[18] as an alternative way to solve the quantum hydrodynamic equations by propagating *individual* quantum trajectories (as opposed to the ensemble required by QTM) in real-valued configuration space. Starting with a polar form for the wave function $\psi(x,t)=\exp\left(C(x,t)+iS(x,t)/\hbar\right)$, one can derive equations of motion for the spatial derivatives of the exponential amplitude $C(x,t)$ and action $S(x,t)$ functions. Instead of computing numerical derivatives for an evolving wave packet (as in QTM), DPM actually propagates the derivatives of the *C(x,t)* and *S(x,t)* fields themselves. This version of DPM, known as real-valued DPM (RVDPM(n)—we will also refer to this method as ‘Bohmian DPM’), was successfully extended to the evolution of phase space distribution functions[19,20,25], dissipative barrier scattering[21], and multidimensional barrier scattering problems[24].

The DPM, unlike QTM, is an *approximate* formulation of the quantum hydrodynamic equations of motion. The constraining factors on the quality of a QTM calculation are numerical in nature (through MWLS). By treating these numerical errors carefully one will obtain a solution that will be very close to the solution obtained by traditional methods (grid, pseudo-spectral, basis function expansions, etc.). By contrast, DPM consists of *approximate* equations of motion, and it will be seen that increasing the order of *real-valued* DPM does not necessarily lead to desired convergence properties. Of particular note is that Bohmian DPM itself does not provide highly accurate transmission probabilities for “thin” barrier scattering problems[26].

The DPM was extended to phase-space Wigner trajectories evolving under various master equations (Liouville, Wigner-Moyal, Caldeira-Leggett)[27-30] and dissipative systems[31, 32]. These master equations are given in Liouville (1.7), Wigner-Moyal (1.8), Klein-Kramers (1.9), and Calderia-Leggett (1.10), along with the Wigner transform[33] (1.11), which transforms wave packets in configuration space to a distribution in phase space.

$$\frac{\partial W}{\partial t} = -\frac{p}{m}\frac{\partial W}{\partial x} + \frac{\partial V}{\partial x}\frac{\partial W}{\partial p} \tag{1.7}$$

$$\frac{\partial W}{\partial t} = -\frac{p}{m}\frac{\partial W}{\partial x} + \frac{\partial V}{\partial x}\frac{\partial W}{\partial p} - \frac{\hbar^2}{24}\frac{\partial^3 V}{\partial x^3}\frac{\partial^3 W}{\partial p^3} + \frac{\hbar^4}{1920}\frac{\partial^5 V}{\partial x^5}\frac{\partial^5 W}{\partial p^5} + O(\hbar^6) \tag{1.8}$$

$$\frac{\partial W}{\partial t} = -\frac{p}{m}\frac{\partial W}{\partial x} + \frac{\partial V}{\partial x}\frac{\partial W}{\partial p} + \gamma \frac{\partial}{\partial p}\left[p + mk_B T \frac{\partial}{\partial p} \right] W \tag{1.9}$$

$$\frac{\partial W}{\partial t} = -\frac{p}{m}\frac{\partial W}{\partial x} + \frac{\partial V}{\partial x}\frac{\partial W}{\partial p} - \frac{\hbar^2}{24}\frac{\partial^3 V}{\partial x^3}\frac{\partial^3 W}{\partial p^3} + \gamma \frac{\partial (pW)}{\partial p} + \gamma m k_B T \frac{\partial^2 W}{\partial p^2} \tag{1.10}$$

$$W(x,p,t) = \frac{1}{2\pi\hbar}\int \psi^*\left(x + r/2, t\right)\psi\left(x - r/2, t\right) e^{ipr/\hbar} dr \tag{1.11}$$

Low order DPM was shown to very accurately predict transmission probabilities in barrier scattering calculations in certain cases (when the width of the scattering potential barrier is greater than the width of the initial wave packet). However, very high orders must be used in order to obtain accurate results around nodes, and this presents numerical problems. By combining the initial value representation with the DPM, Bittner[34] was able to make observations concerning the utility of DPM with regards to certain types of problems. The DPM has been extended to high-dimensionality (10 degrees of freedom for the quadratic DPM) barrier scattering problems[24].

It can be shown that the DPM is a generalization of earlier studies conducted by Heller[35] on the use of frozen or thawed Gaussians in time-dependent semi-classical scattering processes, known as Gaussian Wave Packet Dynamics (GWPD). The difference, however, is that the DPM can approximate the *C* and *S* fields along *each* trajectory to quadratic and higher orders whereas Heller's studies employed equations of motion for parameters in a Gaussian which approximated the global wave packet. Several methods which employ multiple Gaussians propagating along classical trajectories will also be mentioned. Shalashilin and Child have developed a method which employs multiple non-orthogonal traveling frozen Gaussians which are sampled by a Monte Carlo procedure[36-38]. This method has been applied to tunneling problems[37]. In addition, Martinez et al[39-41] have developed the multiple spawning method wherein additional frozen Gaussians following classical trajectories are used to augment the basis set where they are needed, to account for tunneling and non-adiabatic transitions. Much earlier studies by Metiu et al[42] involved expansion of the wave packet in a swarm of thawed traveling Gaussians.

C. Other Methods and Points of View

There has been recent work on extending quantum trajectories to problems with many degrees of freedom. Kendrick[43] used arbitrary Lagrangian-Eulerian trajectories and artificial viscosity to stabilize the propagating wave packet in barrier scattering processes. This work was subsequently extended to two-dimensional problems by Pauler and Kendrick[44], and eventually to multi-dimensional problems as well[45]. ALE methods have also been employed in the node coping problem in the QTM (see chapter 7 of reference 8 for discussion and results).

Poirier and co-workers have also done much work on the bipolar-decomposition of the wave function in the reconciliation of semi-classical dynamics with Bohmian dynamics[46-48]. Rassolov and Garashchuk[49] have introduced an approximate linearized quantum potential into the hydrodynamic equations of motion. This served to stabilize the wave function around nodes. Even greater stability was obtained by introducing a mixed polar-coordinate space representation of the wavefunction[50]. This was successfully extended to non-adiabatic systems[51].

Alternatively, the quantum hydrodynamic equations of motion can be obtained through a momentum-moment expansion of the Wigner function (equation (1.11)) in phase space. This work is based upon early studies conducted by Takabaysi[52]. He was the first to develop equations of motion for the Wigner function momentum moments. The momentum moments form an infinite hierarchy exhibiting both up-coupling to higher order equations as well as down-coupling to lower order equations. Burghardt and Cederbaum formulated quantum hydrodynamic equations of motions for mixed (and pure) states[53], as well as for coupled electronic states[54] in terms of the Wigner function momentum moments. This formulation has been extended to dissipative systems[55] as well. This is a most interesting route to the QHEM, as many subtle nuances can be gleaned from this formulation. For example, the approach of Burghardt and Cederbaum is applicable to both mixed and pure states. However, for pure states, the momentum moment expansion terminates at the second order, leaving two equations which are identical to the underlying equations in Bohmian mechanics.

D. Complex Quantum Trajectories

Complex-valued *classical* trajectories were introduced in the early years of quantum mechanics to deal with the “turning point” connection problem in WKB theory[56]. The extensive 1972 review by Berry and Mount[57] covered this and other developments in semiclassical theory. In 1987, Huber and Heller[58] generalized the earlier real valued version of Gaussian wave packet dynamics[35] to allow for the propagation of complex valued classical trajectories. When it comes to complex valued *quantum* trajectories, the developments are much more recent.

Recently, Goldfarb, Degani, and Tannor used the DPM to solve equations of motion for trajectories which had been extended to the *complex* plane[59]. This complex-extended DPM, denoted BOMCA, was shown to very accurately reproduce barrier transmission probabilities at *low orders*, even for the deep barrier tunneling case. These trajectories provide a method for solving the complex quantum Hamilton-Jacobi equation (QHJE), which is obtained from the Schrödinger equation through use of the exponential ansatz[2,3] for the wave function, namely $\psi(x,t) = \exp(iA(x,t)/\hbar)$. In this polar form for the wave function, $A(x,t)$, the complex valued action function, is the solution to the QHJE. Schrödinger himself recognized the necessity for a complex action function[60]. Assuming the *complex* de Broglie guidance condition, $p(z,t) = \partial S(z,t)/\partial t$, along with the dynamical equation $dz(t)/dt = p(z(t),t)/m$, we are led to trajectories evolving in phase space with *complex values* for both x (now *z*) and p (we will assume that the time remains real valued).

In contrast to many recent developments using real valued quantum trajectories, the use of *complex valued quantum trajectories* for solving the QHJE is at a much earlier stage of development. BOMCA was applied by Tannor et al to the one-dimensional scattering of a wave packet from an Eckart barrier[59]. Implementation of DPM at the second-order, denoted by CVDPM(2), involves the propagation of complex valued classical (2nd order) trajectories along which is transported an approximate quantum action function. In higher-order versions of CVDPM, the quantum trajectories are influenced by classical (local) forces and by quantum non-local forces. Perhaps the most interesting result of this study is that a very good approximation to the deep barrier tunneling probability is obtained with *classical* complex trajectories! Though not immediately recognized by Goldfarb, Degani, and Tannor[59], BOMCA trajectories are really just complex-valued DPM (CVDPM(n)) trajectories obtained by the application of the DPM to the complex quantum Hamilton-Jacobi equation[10].

E. Stationary States and Complex Trajectories

Assuming that $\psi(x,t)$ is known in advance (clearly, a major assumption), it is rather straightforward to analyze and plot quantum trajectories. Over the past five years, for the stationary state case, both John[61] and Yang[62-68] have independently provided informative analyses for the harmonic oscillator[61,62], one-dimensional barrier tunneling[61,63], hydrogen atom eigen-trajectories[64,65], an analysis of electron spin in the complex plane[66], and several other problems[67-69]. Yang's solutions, however, require an analytic form of the wave packet at each step and thus are only applicable to situations in which the exact quantum mechanical solution is known *a priori*.

A direct computational approach to the stationary state QHJE for both bound states and scattering problems, based upon use of the Möbius propagator and approximate boundary conditions (assumption of a specific approximate form in the deep-tunneling region), has been developed by Chou and Wyatt[70-72]. Recently, there has been interest in developing solutions to the complex-extended Hamilton Jacobi equation for quantum mechanical problems. For stationary states, John[61] introduced complex trajectories in his analysis of the Hamilton-Jacobi equation. Boiron and Lombardi[73] ran complex semi-classical complex trajectories in 1998 that were successfully tested for some analytic as well as numerical cases.

In a recent study by Chou and Wyatt[74], complex quantum trajectories were computed for both non-stationary and stationary state problems. For the free translating Gaussian wave packet and the coherent state in a harmonic oscillator potential, equations were derived for the isochrones. In addition, information transported by trajectories launched from isochrones was used to synthesize the time dependent wave function on the real axis. Two stationary state problems were also studied: excited states for the harmonic oscillator and scattering states for the Eckart potential. For the latter problem, the exact complex quantum trajectories were investigated, an unusual ‘channel’ structure was found for the total potential (the sum of the classical and quantum potentials), and some trajectories were found to spiral in toward point attractors in the barrier region.

F. Recent Developments with Synthetic Complex Trajectories

As stated in subsection B of this introduction, there have been many developments in the synthetic complex quantum trajectory problem. This work has come from two research groups: the Wyatt group at the University of Texas Austin, and the Tannor group at the Weizmann Institute, Israel. Goldfarb, Degani, and Tannor were the first to publish results for the DPM applied to the complex quantum Hamilton-Jacobi equation. This work was in particular very interesting as it showed that relatively good Eckart barrier scattering transmission probabilities could be obtained with very low orders of DPM (in fact, for *classically* propagating trajectories). They did not, however, provide necessary analysis, such as a convergence analysis for DPM, or any results to help in the implementation (such as the role of the complex potentials or a model for isochrone selection), or why it seems that classical complex trajectories can reproduce quantum information!

Rowland and Wyatt have recently published a paper[26] that addresses some of the questions unaddressed in the initial paper by the Tannor group. In this study, the CVDPM(n) was applied to both Eckart and Gaussian barrier scattering problems (in the Lagrangian frame) over a range of energies. The complex potential energy surfaces (both classical and quantum) are examined, properties of transmission isochrones are examined, the reason why classical complex trajectories can in fact reproduced quantum information is deduced, and the general relationship between RVDPM(n) and CVDPM(n) is described.

Wyatt and Rowland subsequently published another paper[75] detailing the extension of the CVDPM(n) to problems with two degrees of freedom—a translational coordinate (either Gaussian or Eckart barrier) and a vibrational mode, with a coupling parameter between them. In this study, the two-dimensional potential energy surfaces are plotted and analyzed, a model for the isochrone surface is given, and barrier transmission probabilities are compared for CVDPM(2) and CVDPM(3) trajectories as compared to solutions obtained through the numerical integration of the TDSE. Excellent results were obtained, and the extension of these methods to higher-dimensional problems seems highly promising.

In the three studies discussed above, the isochrone problem is the largest difficulty to efficient implementation of the CVDPM(n) in any dimension; a problem for which the Wyatt and Tannor groups have taken divergent approaches. The Tannor group approach to address the isochrone problem is termed ZEVCA[76]. Basically, what Tannor and co-workers have done is replaced the Lagrangian flow velocity with the *Eulerian* flow velocity (which is zero) in the CVDPM(n) equations of motion (see equations (2.26), (2.30), and (2.31) in the next chapter for the Eulerian equations). They then compute the wave function density as one point in the complex plane. The "trajectory" (this can hardly be defined as a trajectory as it does not move in space-time) never moves in this formulation, and this is the source of its deficiency. Because the trajectory is not allowed to move, the initial wave packet must be started *very* close to the maximum of the scattering barrier in order for there to be overlap in the initial conditions (starting the wave packet in the asympototic region of the barrier yields initial conditions of 0 and no propagation). In effect, one is required to run very high orders of CVDPM(n) for a very small subset of problems, and this limits the utility of ZEVCA in quantum dynamics.

Rowland and Wyatt, on the other hand, proposed dealing with the isochrone problem in the Lagrangian framework by introducing the concept of the *arbitrary Lagrangian-Eulerian* framework[77]. Instead of setting the flow velocity to the mass scaled action gradient, one is free to select whatever trajectory velocity one would like; this in effect allows complete control over the evolution of the trajectory in the complex plane. When coupled with the quantum mechanical flux, a very good method (termed ALECVDPM(n)) was introduced which gave very accurate transmission probabilities for the barriers studied in prior works. Current work in the Wyatt group involves extending the ALECVDPM(n) framework to the problems examined in Wyatt and Rowland's two-dimensional CVDPM(n) study[75].

Tannor and co-workers then published three subsequent papers: the first[78] dealt with the relationship between ZEVCA, CVDPM(n), and RVDPM(n) (which has been explored previously by Rowland and Wyatt), a very interesting study on isochrone branches[79] and the possibility that DPM trajectories *may* violate Bohm's no-crossing rule, and a paper[80] which explored the WKB theory in the context of crossing complex trajectories. Of the most direct interest is the paper which describes apparent violations of the no-crossing rule. Tannor and co-workers began to examine the reflected wave packet in the barrier scattering problem[79], and found that *multiple* trajectories originating from different isochrones in the complex plane could be arranged in a linear combination in such a way as to reproduce the reflected wave packet, including nodes! Unfortunately, they declined to present any model on how to properly combine the results from different isochrones, what effect higher orders of CVDPM(n) might have on trajectory branches, and why the no-crossing rule may be violated in this instance.

Recent work in the Wyatt group on synthetic quantum trajectories has had two focuses. First, David and Wyatt have submitted a study[81] which thoroughly analyzes the isochrone branches that appear for *both* the reflected and transmitted wave packets in the complex plane. Properties of these isochrones are deduced, it is show that features of the complex-extended initial wave packet affect isochrone behavior, and a predicative model is given for the transmitted isochrone branch. This work, in conjunction with Tannor's work on crossing trajectories, has spurred examination of the reflected wave packet and the role of the quantum potential in complex barrier scattering processes. Initial results show that the reflected wave packet can indeed be reconstructed from trajectories launched on different isochrones, but we have failed to develop a model for this process.

Because we would like to study the complex quantum potential, we need methods that can effectively extended data that is only given on the real axis (such as wave packet density). This has motivated us to study and implement various Numerical Continuation Methods (NACs). These methods have been used to visualize the complex quantum potential (which is distinct from the Bohm quantum potential) and the complex-extended wave packet. Further motivation for the development of these techniques is the fact that potentials for problems of interest to chemical physicists are not given in a nice analytic form; they are usually given in terms of discretized data sets and if these potentials are to be used in CVDPM(n) and the related family of methods they must be accurately continued off the real axis, in order to be able to update trajectory motion and density "on the fly".

II. General Outline of Dissertation

A. Dissertation Outline

Chapter 2 of this dissertation presents analysis and results for wave packet transmission in the one dimensional complex barrier scattering problem. In Subsection II the theory behind both RVDPM(n) and CVDPM(n) is explored. Subsection III discusses the Eckart and Gaussian potentials and their extension into the complex plane. Subsection IV details the comparison of RVDPM(n) to CVDPM(n) for transmission probabilities. The concept of the *isochrone* is introduced in this subsection, as well as an analysis of both classical and quantum complex trajectories. The chapter closes with Subsection V, a summary of results.

Chapter 3 discusses the extension of complex trajectory methods to two dimensional systems. Subsection II will derive the equations of motion for the two dimensional problem, while subsection III discusses the model potentials (which have one translational degree of freedom coupled to a vibrational degree of freedom) and the two-dimensional complex extension of the initial wave packet. Subsection IV discusses myriad results, from arrival times for transmitted trajectories to a model for isochrones, and results concerning barrier scattering in “thick” versus “thin” cases. Finally, subsection V closes the chapter with conclusions.

Chapter 4 will examine the use of complex valued Arbitrary Lagrangian-Eulerian trajectories in the barrier transmission problem studied in chapter 2. Subsection II details the theory involved in deriving the equations of motion for arbitrary Lagrangian-Eulerian complex quantum trajectories. Equations for computing the probability flux are provided. Subsection III details the model potentials, including the Metastable Well, while subsection IV presents results for constant velocity rectilinear trajectories. By employing the ALE framework, we can exert precise control over where the trajectories go in the complex plane. The benefits of this are explored in this subsection. The chapter concludes with subsection V.

Chapter 5 will present very recent results concerning the use of numeric analytic continuation (NAC) methods to simulate complex valued potentials as obtained from real valued discrete data (as would be obtained from DFT calculations). Subsection I details recent work in this area, with particular attention paid to various NAC techniques, their application in extending the potential surfaces into the complex plane, and running ALECVDPM(n) trajectories on numerical potentials. The numeric extension of the complex quantum potential is also presented to further understand complex trajectory methods. Subsection II discusses future directions for the work, including recent results concerning isochrone branches. The chapter closes with a summary of results.

A single appendix is presented at the end of this dissertation. Appendix A contains a proof that the CVDPM(n) equations of motion reduce to the RVDPM(n) equations of motion on the real axis. This proof can be found in a recent publication by Rowland and Wyatt[26], while an alternative derivation can be found by Tannor and co-workers[78].

Chapter 2: Comparison and Analysis of Both Real and Complex Quantum Trajectories for the Transmitted Wave packet in Barrier Scattering Problems

I. Introduction and Outline

A. Motivation

Quantum wave packet dynamics can provide considerable insight into problems of interest in chemical physics such as photodissociation, barrier scattering, and femtochemical processes[9]. Traditionally, quantum wave packet dynamics calculations involved the solution of the time-dependent Schrödinger equations (TDSE) through the use of fixed grids or basis set expansions. Recently, much work has been focused upon the development and application of non-local *quantum* trajectory methods to these problems[8].

RVDPM(n) has been successfully extended to many problems (see chapter 10 in reference 8), and yet it has many drawbacks, as discussed in chapter 1. In general, there is no way to predict what the best order of RVDPM(n) would be for a problem. RVDPM(n) does not accurately reproduce reflected wave packet results for some barriers, and has difficulty in problems for which the barrier is "thin" by comparison to the width of the initial wave packet. The strengths of RVDPM(n), however, lie in the parallelizability of the trajectories, the good transmission probabilities that can be obtained for some barriers, and its ease of extension to multi-dimensional problems.

Recently, Goldfarb and co-workers[59] have reported an extension of the DPM into the complex plane. In their initial paper, they reported excellent transmission probabilities for the Eckart barrier scattering problem from *classical* complex trajectories for the deep barrier tunneling problem! This extension, which is just an application of the DPM to the complex quantum Hamilton-Jacobi equation, has been termed BOMCA by the Tannor group, CVDPM(n) by the Wyatt group[26]. Goldfarb and co-workers did not give any analysis of this new method; they presented probabilities and errors only. There was no discussion of the imaginary potential energy, the complex extended wave packet, how the RVDPM(n) corresponded to the CVDPM(n), or how it was possible that a classical trajectory could reproduce quantum results!

Naturally, this extension to the complex plane (and the good transmission probabilities) came as a surprise. We commenced a study in order to answer some of the above questions, and we found some very interesting results in cases where complex trajectories had been applied to other problems (Yang's work is of particular note). In our study, both RVDPM(n) and CVDPM(n) were applied to model barrier scattering problems employing either an Eckart or Gaussian barrier and an initial Gaussian wave packet. The initial wave packets in these calculations will have either zero initial energy, denoting a deep barrier tunneling problem (DT), or an initial energy equal to the barrier height, which is termed high-energy (HE). Various properties of CVDPM(n) trajectories will then be examined. Of concern here is the method by which the appropriate initial conditions are chosen, the complex-extension and influence of the potentials, and the behavior of CVDPM(n) trajectories in the complex plane for several orders of DPM.

B. Outline of Chapter

In subsection II, relevant equations of motion for both RVDPM(n) and CVDPM(n) trajectories will be presented and discussed. The derivative propagation method is introduced. Subsection III explores various implementation issues, computational methods, and the model Eckart and Gaussian potentials will be discussed. This subsection contains an analysis of the complex extended Eckart and Gaussian potentials. The initial wave packet in the complex plane is presented. Subsection IV presents relevant results for both DT and HE scattering from Eckart and Gaussian barriers, as well as analysis of some complex quantum trajectories. In particular, analyses of the forces, kinetic energy, and complex potential are presented. Finally, concluding remarks will be given in subsection V.

II. Theory

A. Real Valued DPM

In this section, the real-valued DPM equations of motion will be derived and discussed in both the Eulerian and Lagrangian frames. A discussion of the conservation of weights on real-valued quantum trajectories will follow. Equations for CVDPM(n) will be derived and discussed in Section II B, in both the Eulerian and Lagrangian frames. Finally, this section will close with an analysis of CVDPM(2) trajectories.

Equations of motion for real-valued quantum trajectories are obtained by first performing a polar decomposition of the wave function, via the *ansatz*

$$\Psi(x,t) = \exp\left(C(x,t) + \frac{i}{\hbar} S(x,t) \right). \tag{2.1}$$

In equation (2.1), $S(x,t)$ is the real-valued action function, and $C(x,t)$ is a real-valued function which is related to wave function density via $\rho(x,t) = |\psi(x,t)|^2 = \exp(2C(x,t))$. Substituting equation (2.1) into the time-dependent Schrödinger equation (TDSE) and separating the resulting equation into real and imaginary parts yields two coupled equations. The first is the quantum Hamilton-Jacobi equation

$$\frac{\partial S(x,t)}{\partial t} + \frac{1}{2m} S_1^2 + Q_B + V = 0, \tag{2.2}$$

where Q_B represents the non-local Bohm quantum potential

$$Q_B = -\frac{\hbar^2}{2m}\left[C_2 + C_1^2\right]. \tag{2.3}$$

The second equation is the continuity equation,

$$\frac{\partial C(x,t)}{\partial t} + \frac{1}{2m}\left[S_2 + 2C_1 S_1\right] = 0. \tag{2.4}$$

In all equations, subscript notation is used for spatial partial derivatives.

$$\frac{\partial^n F(q,t)}{\partial q^n} = F_n, \tag{2.5}$$

where $q = x$ for real-valued trajectories and $q = z$ for complex-valued trajectories. These equations are cast in the Eulerian form (the grid points are stationary).

In order to obtain equations of motion for trajectories, it will be necessary to transform the Eulerian equations into the Lagrangian frame via the transform

$$\frac{d}{dt} = \frac{\partial}{\partial t} + v\frac{d}{dq}, \tag{2.6}$$

where v is the flow velocity. Taking the de Broglie guidance condition, $p = S_1$, the flow velocity becomes

$$v = \frac{S_1}{m}. \tag{2.7}$$

Substituting equations (2.2) and (2.4) into equation (2.6) and using equation (2.7) yields Lagrangian equations for the evolution of the action,

$$\frac{dS(x,t)}{dt} = \frac{1}{2m} S_1^2 - V + \frac{\hbar^2}{2m}\left[C_2 + C_1^2\right], \tag{2.8}$$

and the C-amplitude,

$$\frac{dC(x,t)}{dt} = -\frac{1}{2m} S_2. \tag{2.9}$$

One way to propagate the trajectories described in equations (2.8) and (2.9) is to employ the quantum trajectory method. In essence, this involves the propagation of a correlated ensemble of trajectories. At each time step, fitting techniques (such as least squares) can be employed to compute the spatial derivatives of the S and C functions in order to update the trajectory position and density. In this way, quantum non-locality is explicitly introduced into the trajectory dynamics. However, as the trajectories evolve, any semblance of an ordered grid quickly disappears. While successful in a variety of problems, QTM is usually computationally intensive.

Alternatively, the DPM can be used to derive an exact set of equations of motion for the spatial derivatives of the C and S functions. The spatial derivatives of S and C will be propagated along *individual trajectories*, and the need for fitting is removed. The

DPM equations are obtained by spatially differentiating both sides of each Eulerian equation, equations (2.2) and (2.4):

$$\frac{\partial S_1}{\partial t} = -\frac{1}{m} S_1 S_2 + \frac{\hbar^2}{2m}\left[C_3 + 2C_1C_2\right] - V_1, \tag{2.10}$$

and

$$\frac{\partial C_1}{\partial t} = -\frac{1}{2m}\left[S_3 + 2C_1S_2 + 2C_2S_1\right]. \tag{2.11}$$

These equations transform to the Lagrangian frame as

$$\frac{dS_1}{dt} = \frac{\hbar^2}{2m}\left[C_3 + 2C_1C_2\right] - V_1, \tag{2.12}$$

and

$$\frac{dC_1}{dt} = -\frac{1}{2m}\left[S_3 + 2C_1S_2\right]. \tag{2.13}$$

The first term on the right-side of equation (2.12) is the Bohm quantum force, $-\partial Q_B/\partial x$. Note that equations (2.12) and (2.13) exhibit both down-coupling to lower-order derivatives and up-coupling to higher-order derivatives, making these equations and ones for the higher-order derivatives an infinite but exact hierarchy. Eulerian equations for RVDPM(2) can be derived by taking the spatial derivative of equations (2.10) and (2.11):

$$\frac{\partial S_2}{\partial t} = -\frac{1}{m}\left(S_1S_3 + S_2^2\right) + \frac{\hbar^2}{2m}\left[C_4 + 2C_2^2 + 2C_1C_3\right] - V_2, \tag{2.14}$$

and

$$\frac{\partial C_2}{\partial t} = -\frac{1}{2m}\left[S_4 + 2C_1S_3 + 4C_2S_2 + 2S_1C_3\right]. \tag{2.15}$$

These equations transform to the Lagrangian frame as

$$\frac{dS_2}{dt} = -\frac{1}{m}S_2^2 + \frac{\hbar^2}{2m}\left[C_4 + 2C_2^2 + 2C_1C_3\right] - V_2, \tag{2.16}$$

and

$$\frac{dC_2}{dt} = -\frac{1}{2m}\left[S_4 + 2C_1S_3 + 4C_2S_2\right]. \tag{2.17}$$

Notice the up-coupling to higher-order derivatives in equations (2.16) and (2.17).

Equations (2.12), (2.13), (2.16), and (2.17) will constitute a *closed set* of equations if spatial derivatives of the C-amplitude and S of order greater than 3 vanish. Following this procedure, Lagrangian equations for any order of real-valued DPM can be obtained through the following infinite system of equations:

$$\frac{dC_n}{dt} = -\frac{1}{2m}\left[S_{2+n} + 2\left(C_1S_1\right)_n\right] + \frac{1}{m}S_1C_{1+n}, \tag{2.18}$$

and

$$\frac{dS_n}{dt} = -\frac{1}{2m}\left(S_1^2\right)_n + \frac{\hbar^2}{2m}\left[C_{2+n} + \left(C_1^2\right)_n\right] - V_n + \frac{1}{m}S_1S_{1+n}. \tag{2.19}$$

In order to make progress with the infinite hierarchy of equations, assume that the C and S functions are smooth enough to be approximated in the vicinity of a trajectory by polynomials,

$$C(\xi,t) = \sum_{k=0}^{K}\frac{1}{k!}c_k(t)\xi^k, \tag{2.20}$$

and

$$S(\xi,t) = \sum_{k=0}^{L}\frac{1}{k!}s_k(t)\xi^k, \tag{2.21}$$

where ξ denotes the displacement from a trajectory at time t. Assuming quadratic expansions ($K = L = 2$) for both C and S, substituting into equations (2.2), (2.4), (2.10), (2.11), (2.14), and (2.15), and letting $\xi \rightarrow 0$ gives six coupled equations which are exactly the same as equations (2.2), (2.4), (2.10), (2.11), (2.14), and (2.15), only these equations lack spatial derivatives of C and S greater than order 2. This shows that truncation of the derivative hierarchy is equivalent to assuming some level of polynomial smoothness for the C and S fields. Lagrangian equations for any RVDPM(n) can be obtained by working out the terms in equations (2.18) and (2.19) and setting to zero all spatial derivatives of S and the C-amplitude with orders greater than n.

A few comments can be made about RVDPM(n) trajectories. First, note that these trajectories can be computed *individually*, and the need for functional fitting has been circumvented by propagating the approximate spatial derivatives of C and S along each trajectory. However, due to the up-coupling to higher-order spatial derivatives in the derivative propagation equations, the quantum potential will rarely be exactly specified along the trajectory. Higher orders of RVDPM(n) bring in improved approximations to the quantum potential and allow the trajectory to ‘sense’ how the C and S fields are behaving in the vicinity of the trajectory. In this way, DPM can be thought of as introducing a *regional non-locality* around each propagating trajectory. However, because the equations of RVDPM(n) are usually truncated at low-order, the reach of this regional non-locality is limited. High-orders of RVDPM(n) are needed to allow distant features to affect the motion of the approximate quantum trajectory.

It is not necessary to propagate a large number of trajectories in a real-valued DPM calculation in order to obtain the transmission probability. The time-dependent transmission probability *P(t)* of a wave packet through a barrier can be obtained via

$$P(t) = \sum_{i,products} w_i(x_i(t),t), \tag{2.22}$$

where w_i represents the trajectory weight[82] defined as

$$w_i(x_i(t),t) = \rho(x_i(t),t)\delta x_i, \tag{2.23}$$

where δx_i represents a volume element. This weight is a conserved quantity[82], as required by the continuity equation, equation (2.9). Recasting the weights in terms of the *initial trajectory densities* yields

$$w_i(x_i(t),t) = w_i(x_i(0),0) = \rho(x_i(0),0)\delta x_i. \tag{2.24}$$

Substitution of equation (2.24) into equation (2.22) immediately shows that transmission probabilities can be computed only from the *initial* wave packet densities if one also knows which trajectories transmit through the barrier. As shown in Figure 1, there is a definite bifurcation point for each time such that trajectories initially launched from the right of the bifurcation point will be transmitted while trajectories launched from the left will be reflected. Integrating the probability density obtained from the initial Gaussian wave packet from this bifurcation point forward will yield an area which is equivalent to the transmission probability at that time, in accordance with equation (2.22). Only a few transmitted trajectories need to be evaluated in order to locate the bifurcation point.

B. Complex Valued DPM

Schrödinger himself recognized that the action S found in the Hamilton-Jacobi equation should be regarded as a complex quantity[60] (he was motivated to make this change in an effort to consolidate both S and ρ into a single function). Letting $z = x + iy$ represent a point in the complex plane, we can express the complex-valued wave function in terms of a complex action $A(z,t)$ via the *ansatz*

$$\Psi(z,t) = \exp\left(\frac{i}{\hbar} A(z,t)\right). \tag{2.25}$$

Inserting equation (2.25) into the time-dependent Schrödinger equation yields a single complex equation,

$$\frac{\partial A(z,t)}{\partial t} + \frac{1}{2m} A_1^2 + Q_C + U = 0, \tag{2.26}$$

Figure 1: Wave packet bifurcation and transmission probability

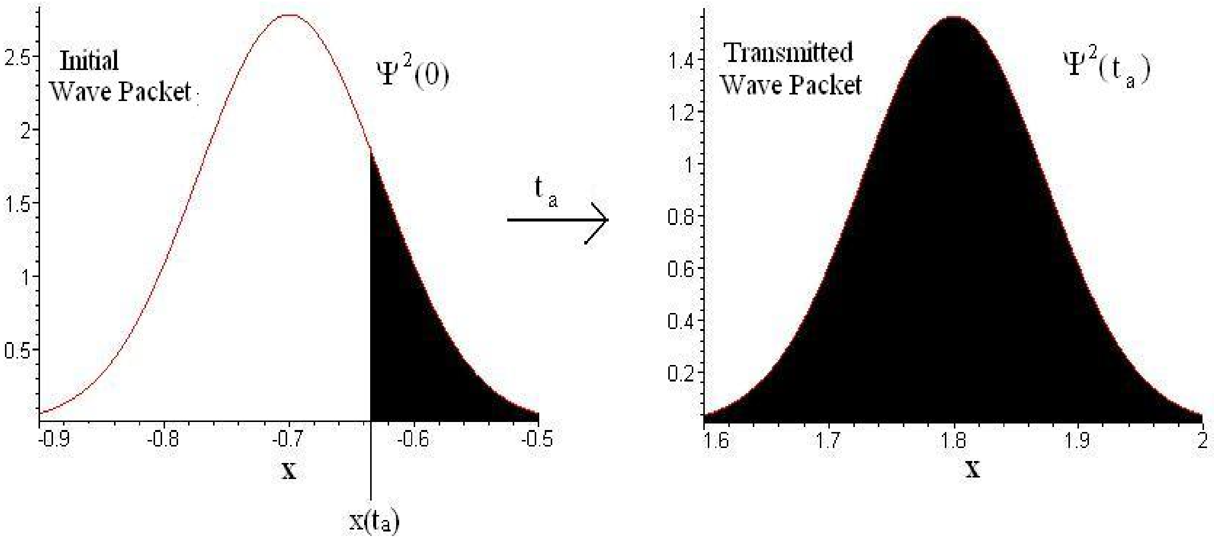

The integration of the initial Gaussian wave packet density from $x(t_a)$ forward yields an area which is equal to the transmitted probability density at time t_a. The shaded region of $\Psi^2(0)$ represents the starting location of all trajectories which have transmitted the barrier at the arrival time t_a.

which is a complex-version of the quantum Hamilton-Jacobi equation (For an introduction, see Sec. 4.2.3. in Tannor's text[10]). In this equation, Q_C represents a non-local *complex* quantum potential given by

$$Q_C = -\frac{i\hbar}{2m} A_2. \tag{2.27}$$

The de Broglie guidance condition, equation (2.7), is assumed valid, thus making the momentum complex. *U(z)* is the continuation of the potential to the complex plane. The Lagrangian form of the complex quantum Hamilton-Jacobi equation can be obtained by substituting equation (2.26) into equation (2.6) and employing the guidance condition, thus giving

$$\frac{dA(z,t)}{dt} = \frac{1}{2m} A_1^2 - U + \frac{i\hbar}{2m} A_2. \tag{2.28}$$

In effect, of the Lagrangian transformation allows grid points to travel along complex quantum trajectories. The time-dependent wave function evaluated along the trajectory is given by

$$\Psi(z,t) = \exp\left\{ \frac{i}{\hbar} \left[A(z_o,0) + \int_0^t \frac{dA(z,\tau)}{d\tau} d\tau \right] \right\}, \tag{2.29}$$

with *dA/dt* given by equation (2.28). The density along the trajectory can be obtained through the relation $\rho(z,t) = \exp(-2/\hbar\ \mathrm{Im}(A(z,t)))$.

The derivative propagation method will again be employed in order to approximately solve equation (2.26). Note that, as in the real-valued case, the evolution equation for *A* requires the first and second order spatial derivatives of *A* in order to evaluate the expression. Evolution equations for these functions can be obtained by taking the first and second spatial derivatives of equation (2.26),

$$\frac{\partial A_1}{\partial t} = -\frac{1}{m} A_1 A_2 + \frac{i\hbar}{2m} A_3 - U_1, \tag{2.30}$$

and

$$\frac{\partial A_2}{\partial t} = -\frac{1}{m}\left(A_2^2 + A_1 A_3\right) + \frac{i\hbar}{2m} A_4 - U_2. \tag{2.31}$$

Substituting equations (2.30) and (2.31) into equation (2.6) and employing the guidance condition gives equations of motion in the Lagrangian frame,

$$\frac{dA_1}{dt} = \frac{i\hbar}{2m} A_3 - U_1, \tag{2.32}$$

and

$$\frac{dA_2}{dt} = -\frac{1}{m} A_2^2 + \frac{i\hbar}{2m} A_4 - U_2. \tag{2.33}$$

The first term on the right-side of equation (2.32) is the complex-valued and non-local quantum force, $-\partial Q_C/\partial z$. This quantum force is not the same function that appears on the right-side of the Bohmian equation, equation (2.12). For example, the Bohmian quantum force is anti-Hook's law (linear in displacement from the center and expansive) for a Gaussian wave packet, but the force term given by $-\partial Q_C/\partial z$ vanishes (Classical trajectories provide the exact propagation for the packet in the latter formulation). The form of the quantum force in equation (2.32) may be the prime reason that low-order DPM calculations give excellent results for some barrier transmission problems (as described later in this study).

Lagrangian equations of any order can be generated using the following equation

$$\frac{dA_n}{dt} = -\frac{1}{2m}\left[\left(A_1^2\right)_n - i\hbar A_{2+n}\right] + \frac{1}{m}A_1A_{1+n} - U_n. \tag{2.34}$$

It was precisely CVDPM(n) that Tannor and co-workers employed in their complex-valued trajectory study. A discussion of the correspondence between RVDPM(n) and CVDPM(n) is provided in Appendix A.

A brief examination of equations (2.28) and (2.32) is in order. The right-hand side of equation (2.32) represents the components of force acting upon each trajectory. The local (or classical) force is contained in the derivative of the potential, while all quantum forces are represented by the $\hbar$-dependent A_3 term. Focusing upon 2nd order DPM leads to trajectories with purely Newtonian (albeit complex) motion, as the A_3-dependent quantum force will be zero. The trajectory is guided through completely local information contained in the derivative of the complex extended 'classical' potential. Note, however, that equation (2.28) includes a non-local quantum energy term A_2. The CVDPM(2) equation for A_2,

$$\frac{dA_2}{dt} = -\frac{1}{m}A_2^2 - U_2, \tag{2.35}$$

includes both local information (from the derivative of the complex potential) and non-local information (through the derivative of A—this information is considered to be non-local as it depends on the state of the entire wave function). This serves to introduce non-locality into equation (2.28) and consequently into equation (2.29), which accumulates the appropriate quantum phase for wave function synthesis at each time step. In effect, CVDPM(2) trajectories are classical trajectories traveling in the complex plane—

quantum information is only manifested thorough the quantum potential appearing in the action function.

Equation (2.33) shows that the trajectory will no longer exhibit classical motion for CVDPM(3), as an approximation to the quantum force influences the trajectory motion. This has an interesting effect on the interpretation of tunneling in the complex plane. CVDPM(2) trajectories are classical in the sense that only local information provided by the potential is used to propagate the trajectory. These trajectories are ones that make it over the top of the barrier—they do not "go through the barrier". However, each CVDPM(2) trajectory is carrying a density which ultimately will make it to the real axis at the arrival time and be 'detected'. The net effect of this density transport on the complex-classical trajectory is to make it appear as if the low-energy initial wave packet 'tunnels' through the classically forbidden region and appears on the transmission side of the barrier.

Interestingly, the CVDPM(2) equations appeared in the literature before the recent publication by Tannor, et al[59]. In generalizing earlier work with Gaussian Wave Packet Dynamics, Huber and Heller[58] extended the classical trajectories into the complex plane, and in effect generated the equations of motion for CVDPM(2) trajectories. Subsequent collaboration with Littlejohn[83] provided deeper mathematical insight into these trajectories. Again, as in the case of RVDPM(n), our formulation has the advantage in that we approximate *A(z,t)* in a quadratic or higher-order expansion along each propagating trajectory, as opposed to a global 'thawed' Gaussian. De Aguiar and co-workers[84] expanded upon this work by Heller by deriving additional approximations to replace the complex trajectories with real trajectories. These studies are semi-classical; it is important to remember that the infinite hierarchy of DPM equations of motion are *exactly* quantum.

III. Model Problem

A. Model Potentials and Initial Wave Packet

In this Section, the initial wave packet and the two potentials are described. The implementation of both RVDPM(n) and CVDPM(n) trajectories will also be discussed. Finally, for comparison with the trajectory results, a space-fixed grid method for solving the TDSE for these scattering problems will be mentioned. All calculations were run to the arrival time $t_a = 1.5$. Unless otherwise stated, all quantities are in atomic units.

The initial conditions on individual trajectories were determined from a Gaussian wave packet of the form

$$\Psi(x) = \left(\frac{2\beta}{\pi}\right)^{\frac{1}{4}} \exp\left(-\beta\left(x - x_o\right)^2 + \frac{ip_o}{\hbar}\left(x - x_o\right)\right). \tag{2.36}$$

This function is normalized on the real axis. Following Tannor, et. al.[59, 26], we choose the width parameter $\beta = 30\pi$, the center of the wave packet x_o = -0.7, and the initial momentum either p_o = 0 (DT case) or 48.9 (HE case). Initial conditions for complex trajectories were obtained by analytically continuing equation (2.36) into the complex plane.

Obtaining the initial functional values required for the time integration of the RVDPM(n) trajectories is straightforward. Equating the right-hand sides of equations (2.1) and (2.36) and separating into real and imaginary parts leads to functions which give the initial values of *C(x,t)* and *S(x,t)* in terms of the parameters in equation (2.36), for any given selected initial x value.

Obtaining initial functional values for CVDPM(n) is a more difficult task. Equating the right-hand sides of equations (2.25) and (2.36) leads to a single equation which returns the initial value of *A(z,t)* with regard to the parameters in equation (2.36) and the initial coordinate z. For CVDPM(n), one obtains the initial coordinates z by merely discretizing the complex-extension of the initial wave packet. However, both the real and imaginary parts of z are needed to obtain the initial condition. Trajectories with the same initial real part but different imaginary parts in their complex positions will have drastically different behaviors. The trajectories of interest will be those which have position $y = 0$ at the specified arrival time and $x > 0$ for the transmitted subset. The imaginary component of the complex initial position has direct effect on both the time and position where these trajectories cross the real axis. The set of initial complex positions z which satisfy the above condition will comprise a curve in the complex plane called an *isochrone*. Any trajectory launched from an initial position on that isochrone will land somewhere on the real axis ($x > 0, y = 0$) at the specified arrival time. Properties of isochrones will be discussed further in Section VI B.

The potentials used for both the real and complex trajectory calculations are either an Eckart barrier of the form

$$V(z) = \frac{V_o}{\cosh^2(\alpha z)}, \tag{2.37}$$

where the barrier height is $V_o = 40$, and the barrier width parameter is $\alpha = 4.32$, or a slightly slimmer Gaussian barrier of the form

$$V(z) = V_o \exp\left(-\gamma z^2\right), \tag{2.38}$$

where again $V_o = 40$, and the width parameter is $\gamma = 15.35$. Both barriers are centered at $z = 0$. The two potentials evaluated on the real axis are shown in Figure 2, while the real and imaginary parts of the complex-extended Eckart potentials are shown in Figures 3 and 4 and the real and imaginary parts of the complex-extended Gaussian potential in Figures 5 and 6, respectively.

Figure 2 shows that we are dealing with a “thick” barrier scattering problem, in that the half-width of the initial Gaussian wave packet is slim compared to the width of the scattering Eckart and Gaussian potentials. Thick barrier quantum scattering problems typically display transmitted probability densities which are similar to those produced by the propagation of the corresponding Wigner wave packet in phase space with the classical Liouville equation. Alternatively, one can obtain classical transmitted probability densities in phase space by integrating the initial Wigner wave packet for $p \geq p_b$, where p_b represents the barrier momentum. An example of the similarity of phase-space classical and quantum barrier transmission probabilities is presented by Rowland and Wyatt[25]. Thin barrier scattering problems will have solutions which depend much more strongly upon the quantum potential and are not reproduced nearly as well with classical phase space methods.

Given the Cauchy-Riemann condition[85] for the complex-valued function *f(x+iy)*, i $\partial f / \partial x = \partial f / \partial y$, we can determine whether or not the potentials given in equations (2.37) and (2.38) are analytic. The Cauchy-Riemann condition is seen to hold for the Gaussian potential in equation (2.38) in the domain of the finite complex plane. Hence, this complex-extended potential would be termed *holomorphic*[85]; that is, the potential has no singularities and is

Figure 2: Real-Valued Potentials

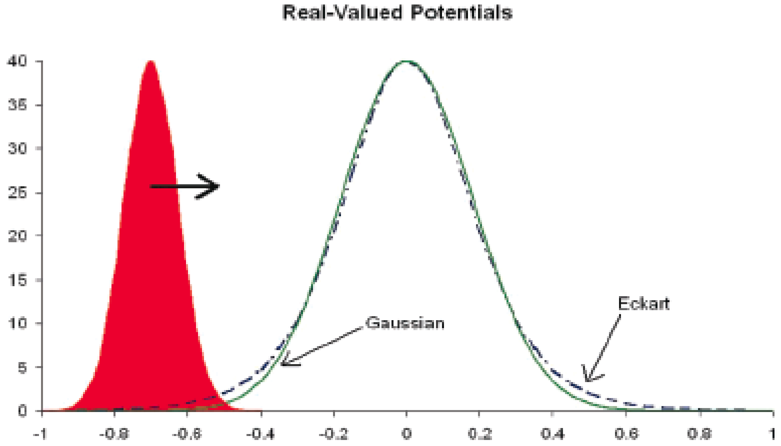

Real-valued Eckart (in blue) and Gaussian (in green) potentials used in this study. The magnitude of the initial Gaussian wave function (solid red) is also shown to compare the relative width of the wave packet to the barrier width. For the purposes of this figure, the peak value for $|\Psi(x)|$ was adjusted to be the same as the barrier height.

Figure 3: Real Part of the Complex-Eckart Potential

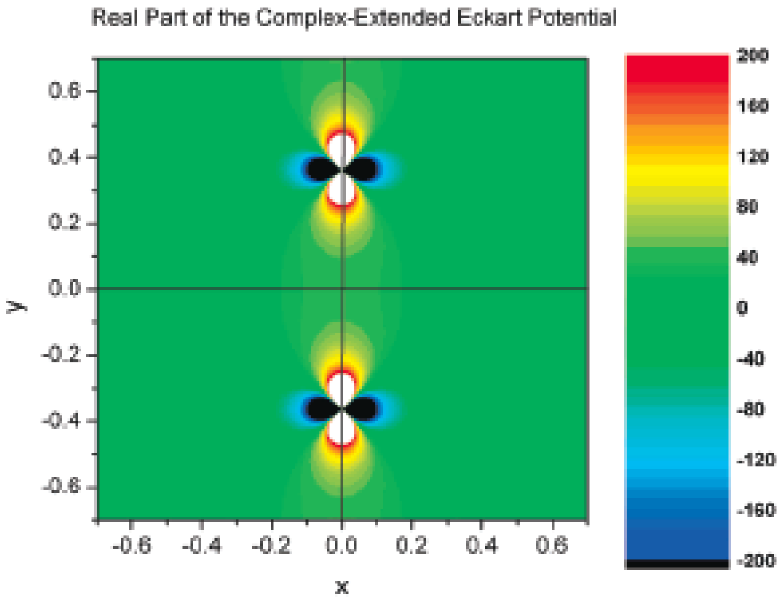

Real part of the complex-extended Eckart potential.

Figure 4: Imaginary Part of the Complex-Eckart Potential

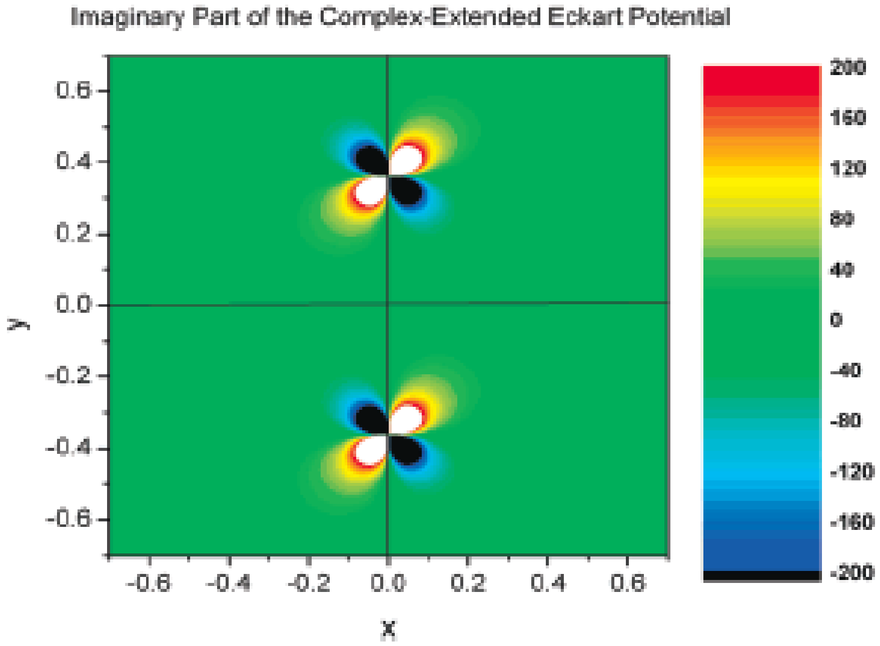

Imaginary part of the complex-extended Eckart potential.

Figure 5: Real Part of the Complex Gaussian Potential

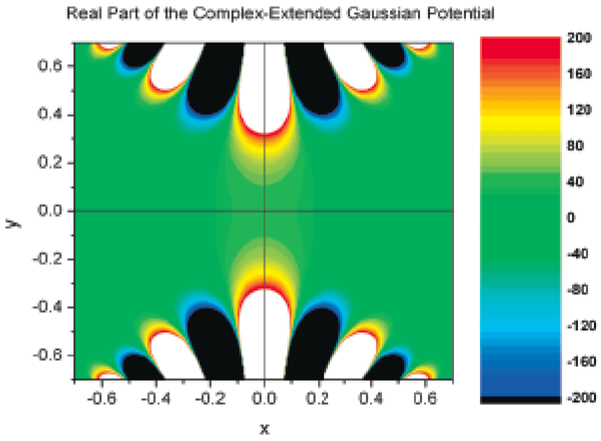

Real part of the complex-extended Gaussian Potential.

Figure 6: Imaginary Part of the Complex-Gaussian Potential

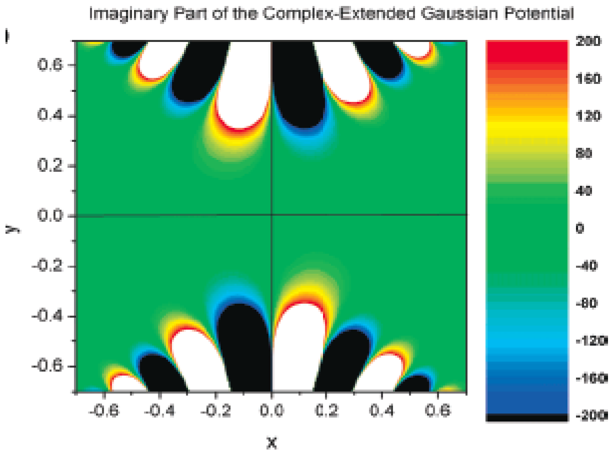

Imaginary part of the complex-extended Gaussian Potential.

differentiable at every point in the finite complex plane. Application of the Cauchy-Riemann condition to equation (2.37) shows that the complex-extended Eckart potential is *meromorphic*[85], that is, it is analytic in the finite complex plane *at all but some isolated points*. These isolated points (albeit countably many) are the poles of the complex-extended Eckart potential. These poles, at the centers of the cloverleaves along the imaginary axis in Figures 3 and 4, are located at

$$z = \frac{m\pi}{2\alpha} i, \tag{2.39}$$

where $m = \pm 1, \pm 2, \ldots$ The two poles of principal interest are located at $z = \pm$ 0.3636i. Later, it will be seen that complex trajectories are forced to avoid the poles in the complex-extended Eckart potential. Very interesting behavior is also obtained for complex trajectories evolving on the complex-extended Gaussian potential.

An examination into the nature of the poles in the complex-extended Eckart potential is in order. Specifically, we would like to examine the behavior of the potential in the vicinity of the pole as well as explain the four-lobed structures and associated signs that appear in Figures 3 and 4. One way to approach this problem is to expand the complex-extended Eckart potential about a pole using a Laurent series[86]. A Laurent series can be thought of as an extension of the Taylor series to complex functions which are meromorphic. Unlike the Taylor series, which only employ positive powers in the power series expansion, a Laurent series may employ negative powers in the expansion,

$$f(z) = \sum_{n=-\infty}^{\infty} a_n (z - z_o)^n, \tag{2.40}$$

where the expansion coefficients a_n are given by Cauchy's integral formula. Performing a Laurent expansion on equation (2.37) about the node located at $z_o = -i\pi/2\alpha$ gives

$$V(z_o) = -\frac{V_o}{\alpha^2}\frac{1}{(z-z_o)^2} + \frac{1}{3}V_o - \frac{1}{15}V_o\alpha^2(z-z_o)^2 + \frac{2}{189}V_o\alpha^4(z-z_o)^4 + O\left((z-z_o)^6\right), \tag{2.41}$$

where the first term in equation (2.41) is known as the *principle part* of the function. Notice that a holomorphic function will have no principle part.

Determining the order of the pole is a simple matter with equation (2.41); all one must do is look to the principle part of the Laurent expansion. In this example, we see that the poles of the complex-extended Eckart barrier are of second order (this means that the residue about the poles will be zero); these poles are neither simple poles (poles of order one, also known as removable singularities) nor are they essential singularities (which would have an infinite number of terms in its principle part). The principle part of the Laurent series describes the behavior of the function in the vicinity of the pole. As one approaches z_o only the principle part of the expansion contributes, up to an additive constant. Simply put, $(z - z_o) = Re^{i\theta}$ (the expression of a complex number in polar form). Combining the above expression with principle part of equation (2.41) gives

$$V(z_o) \to -\frac{V_o}{\alpha^2}\frac{1}{R^2}\exp\left(-2i\theta\right). \tag{2.42}$$

Plotting the real and imaginary parts of this function will reproduce the four-lobed 'quadrapole' structures as well as the signs on those lobes in agreement with Figures 3 and 4.

A similar analysis for poles can be carried out for the Gaussian potential. Making the substitution $z = 1/t$ in equation (2.38) and performing a Taylor series expansion yields

$$V\left(\frac{1}{t}\right) \rightarrow 1 - \frac{\gamma}{t^2} + \frac{\gamma^2}{2t^4} + O\left(\frac{1}{t^6}\right). \tag{2.43}$$

Bearing in mind that as $z \rightarrow \pm\infty$ $t \rightarrow 0$ so that the function is not defined at $\pm\infty$. These will be singularities in the Gaussian potential. The expansion in equation (2.43) tells us that these singularities will be *isolated essential singularities*[85] as the principle part of its expansion has an infinite number of terms.

Holomorphic and meromorphic (excluding poles) functions have very interesting properties which cast a different flavor on CVDPM(n) trajectories. If a function *f(z)* is holomorphic both inside and on a simple closed contour *C* in the complex plane, then the generalized Cauchy integral formula guarantees the existence of the derivatives (including partials) of *f(z)* of all orders[86]. These derivatives will be continuous both on and inside the contour *C*. No similar statement can be made for real functions.

The Cauchy integral formula also states that the value of *f(z)* at any point *z inside* the closed contour *C* will be determined by the values of the function along *C*. This is very interesting in the context of complex DPM trajectories. Complex DPM trajectories can "sense" the behavior of their neighbors through a *regional non-locality*. The potentials and the evolving wave packet remain holomorphic as long as they stay in the finite complex plane (both Eckart and Gaussian potentials) and avoid poles (Eckart potential only). This means that the value of the wave packet at any point *z* in the complex plane is determined solely by the values of the wave packet on a closed contour.

In other words, the value of the function *f(z)* depends on information located at other points (i.e. non-locality). This may explain why low orders of CVDPM(n) can yield very accurate barrier transmission probabilities.

B. Computational/Numerical Methods

Equations of motion for both RVDPM(n) and CVDPM(n) trajectories were implemented by integrating the system of differential equations in time with the second-order implicit trapezoidal method[87]. This method is both symmetric and self-adjoint, which ensures time reversibility. DPM equations for barrier-scattering problems can become stiff in regions where the derivatives of the action may become large (i.e. near a pole). Stating that a system of differential equations is stiff generally means that the dynamical processes being modeled are evolving under multiple timescales[88]. Another way to think of stiffness is that the largest allowable step-size taken is determined by the system's stability rather than the accuracy. The implicit trapezoidal method was chosen to integrate this system of differential equations because it is a relatively easy method to implement and is known to handle stiff systems of differential equations well. Solving this system of non-linear equations requires the use of functional iteration or Newton's method. In this study, functional iteration was used with the initial guess given by the first-order explicit Euler method. Three functional iterations were sufficient at each time step. In both RVDPM(n) and CVDPM(n), the integration time step was $\Delta t = 1 \times 10^{-4}$ a.u.

In order to solve the TDSE on a grid[88,10, 9], the Method of Lines[87] was employed with 4th order centered finite differencing to obtain a system of differential equations which was integrated using the second-order leap-frog method[87]. The leap-frog method is not symplectic, however. This was not a problem in this study, as the normalization on the entire grid remained accurate to 10^{-5} for the length of the calculation. The implicit trapezoidal method was chosen for its good stability properties, and ease of implementation. As in the case of DPM, functional iteration was used to solve the resulting system of non-linear equations; five iterations per time step was found to be sufficient for these calculations. The grid calculation used to solve the TDSE was performed with $\Delta t = 1 \times 10^{-4}$ and $\Delta x = 5 \times 10^{-3}$.

IV. Results

A. Transmission Probabilities

In this Section, transmission probabilities will be presented for RVDPM(n) and CVDPM(n) trajectories for both the Eckart and Gaussian barrier scattering problems. This will be followed by results and discussion for classical complex trajectories (CVDPM(2)). Determining how initial conditions are implemented into CVDPM(n) is discussed later in Subsection B. Finally, some interesting properties of complex quantum trajectories will be explored.

Table 1 lists transmission probabilities for real-valued DPM trajectories for the DT Eckart and HE Gaussian scattering problems. There are some points of note here. First, it appears that the appropriate order of real-valued DPM can give transmitted densities that are close to the exact grid solution. In the case of the HE Gaussian scattering problem, orders 2, 3, and 4 give results that are in good agreement with the exact grid results, whether the final probability is computed by actually interpolating the transmitted wave packet density and integrating or by locating the bifurcation point and integrating the *initial* probability density. However, it is interesting to see that the probabilities for real-valued DPM do not appear to converge smoothly as the order is increased. Similar trends are noted for the HE Eckart scattering problem. Figure 7 shows HE Eckart transmitted probability densities for orders 2 and 3 for real-valued DPM. RVDPM(2) and RVDPM(3) reproduce the exact grid solution. As the order of the DPM is increased to orders 4 and 5, the integrated probabilities agree reasonably well with the numerical probabilities provided by the fixed grid solution.

Table 1. Transmission Probabilities for DPM Barrier Scattering Problems

	order of DPM	**probability**
DT Eckart Real Valued	5	2.79E-007
	6	3.77E-007
	7	3.11E-007
	8	3.34E-007
	9	3.19E-007
	Fixed Grid (exact)	2.90E-007
HE Gaussian Real Valued	2	0.504740
	3	0.503410
	4	0.500900
	5	0.487960
	6	0.419330
	Fixed Grid (exact)	0.502366
DT Eckart Complex Valued	2	2.77E-007
	3	2.90E-007
	4	2.90E-007
	Fixed Grid (exact)	2.90E-007
HE Gaussian Complex Valued	2	0.503070
	3	0.507320
	4	0.501710
	Fixed Grid (exact)	0.502366

Figure 7: RVDPM(n) Probabilities for High Energy Eckart Barrier Scattering

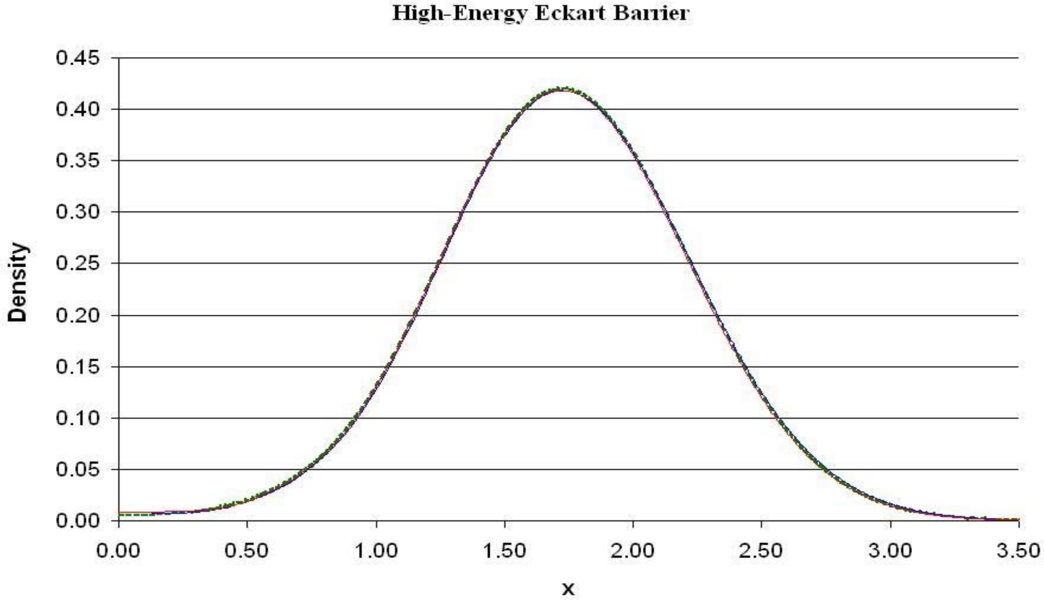

RVDPM(n) transmitted probability densities at $t_a = 1.5$ for HE Eckart barrier densities for n = 2 (blue), 3 (red) and grid (dark green) solutions.

Figure 8: RVDPM(n) Probabilities for Deep Tunneling Gaussian Barrier Scattering

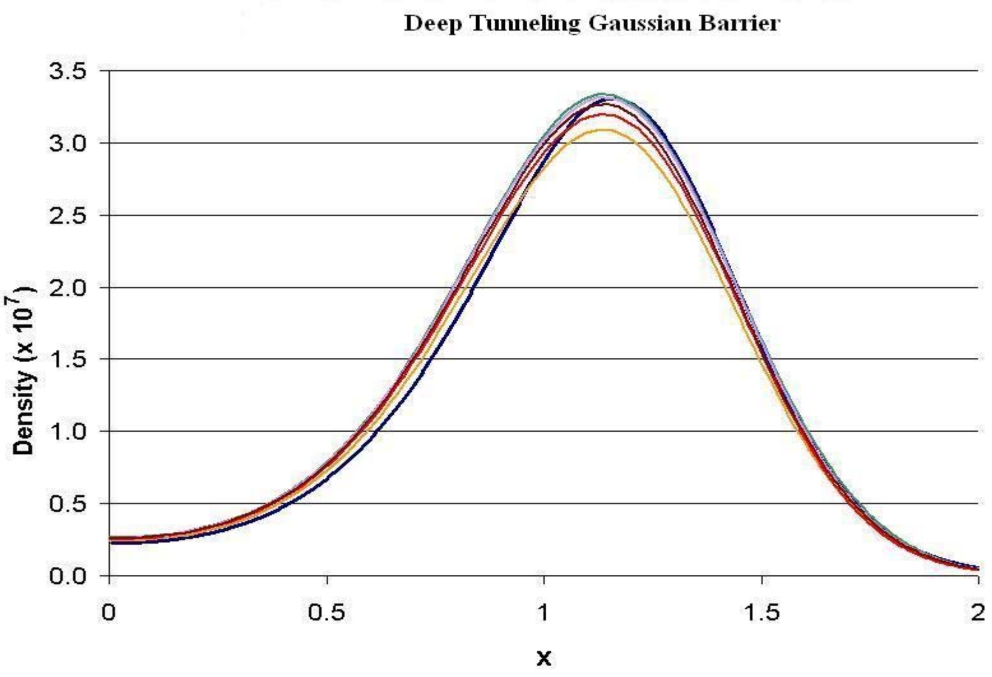

RVDPM(n) transmitted probability densities at $t_a = 1.5$ for DT Gaussian densities for n = 8 (orange), 9 (green), 10 (red), 11 (purple), 12 (brown), and grid (dark blue).

The DT Gaussian scattering problem shows different characteristics. First, accurate solutions require higher-orders of DPM than the corresponding HE case. Figure 8 shows DT Gaussian transmitted probability densities for orders 8 through 12 of RVDPM. There appears to be an oscillation about an average value, with even orders of RVDPM slightly over-estimating the probability and odd orders being just about right.

Figures 9 and 10 show corresponding CVDPM(n) transmitted probability densities for orders 2, 3, and 4 for the same scattering problems as presented in Figures 7 and 8. Initial positions for these trajectories are specifically chosen so that they transmit the barrier ($x > 0$) and are detectable ($y = 0$) at the arrival time $t_a = 1.5$. Figure 9 shows the transmitted densities for the HE Eckart barrier scattering problem for orders 2 through 4. This figure shows that orders 2, 3, and 4 perfectly capture the grid solution, with no detectable decay in the quality of solution. Figure 10 shows the transmitted densities for the DT Gaussian barrier scattering problem for orders 2 through 4. Note that orders 3 and 4 capture the solution exactly. Although CVDPM(2) doesn't quite capture the exact solution, we need to recall that CVDPM(2) trajectories are in fact complex-valued *classical* trajectories transporting an approximate quantum action function (through the inclusion of the non-local term in equation (2.28)). In essence, these trajectories *appear to tunnel* through the barrier, when in reality they are following classically proscribed paths through the complex plane while transporting approximate quantum density. Increasing CVDPM to order 3 adds an approximation to the quantum force to the classical force when computing the trajectory. Note that the CVDPM(n) solutions remain in agreement with the grid solution through order 4. Similar accuracies and trends are noted in the DT

Figure 9: CVDPM(n) Probabilities for High Energy Eckart Barrier Scattering

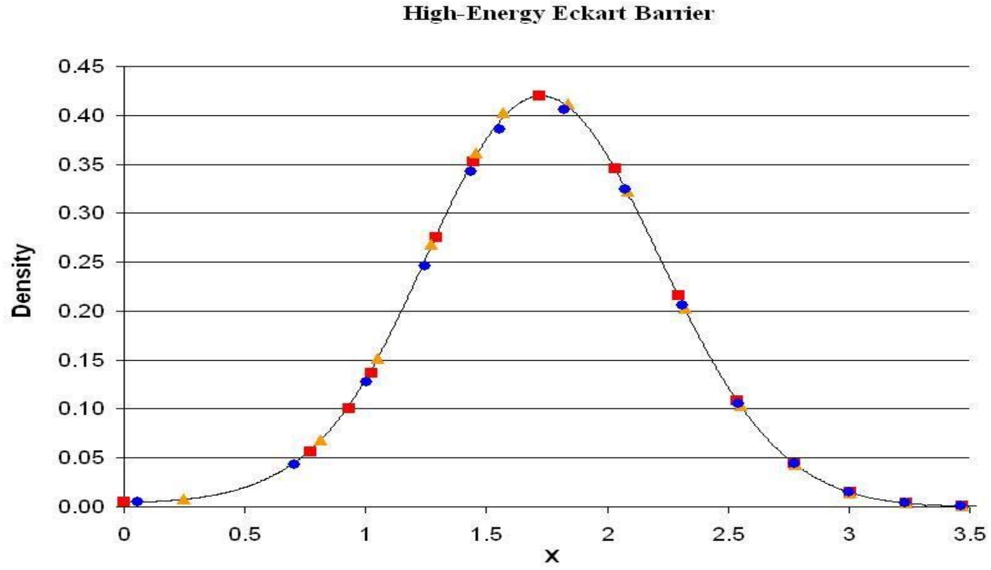

CVDPM(n) transmitted probability densities at $t_a = 1.5$ for n = 2 (red squares), 3 (orange triangles), 4 (blue circles), with grid (black line) for HE Eckart barrier solutions.

Figure 10: CVDPM(n) Probabilities for Deep Tunneling Gaussian Barrier Scattering

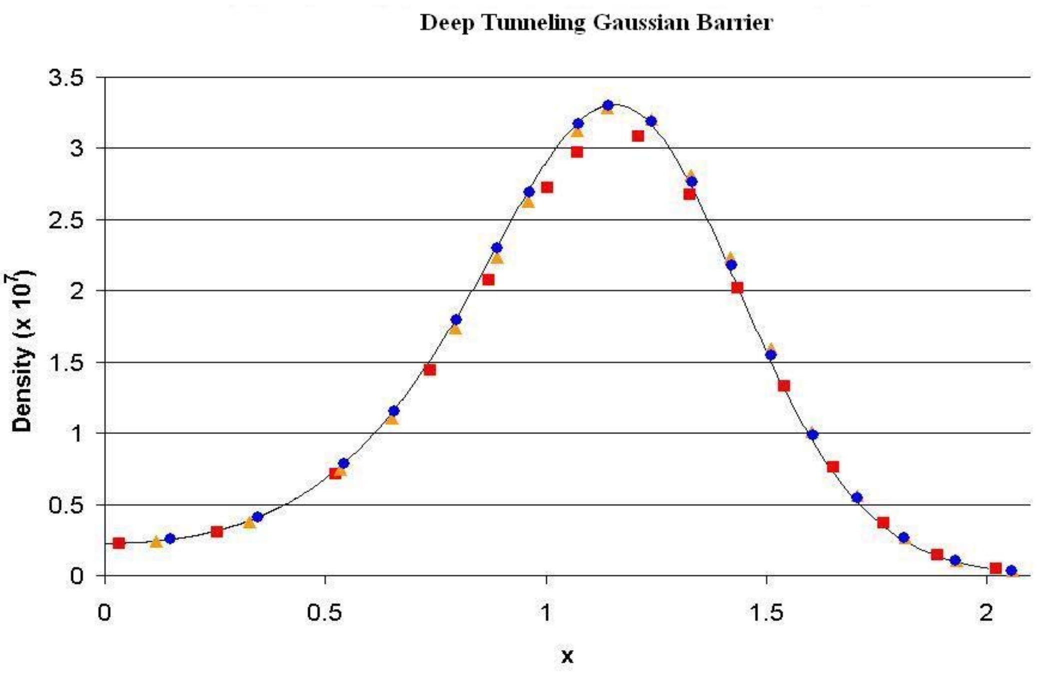

CVDPM(n) transmitted probability densities at $t_a = 1.5$ for n = 2 (red squares), 3 (orange triangles), 4 (blue circles), with grid (black line) for DT Gaussian solutions.

Eckart problem and in the HE Gaussian problem. CVDPM(n) was run through order 6 for these four problems with no decay in the solution quality.

B. Isochrones

Figure 11 shows nine CVDPM(2) trajectories (blue curves) for the arrival time $t_a = 1.5$. Also shown are contour lines for the absolute value of the complex-extended Eckart potential. These trajectories are launched from a curve in the complex plane—the isochrone. Some of the characteristics of isochrones will now be considered. Figure 12 shows the isochrones for the DT Eckart scattering problem for CVDPM(n) orders 2, 3, and 4. Notice that the isochrones traverse only a small portion of the complex plane. The order 2 isochrone converges on the *x*-coordinate of the center of the initial wave packet ($x_c = -0.7$) but does not extend to values of x which are less than this. This point represents the initial coordinate of the last detectable, transmitted complex trajectory. Increasing the order to CVDPM(3) changes the isochrone in two ways. First, each point is shifted down in the imaginary direction. Since these trajectories will be traveling farther than corresponding CVDPM(2) trajectories, and they still need to reach the real axis at $t_a = 1.5$, they need to traverse this distance faster. To understand this further, one must understand how the real and imaginary components of the complex-extended potential are manifesting themselves upon the trajectory, which will be examined later in Section IV C. Secondly, unlike CVDPM(2) trajectories, it is seen that higher-order isochrones extend to the left of the center of the initial wave packet. These trajectories have different properties than those launched with $x > -0.7$. These trajectories will be analyzed further in Section IV D of this chapter. Figure 13 shows similar behavior to that found in Figure 12.

Figure 11: Rutherford-like Scattering around an Eckart Pole

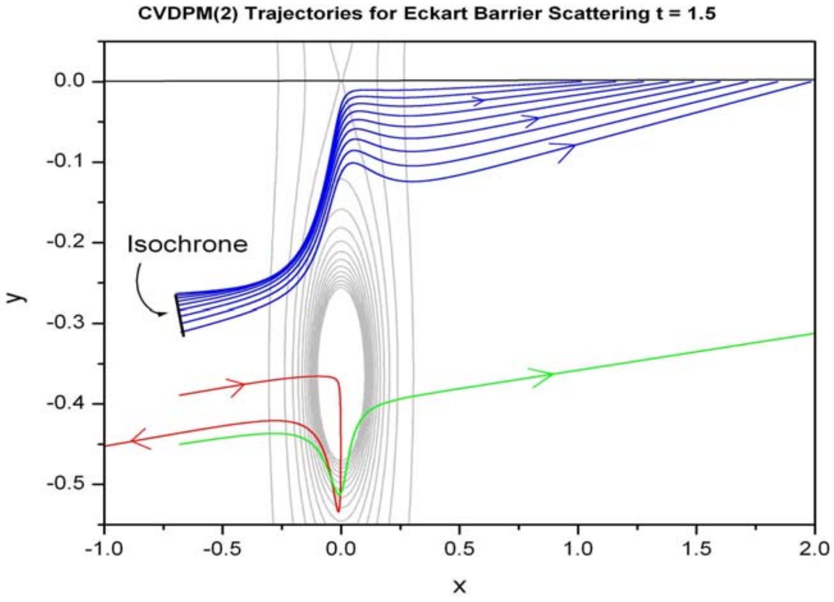

Classical complex trajectories for the deep tunneling Eckart barrier scattering problem, with contours of the absolute value of the complex-extended Eckart potential. Note how the detected transmitted trajectories with the arrival time $t_a = 1.5$ (shown in blue) bend away from the pole on the imaginary axis (at z = -0.35i) in a manner reminiscent of Rutherford foil scattering. The green trajectory is also transmitted, but it is not detected until a time $t > 1.5$. The red trajectory is backscattered from the potential and is undetected at $t_a = 1.5$.

Figure 12: Isochrone for Deep Tunneling Gaussian Barrier Scattering

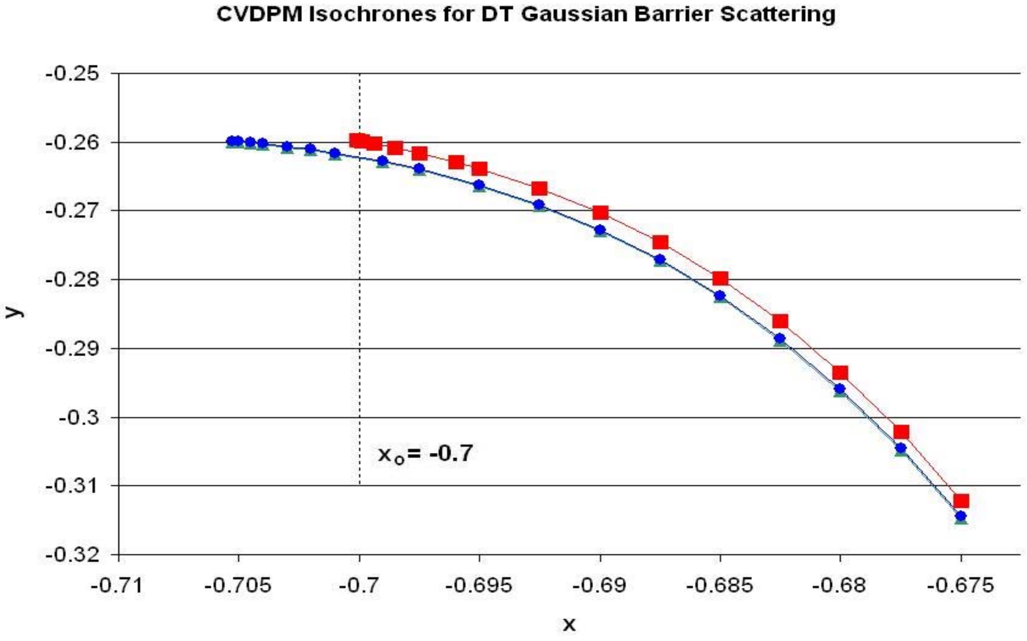

CVDPM(n) isochrones for the arrival time $t_a = 1.5$: n = 2 (red squares), 3 (dark green triangles), and 4 (blue circles) for DT Eckart scattering problem.

Figure 13: Isochrone for High Energy Eckart Barrier Scattering

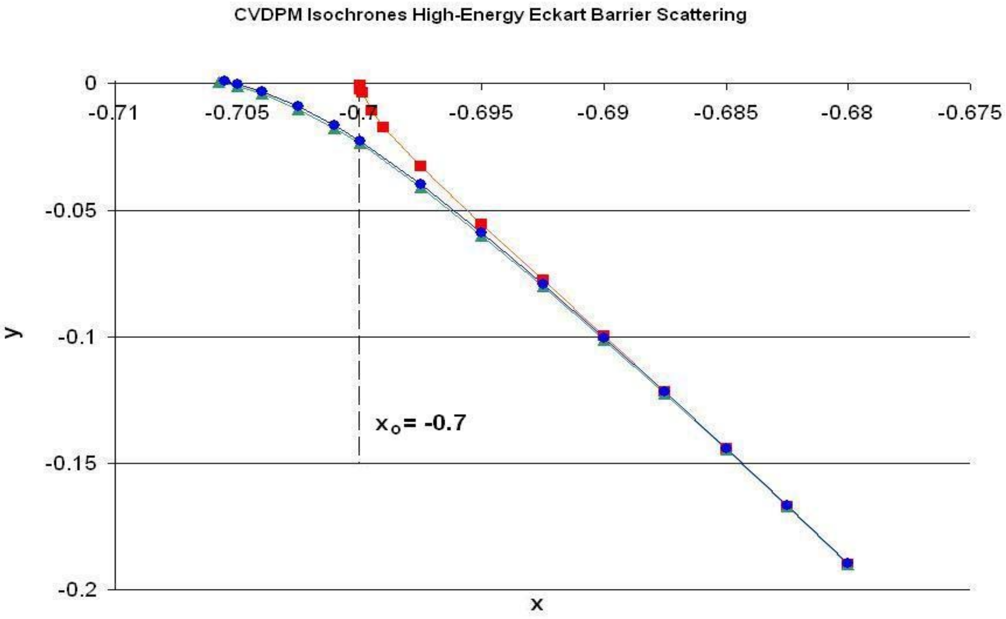

CVDPM(n) isochrones for the arrival time $t_a = 1.5$: n = 2 (red squares), 3 (dark green triangles), and 4 (blue circles) for HE Eckart scattering problem.

12, but for HE scattering from the Eckart barrier. It is interesting to note that all three isochrones converge on the real axis, but at different locations. CVDPM(2) trajectories exhibit the same convergence at the center of the wave packet as seen for the DT Eckart scattering problem in Figure 12. CVDPM(3) and CVDPM(4) lead to very nearly the same isochrone. Isochrones for initial energies between DT and HE barrier scattering will lie between these extremes. Isochrones for both the DT and HE Gaussian barrier problems show similar placements and trends as the Eckart cases. It is interesting to note that the isochrones appear to converge for orders 3 or 4 for all cases.

Obtaining the locations of the isochrones proves to be the most difficult part of implementing CVDPM(n). Initial coordinates were obtained by taking a slice for a constant value for y and selecting x to be between 0 and x_o. This will yield initial values for $A(z,t)$ and its spatial derivatives, which allows one to integrate the trajectory equations. The final location of this trajectory in the complex plane was noted at the preset arrival time t_a, and the initial x-coordinate was varied in order to allow the trajectory to cross the real axis at the arrival time. This is similar to finding the bifurcation point in the real-valued DPM problem, however, this calculation must be repeated many times at different values of y in order to define the isochrone. It is also possible to fit a high-order polynomial to a few data points (once they have been obtained) to help predict the location of the isochrone[75]. In this way, the search procedure could be automated, but that was not done in this study.

C. Classical Complex Trajectories

In this section, some properties of CVDPM(2) trajectories will be explored. Figure 11 reveals that different initial coordinates may lead to drastically different effects during the evolution of the complex-trajectories. The potential energy contours shows that these trajectories are interacting with the pole centered around z = -0.35i. The reactive trajectories (in blue) with $t_a = 1.5$ can be seen deflecting around the top of this pole, while one transmitted trajectory (green curve) with $t_a > 1.5$ skirts around the lower edge of this pole. A non-transmitted trajectory (red curve) is also shown. Note how this trajectory appears to enter the barrier region but is repelled by the pole; this trajectory has initial conditions which lead it directly toward this pole.

The behavior of these trajectories suggests that a force analysis of CVDPM(2) trajectories will be instructive. Figure 14 shows two CVDPM(2) trajectories, one transmitted, one back-scattered for the DT Eckart problem. The arrows represent the vectors of force, $-dV/dz$, for the complex-extended Eckart potential. These trajectories follow classical paths, and it is interesting to see how they are influenced by the complex-valued force. Notice that the trajectories follow the lines of force.

In order to make further progress, we will examine the initial Lagrangian velocities of the trajectories. This velocity as a function of the complex position is given by

$$v_{initial}(z) = -\frac{i\hbar}{m}\left(-2\beta(z-x_o)+\frac{ip_o}{\hbar}\right) = \left(\frac{p_o}{m}-\frac{2\hbar\beta}{m}y\right)+i\frac{2\hbar\beta}{m}(x-x_o). \qquad (2.44)$$

For the DT case, $p_o = 0$. It is seen that the real-part of the initial velocity when $y = 0$ is just as expected, p_o/m. Of interest are both the real and imaginary parts of the initial velocity. This equation reveals that trajectories launched from below the real axis ($y < 0$)

Figure 14: Initial Force Analysis for Eckart Barrier Scattering

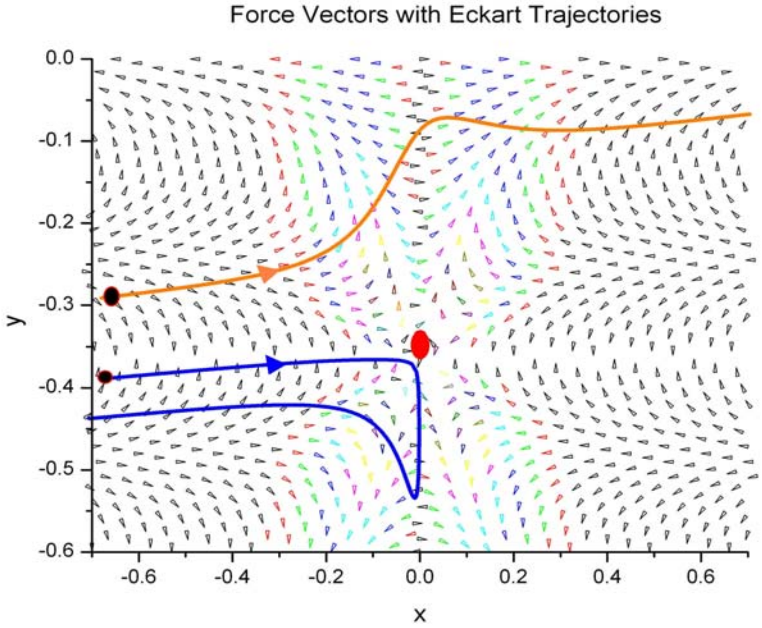

Classical complex trajectories for the Eckart deep tunneling case for transmitted (orange) and reflected (blue) trajectories with force arrows from the complex-extended Eckart potential surface. The center of the pole in this potential is denoted by the red dot. The trajectories follow classical paths through the complex coordinate space.

Figure 15: Initial Velocity Field for Deep Tunneling Wave Packet

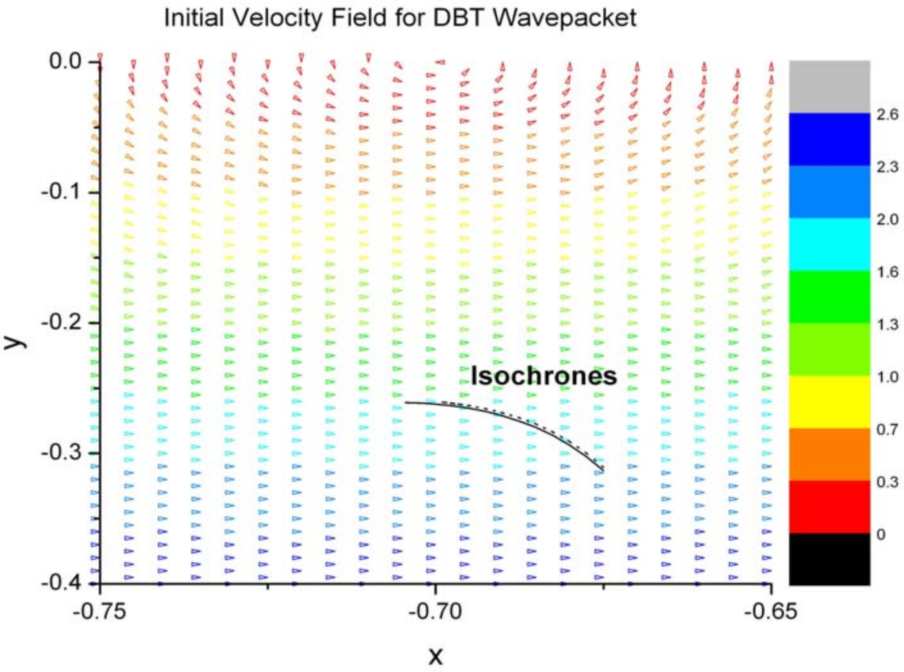

Initial velocity fields, colored by magnitude, with CVDPM(2) (dashed) and CVDPM(3) (solid) isochrones for the deep tunneling problem.

Figure 16: Initial Velocity Field for High Energy Wave Packet

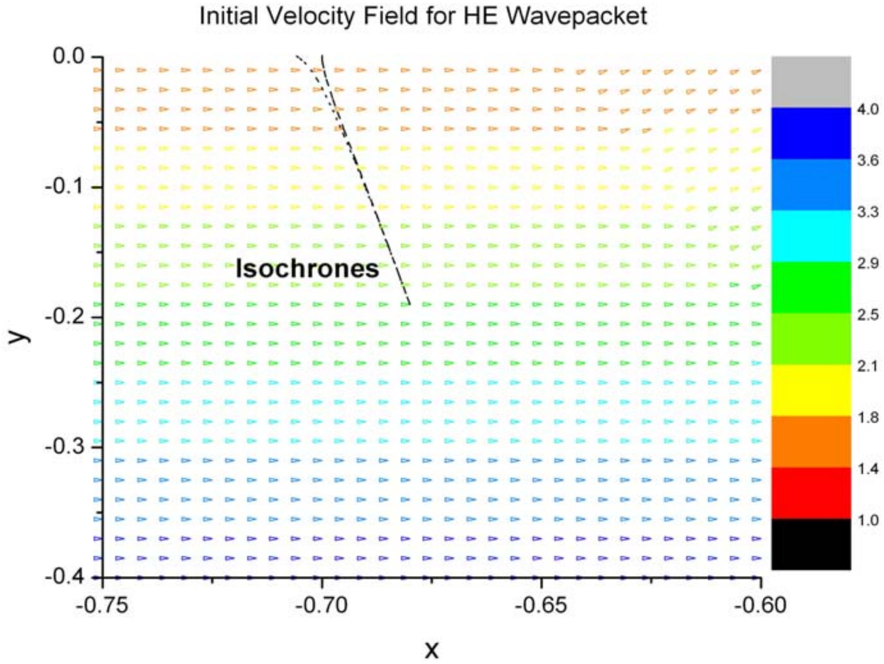

Initial velocity fields, colored by magnitude, with CVDPM(2) (dashed) and CVDPM(3) (solid) isochrones for high energy scattering problem.

will have a positive x component. For trajectories initiating to the right of the center of the wave packet ($x > x_o$), the initial velocity will contain a component in the positive y direction. Figure 15 shows a plot of equation (2.44) for the DT Gaussian scattering problem while Figure 16 shows a plot for the HE Eckart scattering problem. These figures also show CVDPM(2) and CVDPM(3) isochrones for these scattering problems. It is seen that in the regions of interest (near the isochrones), the resultant initial velocity vector is directed toward positive x. Overlaying Figures 14 and 15 can help one define where isochrones might be located, as one can get an idea of the initial impetus each trajectory will have and what forces will influence its subsequent evolution. In addition, as seen in equation 44, trajectories located to the left of the center of the initial wave packet (for CVDPM(3) and CVDPM(4) trajectories) will have $v_{initial}$ which contains a component in the *negative y* direction.

It is interesting to trace the transmitted trajectory's path through this force field knowing that the initial impetus is in the positive x direction. The transmitted trajectory shows a large slowdown in the x direction as the trajectory begins to decelerate in the barrier region. While the trajectory is decelerating in the x direction, it very quickly accelerates in the y direction. This trajectory is able to circumvent the pole located near $z = -0.35i$ by slipping around the top. The reflected trajectory, however is not able to do the same. It encounters very large forces repelling it away from the barrier region, and subsequently this trajectory reaches a turning point in the x direction and reverses course. In essence, the pole plays a role similar to that of the nucleus in the Rutherford foil experiment—some trajectories are able to skirt above or below the pole (which, of course, will affect the trajectory's arrival time), while some trajectories will aim right for the pole and will subsequently be back-scattered into the reflected region.

Figure 17 shows the transmitted trajectory from Figure 14 by plotting both the real and imaginary parts of the kinetic energy versus the propagation time on the *z*-axis. Note that as the trajectory enters the barrier region ($t \sim 0.25$) there is a decrease in the real kinetic energy and a corresponding increase in the imaginary kinetic energy (features which can also be seen in Figure 14). The real kinetic energy can even be seen to go negative for 0.75 a.u.. To help understand this, we will decompose the complex-valued kinetic energy into real and imaginary parts

$$KE = \frac{\left(p_x + ip_y\right)^2}{2m} = \frac{p_x^2 - p_y^2}{2m} + i\frac{p_x p_y}{m}. \tag{2.45}$$

The real component of the kinetic energy can take on negative values if $|p_x| < |p_y|$. However, from Figure 17, when the real component of the kinetic energy is negative, the imaginary component of the kinetic energy is positive, indicating that p_x and p_y are either both positive or negative values. Figure 14 reveals that the trajectory is moving in the positive y direction at this time, thus showing that even when the real kinetic energy is negative, the trajectory is still making progress in the direction of the positive real axis.

D. Quantum Complex Trajectories

Figure 18 shows trajectories for the HE Gaussian scattering problem, as well as a contour map for the complex-extended Gaussian potential. The solid red lines indicate order 3 trajectories originating to the *left* of the wave packet center which cross the real axis *twice*. CVDPM(3) trajectories originating on the right of the wave packet center

Figure 17: Kinetic Energy Profile for Transmitted Trajectory

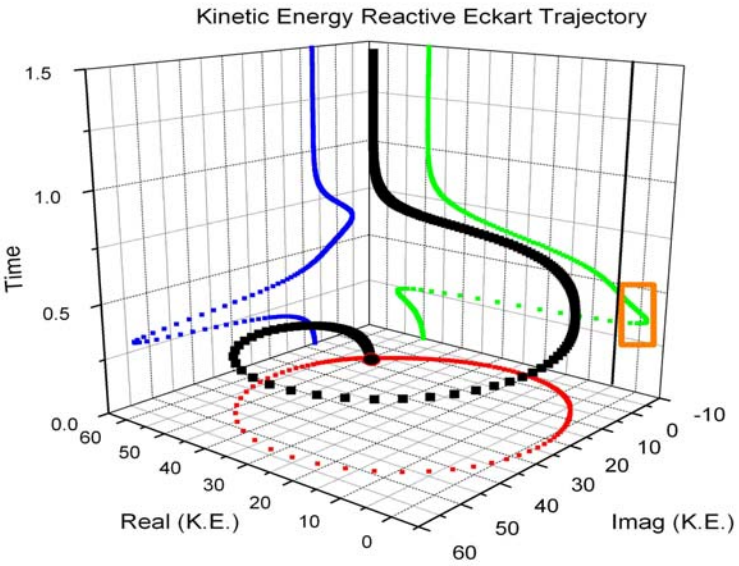

Kinetic energy profile for the transmitted trajectory in Figure 14. An orange box denotes the region where the real component of the kinetic energy is negative.

Figure 18: Trajectories Which Exhibit Multiple Crossings of the Real Axis

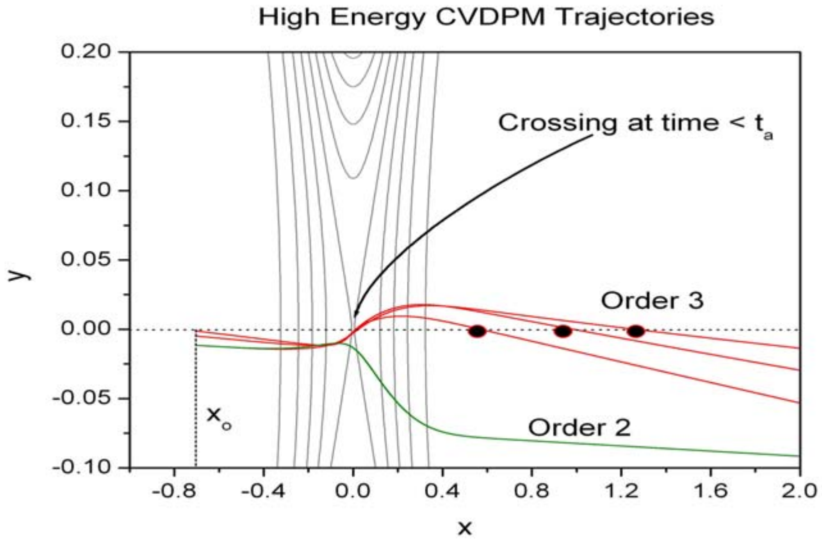

CVDPM(n) trajectories for the HE Gaussian scattering problem, with contours of the absolute value of the complex-extended Gaussian potential. The red lines represent CVDPM(3) trajectories which exhibit two crossings with the real axis and originate on the left side of the center of the wavepacket. The green line is a CVDPM(2) trajectory launched from the same initial position as one of the order 3 trajectories.

only exhibit one crossing of the real axis. CVDPM(3) trajectories originating to the left of the wave packet center will cross the real axis once at a time (around $t = 0.7$) prior to the specified arrival time $t_a = 1.5$, then cross the real axis once more at the specified arrival time. These trajectories are repelled by a very strong potential energy wall once they cross the real axis at $t = 0.7$. This imparts a force in the negative y direction which induces the second crossing. At both of these crossing points, the trajectory exhibits a probability density that matches the exact value of the density at that time *and* at that point in space as determined by the grid calculation. Carrying the integration to later times reveals that these trajectories will not cross the real axis again, at a time greater than $t_a = 1.5$, as there will be no force component to impart an upwards motion to the trajectory (it has already moved beyond the barrier region). This figure also shows an order 2 trajectory which is launched from an identical position as one of the transmitted order 3 trajectories. Note that it does not approach close to the real axis on the timescales of interest.

Figure 19 shows the real and imaginary parts of the wave function plotted against U_I (the imaginary part of the potential) and the probability density for the CVDPM(2) trajectory plotted in Figure 18. Figure 20 shows the same, only plotted this time for the CVDPM(3) trajectory launched with the same initial conditions as the CVDPM(2). Figure 18 showed that both the CVDPM(3) and CVDPM(2) trajectories will transmit the barrier ($x > 0$), but the CVDPM(2) trajectory will not be detected because there is not time at which $y = 0$. In Appendix A it is shown that the real and imaginary parts of $A(z,t)$ in the CVDPM(n) equations can be expressed in a form that is

Figure 19: Imaginary Potential for CVDPM(2) Trajectory

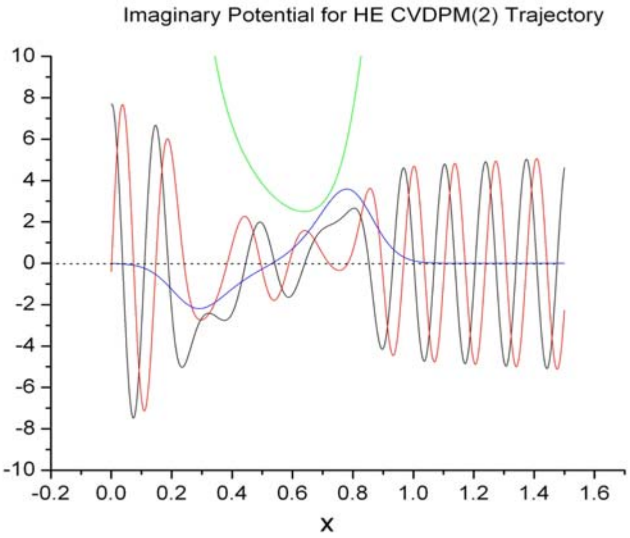

Imaginary potential U_I (blue) with real (black) and imaginary (red) parts of the wave function and density (green) for CVDPM(2) trajectory for the HE Guassian barrier scattering problem. The sign of U_I determines the behavior of the density. A positive U_I leads to a growing density while a negative U_I forces the density to decay.

Figure 20: Imaginary Potential for CVDPM(3) Trajectory

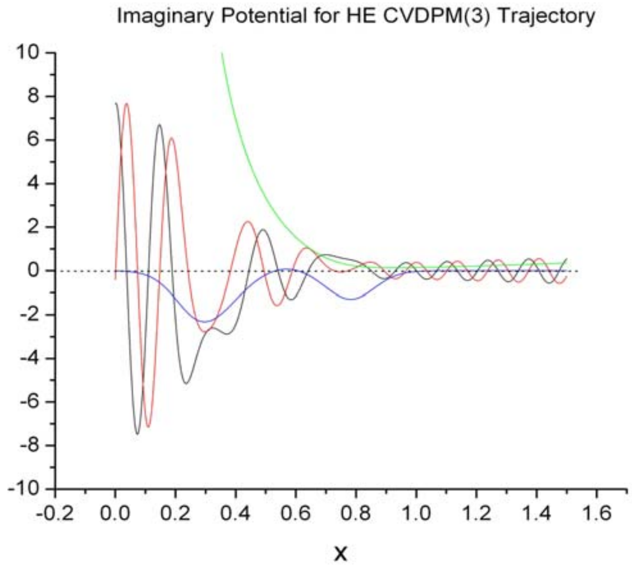

Imaginary potential U_I (blue) with real (black) and imaginary (red) parts of the wave function and density (green) for CVDPM(3) trajectory. Note how the initial value of the wave function gradually decreases to the expected value at the arrival time t_a.

similar to the of RVDPM(n) equations, albeit complex-valued. The density can be computed at any point through the relation $\rho(z,t)$ = exp(-2/$\hbar$ Im($A(z,t)$)). The time derivative of the imaginary component $A(z,t)$ (given in Appendix A as $G(z,t)$), containing density information, is given by

$$\frac{dG(z,t)}{dt} = \frac{\hbar}{2m} F_2 - U_I, \tag{2.46}$$

while the time derivative of the real component of $A(z,t)$, the phase of the wave function, is given by

$$\frac{dF(z,t)}{dt} = \frac{1}{2m} F_1^2 - U_R - \frac{\hbar}{2m} G_2 + \frac{1}{2m} G_1^2. \tag{2.47}$$

Substituting equation 46 into the expression for $\rho(z,t)$ yields

$$\rho(z,t) = \exp\left(-\frac{1}{m} \int_0^t F_2 dt + \frac{2}{\hbar} \int_0^t U_I dt \right). \tag{2.48}$$

Figure 19 illustrates how the real and imaginary parts of the wave function as well as $\rho(z,t)$ vary with position verses the variation in U_I. It is important to note the behavior of U_I in Figures 19 and 20. The two trajectories start with the same initial position, and for early times U_I is similar for both trajectories. A difference develops, however, in Figure 19, around $x = \sim 0.5$ a.u. It is noted that U_I changes sign and becomes a positive valued function which decays to zero when $x > 1$ (away from the barrier region). It is around this point that $\rho(z,t)$ stops declining and starts to increase. The density computed along this trajectory remains large and does not decay to the correct value by $t_a = 1.5$. In Figure 20, however, $\rho(z,t)$ is seen to decay to the value found on the real axis at t = 1.5. The behavior of $\rho(z,t)$ with respect to that of U_I can be examined with equation (2.48). If U_I is positive, it is serving to *increase* the value of $\rho(z,t)$, while the opposite is true for a negative value for U_I, as seen in Figure 20. The path of the trajectory through the complex plane must be chosen such that the integral of U_I cancels just enough of the integral of F_2 (in equation (2.46)) such that the correct density is transported by the trajectory when it crosses the real axis at the arrival time. It is shown in Appendix A that equation (2.46) reduces to equation (2.9) on the real axis. The complex-extended potential is seen to have a dual role for CVDPM(n) trajectories. As in RVDPM(n), the real component of the potential still determines the motion of the trajectory in the x direction. Likewise, the imaginary component of the potential will determine the motion of the trajectory in the y direction.

V. Conclusions

A. Summary of Results

Given the appropriate order, RVDPM(n) was shown to be a quick method for obtaining a very good approximation to transmission probabilities in barrier scattering problems, including the deep tunneling case. Because there are no functional fittings and very few trajectories are required to evaluate the bifurcation point, RVDPM(n) yields vast computational savings over other quantum trajectory methods. RVDPM(n) trajectories are parallelizable, and RVDPM(n) trajectory results have been presented for three-dimensional problems[35]. There are several known problems with RVDPM(n), however. High-orders of RVDPM(n) are required in regions where the wave function develops nodes or in regions of interference. Additionally, the results may not be very good. In problems where the barrier is thin compared to the width of the initial wave packet, the transmitted wave function may not be very accurate. Presently, there is no way of predicting the best order of RVDPM(n) to use for a particular barrier scattering problem, though in general it seems that results for higher-energy problems are very good with low-orders of DPM while deep tunneling problems require higher-orders to produce good transmission probabilities.

CVDPM(n) trajectories very accurately reproduce transmission probabilities at low-orders in both the deep barrier tunneling and higher energy barrier scattering problems *for thick barriers*. For both the Eckart and Gaussian potentials it was found that CVDPM(3) was sufficient to almost exactly predict the transmission probability for deep barrier tunneling problems while CVDPM(2) was sufficient for high energy scattering problems. CVDPM(n) demonstrates good convergence properties on the potential energy surfaces (Eckart and Gaussian) under study. However, it is not to be expected that this will be true for every potential energy surface of interest—more study is needed in this area. Because CVDPM(n) is just the Derivative Propagation Method applied to the complex-extended quantum Hamilton-Jacobi equations, CVDPM(n) trajectories will also share the same parallelizability as their RVDPM(n) counterparts. Again, very few CVDPM(n) trajectories are needed to accurately compute the transmission probability, and in the next chapter an extension of this method to two-dimensional[75] (one translational and one vibration) barrier transmission problems will be presented.

In all, the greatest difficulty with CVDPM(n) lies in locating the isochrones from which one obtains the initial spatial coordinates needed to launch the trajectories. In two dimensions, this situation becomes worse, as the isochrone will become a surface in four-dimensional space[75] and consequently this makes location of the initial coordinates much more difficult. Higher-dimensional problems will introduce even more difficulty in the isochrone search problem. Also, computation of the transmission probability at intermediate time steps requires searching for the location of new isochrones. Depending upon the situation, one may lose much of the computational advantage in CVDPM(n) through the isochrone location problem. Another possible problem with CVDPM(n) concerns potentials which do not have a global analytical function by which to perform the analytic continuation (*ab initio* potentials, for example). This directly impacts situations which will be of interest to the quantum dynamicist. However, there are methods for *numerically* constructing the analytic continuation of a function given only discrete data on the real axis, and these will be discussed in the final chapter. In spite of these issues, CVDPM(n) still proves to be a very interesting method for computing transmission probabilities.

Chapter 3: Extension of Complex Quantum Trajectories to Two-Dimensional Problems

I. Introduction and Outline

A. Motivation

In the previous chapter[26], the RVDPM and CVDPM were both applied to one-dimensional scattering problems employing either Eckart or Gaussian barriers. These barriers were 'thick' compared with the width of the initial Gaussian wave packet. Deep tunneling and higher energy barrier transmission probabilities were compared with exact results obtained using a large space fixed grid. For the DPM implementation involving complex trajectories, special emphasis was placed upon locating *isochrones*. All trajectories with their initial coordinates falling on an isochrone are 'detected' at the same time on the transmitted side of the barrier. From the action function carried by these trajectories, the transmitted density at the specified arrival time may be readily computed.

The current study extends our previous analysis[26] of one-dimensional scattering to a system involving two degrees of freedom, specifically, an Eckart or Gaussian barrier along the 'reaction coordinate', which is coupled to a harmonic mode with a variable force constant. The DPM is used to evolve independent complex quantum trajectories. This study primarily involves the propagation of 2nd order trajectories, namely, classical trajectories along which is transported an action function which includes an approximate quantum potential. Special emphasis is placed upon the distribution of arrival times for transmitted trajectories and locating isochronal surfaces in the complex coordinate space. A relatively simple model is used for locating the initial coordinates for trajectories which fall on an isochronal surface corresponding to a specific arrival time. In addition, the diffraction of quantum trajectories around poles in the complex extended Eckart potential surface is described. Finally, the probability densities for the transmitted wave packets are presented, and problems are pointed out for scattering on ‘thin’ Eckart barriers, where the poles in the complex valued potential lie close to the real axis.

B. Outline of Chapter

This paper is organized as follows. In subsection II, the complex valued potential surfaces involving both Eckart and Gaussian barriers are described and then the initial wave packet in complex coordinate space is presented. Subsection III first reviews the quantum Hamilton Jacobi equation and its solution, the complex action function. The exact equations of motion for complex Lagrangian quantum trajectories are also derived. This section concludes with a derivation and discussion of the DPM equations of motion. Subsection IV presents a number of computational results obtained using complex quantum trajectories: the distribution of arrival times for trajectories to land on the transmitted side of the barrier, the definition and properties of isochrones, including a model for the isochronal surface, and the diffraction of trajectories around poles in the complex Eckart potential. In addition, plots of the transmitted probability density are presented, and, finally, the behavior of higher order quantum trajectories is described. Subsection V then summarizes some of the results and presents suggestions for further study.

II. Theory

A. Lagrangian Equations of Motion in Two Dimensions

If the exponential (polar) form for the wave function, given by $\psi(x_1, x_2, t) = \exp(iS(x_1, x_2, t)/\hbar)$, is substituted into the time-dependent Schrödinger equation, the quantum Hamilton-Jacobi equation (QHJE) for the action function $S(x_1, x_2, t)$ in real-valued coordinate space is obtained:

$$-\frac{\partial S}{\partial t} = \frac{1}{2m}\left[\left(\frac{\partial S}{\partial x_1}\right)^2 + \left(\frac{\partial S}{\partial x_2}\right)^2\right] + V(x_1, x_2) + \frac{\hbar}{2mi}\left[\frac{\partial^2 S}{\partial x_1^2} + \frac{\partial^2 S}{\partial x_2^2}\right]. \tag{3.1}$$

The final term on the right side of this equation, the quantum potential, brings in all quantum effects through the curvature of the action function ($\nabla^2 S$). This quantum potential, denoted by $Q(x_1, x_2, t)$, is not the same function as the Bohm quantum potential, Q_B . The relationship between Q_B and Q is described in the Appendix of reference 71. With the momentum components given by the guidance relations, $p_j = \partial S/\partial x_j$, the first term in equation (3.1) is recognized as the kinetic energy, $T = (p_1^2 + p_2^2)/(2m)$. In addition, the quantum potential depends upon the divergence of the momentum field,

$$Q = \hbar/(2mi)(\partial p_1/\partial x_1 + \partial p_2/\partial x_2) = \hbar/(2mi)\nabla \cdot \vec{p}$$

Continuation of the QHJE into complex space is accomplished by making the substitutions $x_1 \to z_1$ and $x_2 \to z_2$. The action $S(z_1, z_2, t)$ is then regarded as a complex valued function of the complex coordinates and the momentum components, defined by

$p_j = \partial S / \partial z_j$, are also complex valued. If the complex phase is written in terms of real and imaginary parts, $S = S_R + iS_I$, the real part S_R determines the phase of the wave function and the imaginary part determines the modulus, $|\psi| = \exp(-S_I/\hbar)$.

Because the time derivative in equation (3.1) is computed at a fixed point in space, this version of the QHJE is expressed in the Eulerian frame. The time derivative in a moving frame will now be introduced. Although there many possible moving frames, the Lagrangian frame is chosen for this study. In this case, the 'observer' moves with the complex velocity, which has components $v_j = (1/m)\partial S / \partial z_j$, and the 'moving time derivative' is given by

$$\frac{d}{dt} = \frac{\partial}{\partial t} + \left[v_1 \frac{\partial}{\partial z_1} + v_2 \frac{\partial}{\partial z_2} \right], \tag{3.2}$$

where the second term is the convective (flow) contribution. Substituting for $\partial S / \partial t$ in equation (3.1) then gives the Lagrangian version of the QHJE

$$\frac{dS}{dt} = \frac{1}{2m}\left[\left(\frac{\partial S}{\partial z_1} \right)^2 + \left(\frac{\partial S}{\partial z_2} \right)^2 \right] - V(z_1, z_2) - \frac{\hbar}{2mi}\left[\frac{\partial^2 S}{\partial z_1^2} + \frac{\partial^2 S}{\partial z_2^2} \right]. \tag{3.3}$$

The right side of this equation, the excess of the kinetic energy over the total potential energy, $V + Q$, is the quantum Lagrangian.

In order to solve the QHJE using quantum trajectories, the following exact equations of motion can be derived for the coordinates and momenta (see, for example, references 62-69)

$$\frac{dz_1}{dt} = \frac{p_1}{m}, \qquad \frac{dz_2}{dt} = \frac{p_2}{m},$$
$$\frac{dp_1}{dt} = -\frac{\partial}{\partial z_1}[V + Q], \qquad \frac{dp_2}{dt} = -\frac{\partial}{\partial z_2}[V + Q]. \tag{3.4}$$

In addition, along each trajectory, equation (3.3) is integrated to find the action function and from this function the wave function may be synthesized. In equations (3.3) and (3.4), spatial derivatives of S are involved and their numerical evaluation along the trajectory presents a challenge for solving these equations. In order to circumvent the derivative evaluation problem, we now turn to the derivative propagation method, which is based upon propagating a small number of equations to obtain approximations for these spatial derivatives.

B. Derivative Propagation Method

The derivative propagation method (DPM) was developed as an approximate technique for solving the real valued (Bohmian) quantum trajectory equations of motion[18-25]. A significant advantage of this approach is that instead of propagating an ensemble, approximate quantum trajectories may be run independently, one at a time. For quantum trajectories associated with real-valued hydrodynamic equations, the DPM has been shown to accurately predict probabilities for barrier transmission. However, the DPM generally fails to account for interference effects, node formation, and features arising from long-range correlations between quantum trajectories. Problems associated with the DPM have been discussed elsewhere[19].

In order to develop the DPM for complex valued trajectories[59], we return to the Eulerian version of the QHJE given in equation (3.1). Using subscript notation to denote the order of the spatial partial derivatives with respect to z_1 and z_2, this equation may be written

$$-\frac{\partial S_{0,0}}{\partial t}=\frac{1}{2m}\left[S_{1,0}^2+S_{0,1}^2\right]+\frac{\hbar}{2mi}\left[S_{2,0}+S_{0,2}\right]+V_{0,0}. \tag{3.5}$$

Taking first and second partial derivatives with respect to z_1 and z_2 then gives the five equations

$$\begin{aligned}
-\frac{\partial S_{1,0}}{\partial t}&=\frac{1}{m}\left[S_{1,0}S_{2,0}+S_{0,1}S_{1,1}\right]+\frac{\hbar}{2mi}\left[S_{1,2}+S_{3,0}\right]+V_{1,0},\\
-\frac{\partial S_{0,1}}{\partial t}&=\frac{1}{m}\left[S_{0,1}S_{0,2}+S_{1,0}S_{1,1}\right]+\frac{\hbar}{2mi}\left[S_{2,1}+S_{0,3}\right]+V_{0,1},\\
-\frac{\partial S_{2,0}}{\partial t}&=\frac{1}{m}\left[S_{1,0}S_{3,0}+S_{0,1}S_{2,1}+S_{2,0}^2+S_{1,1}^2\right]+\frac{\hbar}{2mi}\left[S_{4,0}+S_{2,2}\right]+V_{2,0},\\
-\frac{\partial S_{0,2}}{\partial t}&=\frac{1}{m}\left[S_{0,1}S_{0,3}+S_{1,0}S_{1,2}+S_{0,2}^2+S_{1,1}^2\right]+\frac{\hbar}{2mi}\left[S_{0,4}+S_{2,2}\right]+V_{0,2},\\
-\frac{\partial S_{1,1}}{\partial t}&=\frac{1}{m}\left[S_{1,0}S_{2,1}+S_{0,1}S_{1,2}+S_{1,1}S_{2,0}+S_{0,2}S_{1,1}\right]+\frac{\hbar}{2mi}\left[S_{3,1}+S_{1,3}\right]+V_{1,1}.
\end{aligned} \tag{3.6}$$

In equations (3.5) and (3.6), the quantum potential and the components of the quantum force along z_1 and z_2 are given by

$$Q=\frac{\hbar}{2mi}\left[S_{2,0}+S_{0,2}\right],$$

$$F_{q,1}=-\frac{\hbar}{2mi}\left[S_{3,0}+S_{1,2}\right],\qquad F_{q,2}=-\frac{\hbar}{2mi}\left[S_{0,3}+S_{2,1}\right]. \tag{3.7}$$

In 3quation (3.11), the derivative of total order n on the left side is coupled to both lower and higher-order derivatives on the right side. The coupling to higher derivatives brings in the next two orders, namely, orders $(n+1)$ and $(n+2)$. Taking higher-order spatial derivatives beyond $n=2$ leads to an infinite hierarchy of coupled ordinary differential equations for S and its partial derivatives.

In order to convert these equations into the Lagrangian frame, the time derivative is transformed with the relation (see equation (3.2))

$$-\frac{\partial}{\partial t}=-\frac{d}{dt}+\frac{1}{m}\left[S_{1,0}\frac{\partial}{\partial z_1}+S_{0,1}\frac{\partial}{\partial z_2}\right]. \tag{3.8}$$

Using this equation, the Lagrangian version of equations (3.6) then becomes

$$\begin{aligned}
\frac{dS_{1,0}}{dt}&=-\frac{\hbar}{2mi}\left[S_{3,0}+S_{1,2}\right]-V_{1,0},\\
\frac{dS_{0,1}}{dt}&=-\frac{\hbar}{2mi}\left[S_{0,3}+S_{2,1}\right]-V_{0,1},\\
\frac{dS_{2,0}}{dt}&=-\frac{1}{m}\left[S_{2,0}^2+S_{1,1}^2\right]-\frac{\hbar}{2mi}\left[S_{4,0}+S_{2,2}\right]-V_{2,0},\\
\frac{dS_{0,2}}{dt}&=-\frac{1}{m}\left[S_{0,2}^2+S_{1,1}^2\right]-\frac{\hbar}{2mi}\left[S_{0,4}+S_{2,2}\right]-V_{0,2},\\
\frac{dS_{1,1}}{dt}&=-\frac{1}{m}S_{1,1}\left[S_{2,0}+S_{0,2}\right]-\frac{\hbar}{2mi}\left[S_{3,1}+S_{1,3}\right]-V_{1,1}.
\end{aligned} \tag{3.9}$$

In order to make progress, the system of coupled Lagrangian equations is truncated at total order n, thus obtaining the complex-valued derivative propagation method, denoted CVDPM(n).

From equations (3.9) and (3.6), the five CVDPM(1) equations of motion are given by

$$\begin{aligned}
\frac{dp_1}{dt}&=-V_{1,0}, \qquad \frac{dz_1}{dt}=p_1,\\
\frac{dp_2}{dt}&=-V_{0,1}, \qquad \frac{dz_2}{dt}=p_2.
\end{aligned} \tag{3.10}$$

$$\frac{dS_{0,0}}{dt}=\frac{1}{2m}\left[S_{1,0}^2+S_{0,1}^2\right]-V_{0,0}.$$

These equations do not involve any quantum terms and are thus classical equations of motion in the complex space. The right side of the final equation defines the classical Lagrangian, integration of which gives the classical action function evaluated along the classical trajectory.

The next higher approximation, CVDPM(2), obtained from equations (3.9) by dropping 3-rd and 4-th order derivatives, is given by the system of equations

$$\begin{aligned}
&\frac{dp_1}{dt}=-V_{1,0}, \qquad \frac{dz_1}{dt}=p_1,\\
&\frac{dp_2}{dt}=-V_{0,1}, \qquad \frac{dz_2}{dt}=p_2,\\
&\frac{dS_{2,0}}{dt}=-\frac{1}{m}\left[S_{2,0}^2+S_{1,1}^2\right]-V_{2,0},\\
&\frac{dS_{0,2}}{dt}=-\frac{1}{m}\left[S_{0,2}^2+S_{1,1}^2\right]-V_{0,2},\\
&\frac{dS_{1,1}}{dt}=-\frac{1}{m}\left[S_{1,1}S_{2,0}+S_{0,2}S_{1,1}\right]-V_{1,1}.
\end{aligned} \tag{3.11}$$

In this system, the upper four equations determine a classical trajectory and the lower three are used to determine the second derivatives of the action function. These second derivatives are then used to find quantum potential in equation (3.7) from which the action is obtained by integrating the quantum Lagrangian along the classical trajectory

$$\frac{dS_{0,0}}{dt}=\frac{1}{2m}\left[p_1^2+p_2^2\right]-\left[Q+V\right]. \tag{3.12}$$

In second-order, quantum effects arise solely through the influence of the quantum potential in the action function.

Unlike CVDPM(1) and CVDPM(2), in CVDPM(3) and higher-order CVDPM the quantum trajectory is influenced by the sum of the classical and quantum forces. For one-dimensional barrier scattering, higher orders have been studied[25,59].

The initial conditions on the action function and its derivatives are determined from the complex-valued quadratic action function associated with the Gaussian wave packet in equation (3.18)

$$S(z_1, z_2) = -i\hbar \ln(4\beta_1\beta_2/\pi^2) + i\hbar\beta_1(z_1 - \bar{x}_1)^2 + i\hbar\beta_2 z_2^2 + k(z_1 - \bar{x}_1). \tag{3.13}$$

The first and second order partial derivatives with respect to z_1 and z_2 are readily obtained.

III. Model Problem

A. Model Potentials

Letting x_1 and x_2 denote the real parts of the translational and vibrational coordinates, respectively, the potential energy is the sum of either an Eckart or a Gaussian barrier (of height V_0) centered at $x_1 = 0$ which is coupled to a harmonic oscillator with a variable force constant along x_2. This total potential on the real axis is given by

$$V(x_1, x_2) = V_{trans}(x_1) + \frac{1}{2}k(x_1)x_2^2. \tag{3.14}$$

The translational potential is either an Eckart barrier, $V_0 \sec h^2(\alpha x_1)$, or a Gaussian barrier, $V_0 \exp(-\beta x_1^2)$. In equation (3.14), the variable force constant $k(x_1) = (1 - \sigma \exp(-x_1^2))$ reaches its minimum value, $k_0(1-\sigma)$, at the barrier maximum.

For use in the trajectory studies described later in this study, the values of the parameters are given by (in atomic units): $V_0 = 0.035$, $\beta = 7$, $k_0 = 0.09$, and $\sigma = 0.1$. For the Eckart barrier, two width parameters were used: $\alpha = 3$ for the thin barrier and $\alpha = 1.4$ for the thick barrier. The width parameter for the Gaussian was chosen so that the thin Eckart and the Gaussian barriers have similar half-widths. Using the mass $m = 2000$, the classical vibrational period for the oscillator is $\tau = 2\pi\sqrt{m/k_0} = 937$.

Complex coordinates will now be introduced. With y_1 and y_2 denoting the imaginary parts of the translational and vibrational coordinates, respectively, the complex translational and vibrational coordinates are

$$z_1 = x_1 + i y_1, \quad z_2 = x_2 + i y_2. \tag{3.15}$$

Continuation of the potential in equation (3.14) into the complex plane, for the Eckart barrier for example, is then

$$V(z_1, z_2) = V_0 \operatorname{sech}^2(\alpha z_1) + \frac{1}{2} k_0 (1 - \sigma e^{-z_1^2}) z_2^2. \tag{3.16}$$

Analytic continuation of the Eckart potential into complex coordinate space leads to features that significantly affect the trajectory dynamics. Along the imaginary axis at the barrier position ($z_1 = i y_1$), the Eckart potential becomes

$$V_0 / \cosh^2(\alpha \cdot i y_1) = V_0 / \cos^2(\alpha \cdot y_1). \tag{3.17}$$

This potential thus exhibits an infinite string of isolated singularities, at the positions given by $z_n = i \cdot n\pi/(2\alpha)$, $n = \pm 1, \pm 3, \ldots$ This type of complex valued function is referred to as a *meromorphic* function. As described in more detail in the previous chapter[26], these singularities are actually *double poles*, because the Laurent series expansion of the potential is dominated near the pole by the term $V(z) = -V_0/[\alpha^2(z - z_n)]^2$. Using the value of α for the thin barrier, these poles occur at $z_1 = \pm 0.523i, \pm 1.569\,i, \ldots$ When the barrier becomes thicker, the poles move away from the real axis. For the thick barrier studied here, the first pair of poles occurs at $z_1 = \pm 1.122\,i$.

For the Gaussian potential, $V_0 \exp(-\beta z_1^2)$, along the imaginary axis at the barrier position ($z_1 = i y_1$), this function becomes $V_0 \exp(\beta y_1^2)$ and is singular at the two points $y_1 = \pm\infty$. The behavior near these isolated singularities can be determined by making the substitution $y_1 = 1/\eta$ and examining the behavior as $\eta \to 0$. Because the series expansion of the function $\exp(\beta / t^2)$ has an infinite number of terms, the singularity is an *essential singularity.* Fortunately, quantum trajectories do not closely approach these points.

Two isosurfaces for the real part of the Eckart potential energy surface given in equation (3.16) are shown in Figure 21. These surfaces of constant values of the potential are plotted in the three-dimensional (x_1, y_1, x_2) subspace, with $y_2 = 0$. The vertical tubes parallel to the x_2- y_1 imaginary axis enclose poles in V. Trajectories that make it from the incident (left side region) to the transmitted (or product side) of the barrier (on the right side) must navigate around these poles, through the lower-energy channels evident between the poles. Two isosurfaces of the real part of the Gaussian potential energy surface are shown in Figure 22. There are no poles in this surface, but in common with the Eckart potential surface, there are oscillations in the magnitude and sign of the potential along the x_1 axis.

Figure 21: Isosurfaces for the Real Part of the 2-D Thin Eckart-vibrational Barrier

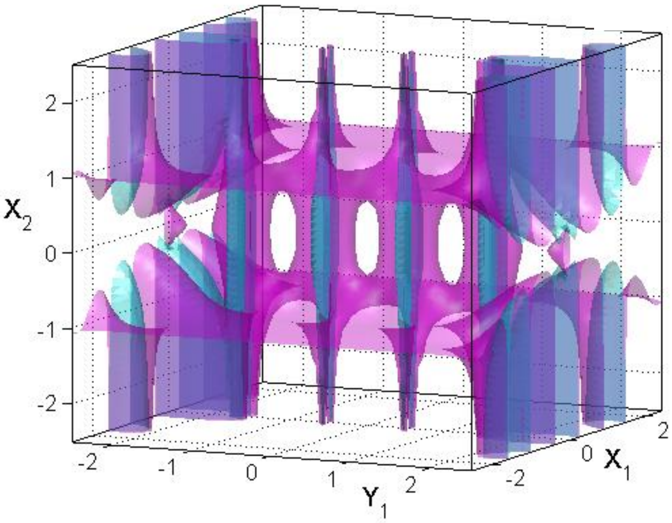

.Isosurfaces (α = 3) for the real part of the thin Eckart potential energy surfaces plotted in the three-dimensional (x_1, y_1, x_2) subspace, with $y_2 = 0$. The isosurface has the value ± 0.045 a.u. The vertical tubes enclose poles in the complex-valued Eckart potential energy surface.

Figure 22: Isosurfaces for the Real Part of the 2-D Thin Gaussian-vibrational Barrier

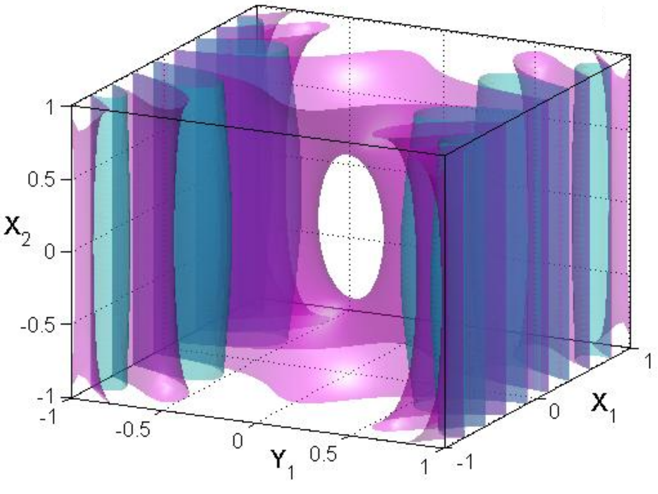

.Isosurfaces for the real part of the thin Gaussian potential energy surface plotted in the three-dimensional (x_1, y_1, x_2) subspace, with $y_2 = 0$. The isosurface has the value ± 0.045 a.u. The Gaussian potential surface exhibits oscillations along the x_1 direction, but there are no poles.

B. Initial Wave Packet in Two Dimensions

The initial wave packet at $t = 0$ is the product of Gaussians for the translational and vibrational modes multiplied by a plane wave driving term which directs the packet toward the barrier region. In the real valued subspace, this normalized wave packet is given by

$$\psi(x_1, x_2) = \left(\frac{2\beta_1}{\pi}\right)^{1/4} e^{-\beta_1(x_1-\bar{x}_1)^2} \cdot \left(\frac{2\beta_2}{\pi}\right)^{1/4} e^{-\beta_2 x_2{}^2} \cdot e^{ik(x_1-\bar{x}_1)}. \qquad (3.18)$$

In this expression, the translational packet is centered at $\bar{x}_1$ and $k = \sqrt{2mE/\hbar^2}$, where E is the mean translational energy. The ground state vibrational packet is centered at $x_2 = 0$ with $\beta_2 = \sqrt{mk_0}/(2\hbar)$. The center of the translational packet is located on the real axis at $\bar{x}_1 = -2.5$ a.u. and the width parameter is $\beta_1 = 6$.

Continuation of this packet into the complex coordinate space is obtained by making the substitutions $x_1 \to z_1$ and $x_2 \to z_2$. In Figure 23, isosurfaces for the absolute value of the wave function are shown in the same three-dimensional subspace used for Figure 21. Each of the Gaussian factors in equation (3.18) can be expressed in the form

$$\exp(-\beta z^2) = \exp(-\beta x^2)\exp(\beta y^2)\exp(2ixy)$$

Because of the factor $\exp(\beta y^2)$, the complex Gaussian becomes singular in the limit $y \to \pm\infty$. Isolated essential singularities of this type were encountered for the Gaussian potential mentioned in the previous section. In addition, the isosurfaces in Figure 23

Figure 23: Isosurfaces for the Complex-Extended Initial Wave Packet in 2-D

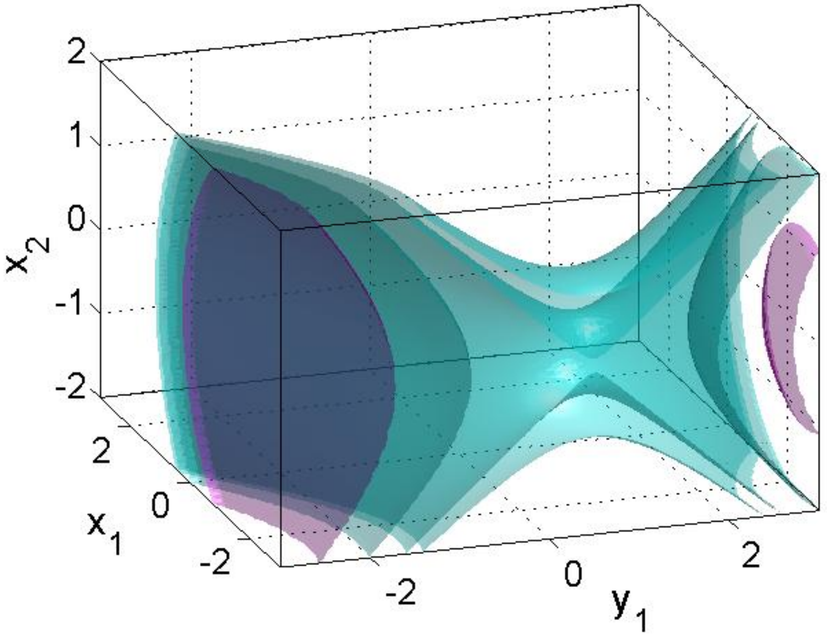

Isosurfaces of the absolute value of the complex-valued wave function plotted in the three-dimensional (x_1, y_1, x_2) subspace, with $y_2 = 0$. The four isosurfaces have the values 10^{-3}, 10^{-1}, 10^{4}, and 10^{12}. The center of the wave packet is given by $\overline{x}_1 = -2.5$, $y_1 = 0$, $x_2 = 0$, $y_2 = 0$.

pinch together along the positive imaginary axis (near the point $z_1 = (k/2\beta_1)i$) due to the factor $\exp(\beta_1 y_1^2 - ky_1)$ in the complex valued wave function.

C. Numerical Methods

With the initial conditions specified, the CVDPM equations of motion are integrated to find the trajectory and the action function. When a trajectory encounters the barrier region, the system of differential equations may become stiff (more detail is presented in ref. 26). This may happen because of the rapid changes in the spatial derivatives which enter these equations. Stiff differential equations generally have solutions with multiple time scales and standard explicit integrators (such as forward Euler or Runge-Kutta) my fail to provide accurate solutions. For this reason, implicit integrators are usually used to solve stiff systems of ordinary differential equations. In this study, a second-order accurate implicit Runge-Kutta algorithm was employed. (Specifically, we used the routine ode23tb from MATLAB, which implements the TR-BDF2 algorithm[89]).

IV. Results

A. Arrive Time Distribution for Transmitted Trajectories

In general, if many trajectories are launched from the reactant region on the ‘left’ side of the barrier ($x_1 < 0$), some will back scatter from the potential and others will make it to the product side ($x_1 > 0$) of the barrier. Within the latter set, some trajectories will never pass through the real plane ($y_1 = 0, y_2 = 0$); these trajectories eventually fly off into complex space. However, trajectories arriving on the product side of the barrier that pass through the real coordinate plane are 'detected' as transmitted trajectories.

For an ensemble of trajectories launched from a grid in the reactant region, there will be a *distribution of arrival times* for the transmitted trajectories. In order to characterize this distribution, a number of trajectories were launched from a Cartesian grid in the four-dimensional (x_1, y_1, x_2, y_2) space in the reactant region on the left side of the barrier. This grid was defined as follows. First, n_{1y} slices were defined along the y_1 axis and along each of these slices, n_{1x} points along x_1 were chosen. The points (x_1^0, y_1^0) thus selected define a grid in the initial translational coordinate space. Next, for each of these points, a square grid of $n_2 \times n_2$ points was defined in the space of initial vibrational coordinates. As a result of this discretization, a four-dimensional rectangular box consisting of $n_{1x} \times n_{1y} \times n_2^2$ points was set up. Of the trajectories launched from these points when the initial translational energy was $E = 0.25\,V_0$, about 4% underwent barrier transmission and crossed the real product coordinate plane at a later time.

The distribution of arrival times (t_A) for transmitted trajectories as a function of the initial translational coordinate (x_1^0, y_1^0) are shown in Figure 24 for $E = 0.25\,V_0$. These trajectories were run on the thin Eckart potential surface. There are no transmitted trajectories for $y_1^0 > -0.5$ and $y_1^0 < -1.2$. The shortest arrival times, $t_A < 500$, occur for trajectories launched from the leading (right) edge of the initial wave packet and the longest times, $t_A > 2000$, occur for points just forward of the center of the initial wave packet. From this figure, it is apparent that the arrival surface in some regions has 'thickness', meaning that there is more than one value for t_A for the same translational point (x_1^0, y_1^0). This feature arises because variations of the initial vibrational coordinates (x_2^0, y_2^0) lead to different trajectories having slightly different arrival times.

Another feature evident from this figure is the very steep increase in arrival times when $y_1^0 \approx -0.5$ and x_1^0 is near the center of the initial wave packet ($x_1^0 \approx -2.5$). This makes accurate location of isochrones computationally demanding if grid search is performed. Isochrones are described in more detail in the following section.

Another significant feature shown in Figure 24 is the gap in the arrival times that extends toward larger values of x_1^0 as y_1^0 becomes more negative. This gap arises because trajectories divert around the sides of the pole nearest to the real axis. Features of the trajectories on the two sides of the gap and the origin of the gap will now be considered. Figure 25 shows the distribution of arrival times for one slice along the imaginary axis, namely $y_1^0 = -0.75$. For the trajectories used to construct this plot, the initial vibrational

Figure 24: Distribution of Arrival Times for the thin Eckart Potential

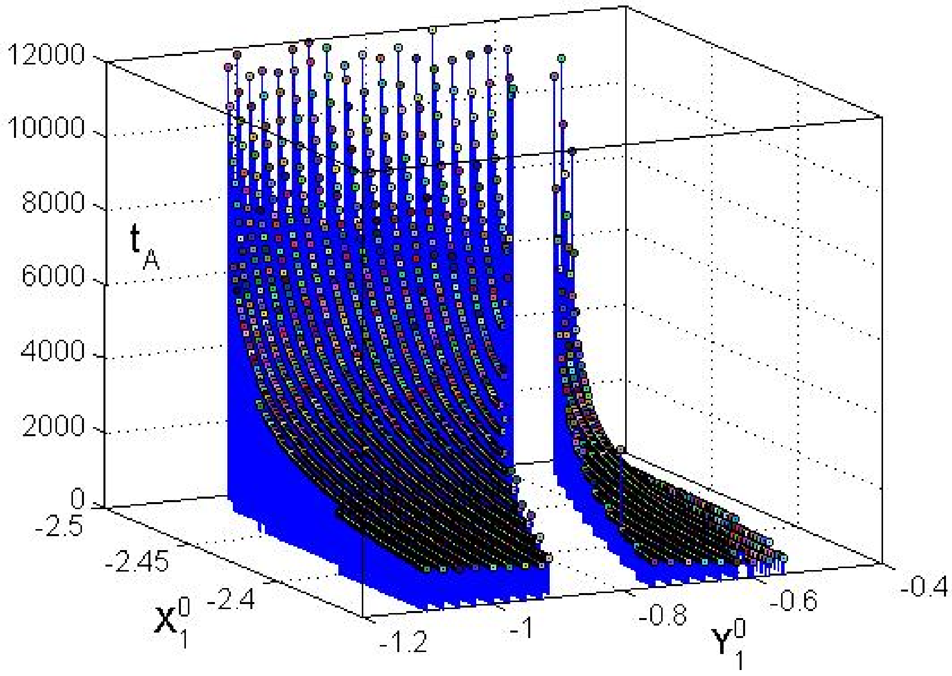

Distribution of arrival times t_A for transmitted trajectories when $E = 0.25\,V_0$. The arrival time is plotted for starting points (x_1^0, y_1^0) in the translational subspace. These arrival times were calculated for trajectories evolving on the thin Eckart potential energy surface.

Figure 25: Arrival times for trajectories

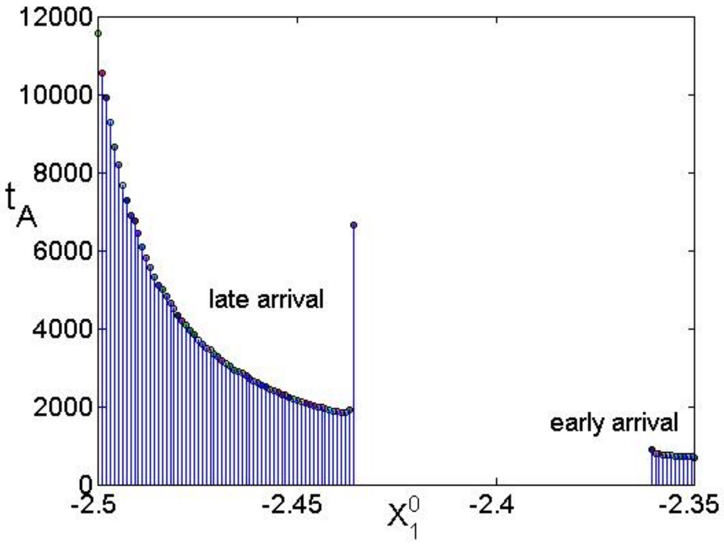

Arrival times for trajectories launched with $y_1^0 = -0.75$. The gap between early and late arrival time trajectories is evident between $x_1^0 = -2.36$ and $x_1^0 = -2.44$. These arrival times were computed for trajectories evolving on the thin Eckart potential surface.

coordinates we chosen to be $x_2^0 = y_2^0 = 0$. The gap that is evident between $x_1^0 = -2.36$ and $x_1^0 = -2.44$ separates early arrival trajectories on the right $(t_A < 900)$ from those that arrive at later times $(t_A > 1800)$. Analysis of trajectories that fall within the gap shows that most of them make it to the product side of the barrier but they fail to pass through the real coordinate plane. A few trajectories close to the edge of the gap may show abnormally long arrival times, such as the one near the point $x_1^0 = -2.44$. Further analysis will be presented beginning in Section II D, where plots of the trajectories will be presented. In contrast, for the thick Eckart barrier scattering problem, the gap is pushed deeper into the complex plane so that the part of the arrival surface facing the real axis is quite smooth. The arrival time distribution for the Gaussian potential surface is qualitatively similar to that shown in Figure 24, with the exception that there is no gap separating two branches of the distribution.

B. Arrival Times and Isochrones

The set of transmitted trajectories having a designated arrival time t_A are launched from points, $(x_1^0, y_1^0, x_2^0, y_2^0)$, in the space of initial coordinates that lie on an *isochrone* (surface of equal arrival times). The projection of the isochrone into the subspace (x_1^0, y_1^0) is obtained by intersecting a horizontal plane at the value t_A through an arrival surface, such as the one shown in Figure 24. (The arrival time surface shown in this figure contains enough information to locate a large number of isochrones.) Because few, if any, trajectories arrive at exactly the time t_A, more trajectories can be sampled by generating isochrones from trajectories arriving within the time interval

$t_A - \delta t$ to $t_A + \delta t$, where the band width is small, $\delta t \ll t_A$. Figure 26 shows an example of three isochrones for the wave packet having the initial energy $E = V_0$. These projected isochrones, the intersections of the vertical lines with the (x_1^0, y_1^0) plane, were plotted for the arrival times t_A = 600, 1200, and 1800 and the width parameter was $\delta t = 50$. As t_A increases, the slope of the isochrone becomes more negative as points with more negative values of y_1^0 move closer to the vertical axis. For each value of y_1^0, there may be a small group of points with slightly differing values for x_1^0 within each isochrone. However, these x_1^0 values may be fit to a polynomial in y_1^0. In Figure 26, linear fits are shown for each isochrone. For the low energy tunneling problem described in this study, linear fits are not accurate when x_1^0 is near the center of the initial wave packet, so in practice cubic or quartic fits were used. Locating the isochrone for a specific arrival time is inefficient if a four-dimensional grid is searched in the Cartesian space $(x_1^0, y_1^0, x_2^0, y_2^0)$ of initial coordinates. An improved method will be described in the following section.

C. Isochrone Model

The goal is to locate the isochrone for transmitted trajectories with a specific arrival time t_A. The method developed in this section assumes weakly coupled vibrational and translational motions. We will first consider the vibrational motion, described by a quantum harmonic oscillator in complex coordinate space[62]. In terms of the complex coordinate z and the complex momentum $p = \partial S / \partial z$, the ground-state oscillator obeys the equation of motion $dp / dt = -kz$, where $k = m\omega^2$ is the force

Figure 26: Three isochrones for the thin Eckart Barrier

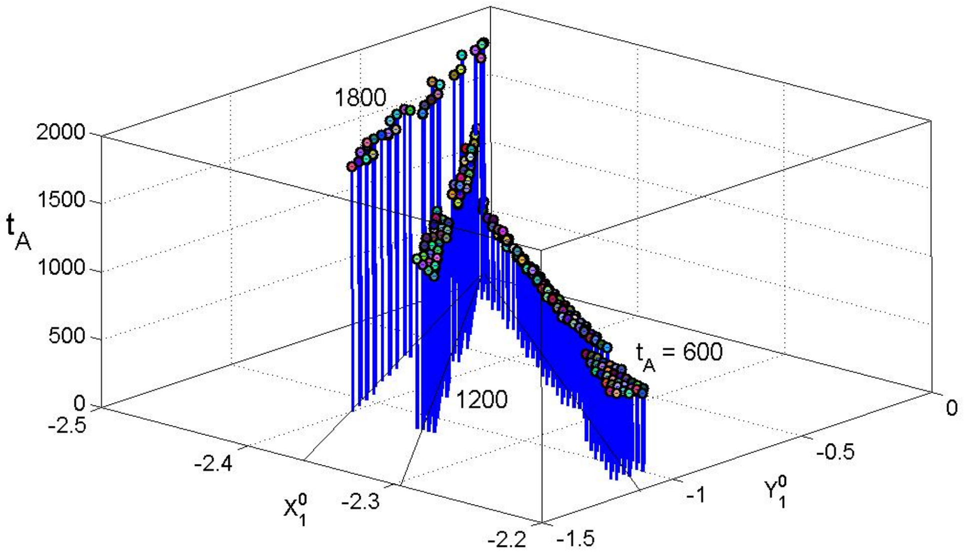

Three isochrones for wave packet scattering on the thin Eckart potential surface at $E = V_0$. For three arrival times, t_A = 600, 1200, and 1800, vertical lines down to the (x_1^0, y_1^0) plane locate the isochrones. Trajectories launched from an isochrone reach the real-valued subspace of the transmitted region ($x_1 > 0$) at the same time. Linear relation of the x_1^0 values as a function of y_1^0 are also shown for these isochrones.

constant. Since the momentum function is given by $p = im\omega z$, $z(t)$ obeys the equation $idz/dt = -\omega z$. The trajectory resulting from integration of this equation, $\mathrm{z(t) = R \cdot e\,xp[i(\omega t + \gamma_0)]}$, is a circle of constant radius R (the vibrational amplitude) in (x, y) space. The initial phase angle is γ_0 and the period of motion is $\tau = 2\pi/\omega$.

Consider a trajectory which starts from the point (x_0, y_0) with the initial phase angle (measured counter-clockwise from the positive x axis) given by $\gamma_0 =$ $\arctan(y_0/x_0)$. We will first assume that this angle is in the primary zone, $0 \le \gamma_0 \le \pi$. How long will it take for the imaginary coordinate to vanish as this phase point rotates counter-clockwise along the circular orbit? This *vibrational arrival time*, denoted by t_V, is determined by the ratio

$$\frac{\pi - \gamma_0}{\pi} = \frac{t_V}{\tau/2}. \tag{3.19}$$

The time to rotate onto the negative real axis is then given by $t_V = (\tau/2)\left[1 - \gamma_0/\pi\right]$. Of course, a point with the initial phase angle $\gamma_0 + \pi$ will rotate onto the positive real axis in the same amount of time. Conversely, if t_V is specified, the initial phase angle which leads to this arrival time satisfies the equation

$$\gamma_0 = \pi\left[1 - \frac{t_V}{\tau/2}\right]. \tag{3.20}$$

In general, if we specify an arbitrary arrival time, we first need to subtract m multiples of the half-cycle in order to find a rotation time which is no larger than a half-cycle, $t_A - m\cdot(\tau/2) \le \tau/2$. This adjusted arrival time is the first arrival time on either the positive or negative real axis. Introducing the modulus function, the initial phase angle is given by

$$\gamma_0 = \pi\left[1 - \frac{\mathrm{mod}(t_A, \tau/2)}{\tau/2}\right]. \tag{3.21}$$

This equation conforms to the feature that trajectories with different R values, all of which lie on the line having the slope $\tan(\gamma_0)$, will cross the real axis at the same time.

In order to incorporate the translational motion, we will first determine the isochrone for transmitted trajectories (again, with the arrival time t_A) for which the initial vibrational amplitude is zero, $R = 0$. As indicated in the preceding section, this could be accomplished by selecting a small number of fixed values (maybe 10) for y_1^0 followed by variation of x_1^0 along each slice to locate the trajectories which have the desired arrival time. These values for x_1^0 could then be fit to a low-order polynomial in y_1^0. In order to locate the isochrone for a specified value of y_1^0 when $R > 0$, the initial vibrational phase angle γ_0 is obtained from equation (3.21) by substituting the specified arrival time. Trajectories could then be launched from points along this line for a series of values of the vibrational amplitude R. For each value of the pair (y_1^0, R), the coordinates x_1^0 and γ could then be adjusted to achieve fine tuning of the arrival times. The isochrone determined through this procedure is then specified by the four coordinates $(x_1^0, y_1^0, R, \gamma)$.

The dependence of the arrival time for transmitted trajectories upon the initial phase angle for the oscillator is shown in Figure 27. The modulus of the arrival time for these trajectories, defined by $t_M = \mathrm{mod}(t_A, \tau/2)$, is shown as a function of γ_0 for constant

Figure 27: Modulus of the arrival time for initial phase angle γ_0

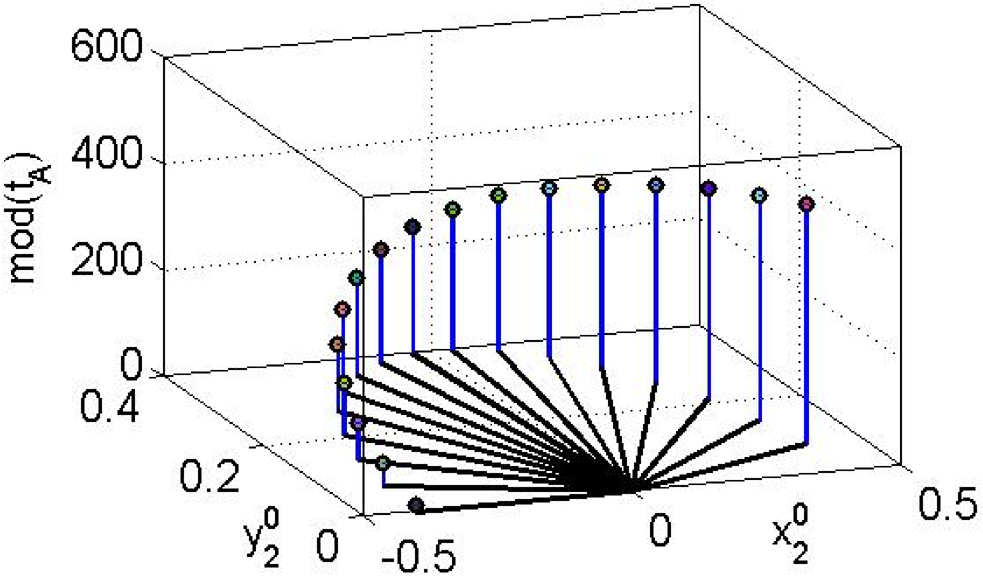

Modulus of the arrival time, $\mathrm{mod}(t_A, \tau/2)$, for 17 values of the initial phase angle γ_0 (measured counter-clockwise from the positive x_2^0 axis). For these trajectories, the initial amplitude of the oscillator was $R = 0.4$ and $y_1^0 = -0.6$. These trajectories were run on the thin Eckart barrier potential energy surface.

values for two of the coordinates, $y_1^0 = -0.6$ and $R = 0.4$. In accord with equation (3.21), the arrival time t_M decreases to zero as $\gamma_0 \rightarrow \pi$.

In Figure 28, isochrones for the arrival time $t_A = 1200$ are shown for trajectories propagated on the Gaussian potential energy surface. The trajectory results (dots), shown for two initial vibrational amplitudes, indicate a slight dependence upon the initial value of R. This dependence arises from translation-vibration coupling in the potential energy surface, a feature which was ignored in the model described earlier in this section. In addition, this plot illustrates bending of the isochrones as x_1^0 approaches the center of the initial wave packet (at -2.5). The figure also shows cubic polynomial fits (red curves) to the trajectory data.

D. Trajectory Diffraction around Poles

A prominent feature of trajectory evolution on the thin Eckart barrier potential energy surface is diffraction around the poles in the complex extended potential. Depending upon the initial conditions, trajectories approaching a pole may divert upward toward the real axis, or down toward more negative values of y_1. Figure 29 shows an example for two trajectories having the same arrival time, $t_A = 1200$. The trajectory launched from $y_1^0 = -0.85$ (the right trajectory in this figure) diverts around the pole toward more negative values of y_1, while the other trajectory, launched closer to the real axis from $y_1^0 = -0.60$, diverts to the left around the pole. A second example concerns short and late arrival time trajectories which are launched from the same value of y_1^0, as

Figure 28: Isochrones for two initial vibrational amplitudes

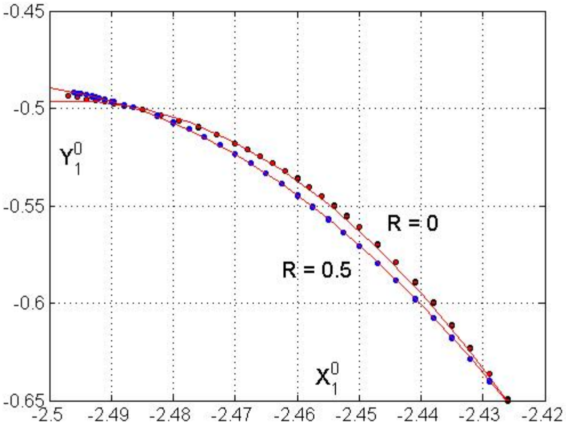

Isochrones for two initial vibrational amplitudes, $R = 0$ and 0.5. The trajectory results are shown by dots and cubic polynomial fits are shown as (red) curves. These trajectories were run on the Gaussian potential energy surface.

Figure 29: Two trajectories diverting around an Eckart pole in 2-D

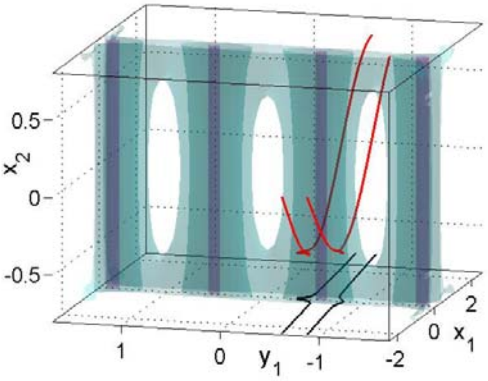

Two trajectories (on the thin Eckart barrier potential surface) diverting around the pole in the potential energy at $z_1 = -0.523i$. Three isosurfaces of the absolute value of the potential are also shown. The trajectory launched from $y_1^0 = -0.85$ diverts to the right around the pole while the second trajectory, launched from $y_1^0 = -0.60$, diverts to the left. Both trajectories start with the vibrational coordinates $R = 0.5$ and $\gamma = 1.407$ and they have the same arrival time, $t_A = 1200$. Projections of the trajectories in the lower horizontal plane are also shown.

mentioned earlier in regard to Figure 25. Figure 30 shows the projection of several early and late arrival time trajectories in the (x_1, y_1) plane, all of which were launched from $y_1^0 = -0.85$. The early arrival time trajectories were launched from values of x_1^0 on the leading edge of the initial wave packet. In contrast, the late arrival trajectories had values for x_1^0 which were closer to the center of the initial wave packet. Between these two groups of trajectories lies a gap in the arrival times. Trajectories launched from within the interval Δx_1^0 do not cross the real plane even if they make it to the transmitted side of the barrier.

E. Transmitted Wave Packets on Thin Barriers

The wave function and the density may be computed from the action function transported by each trajectory as it crosses the real plane on the transmitted side of the barrier. Results will be shown for the arrival time $t_A = 1200$, a time for which the transmitted and reflected wave packets are well bifurcated. For trajectories evolving on the thin Eckart potential surface, Figures 31 and 32 display two views of the transmitted wave packet, one showing the backside of the packet (Fig. 31) and the other showing a side view (Fig. 32). In this figure, the probability density is plotted at the position of each trajectory at the designated arrival time, $t_A = 1200$. Figure 32 shows that the density suddenly declines near $x_1 = 5.4$. Additional trajectories arrive in the interval $x_1 = 7 - 8.5$, on the leading edge of the packet, but they carry very low densities ($\rho < 10^{-4}$) and were not plotted. This gap in the transmitted density arises from the gap

Figure 30: Early and Late Arriving Trajectories Diverting around a Pole

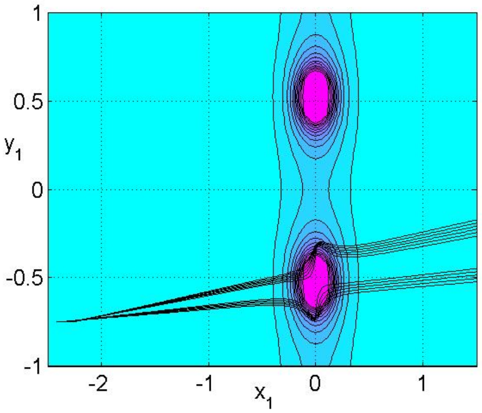

Projection into the (x_1, y_1) plane of early and late arrival time trajectories launched from $y_1^0 = -0.85$. The early arrival trajectories ($t_A = 450 - 600$), launched from starting positions in the interval $x_1^0 = -2.26$ to -2.30, divert up around the pole. The late arrival time trajectories ($t_A = 1000 - 1300$), launched from starting positions in the interval $x_1^0 = -2.38$ to -2.41, divert downward around the pole. Trajectories launched within the gap from $x_1^0 = -2.30$ to -2.38 do not cross the real plane on the product side of the barrier. Contours of the absolute value of the thin Eckart potential are also shown.

Figure 31: Transmitted Wave Packet for Thin Barrier Eckart Scattering (back)

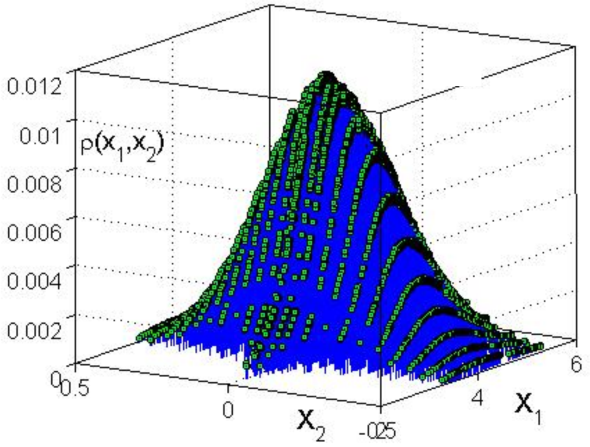

Probability densities (dots) at the trajectory positions for the transmitted wave packet when the energy is $E = 0.25\,V_0$. These trajectories propagate on the thin Eckart potential surface for the arrival time $t_A = 1200$. View from the backside of the transmitted packet.

Figure 32: Transmitted Wave Packet for Thin Barrier Eckart Scattering (side)

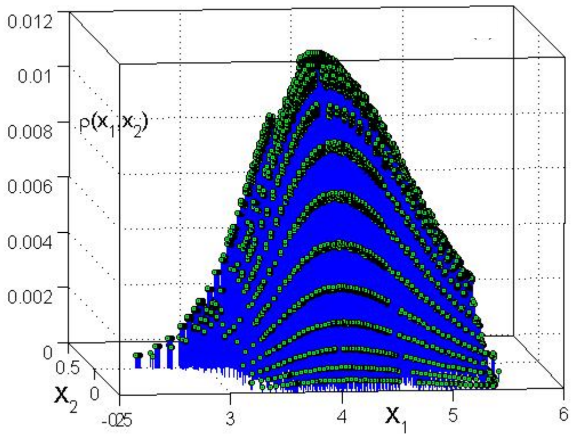

Side view of the packet shown in Figure 31, showing the sudden fall-off in density near $x_1 = 5.4$.

shown earlier in Figures 24 and 25 for the arrival time distributions. Unfortunately, classical trajectories propagating in the complex plane are excluded from populating the gap region in the transmitted wave packet. Even so, by interpolating the density across the gap, it is still possible to integrate the density to obtain the transmission probability at this arrival time. Integration of the trajectory densities gives $P_{trans} = 0.0106$, which compares with 0.0128 from direct numerical integration of the time-dependent Schrödinger equation using a large space fixed grid.

In contrast, for trajectories evolving on the Gaussian potential surface, there is no gap in either the isochrone or the density for the transmitted packet. Figure 33 shows a front view of the transmitted packet for the same arrival time used previously. For this smooth density, the transmission probability is $P_{trans} = 0.0094$, compared with the accurate value (computed on a large space fixed grid) of 0.0116. For both potential energy surfaces, the transmission probabilities computed from complex classical trajectories slightly under-estimate the accurate values. (The density predicted by the trajectory calculations is somewhat smaller than the accurate values near the density maximum and on the backside of the transmitted packet.)

F. Transmitted Wave Packets on Thick Barriers

For the thin Eckart and Gaussian potential energy surfaces, the potential barrier has a slightly smaller half-width than the initial wave packet, as shown in Fig. 34. The thick Eckart barrier shown in this figure has about twice the width of the thin barrier and is broad in comparison with the initial wave packet. For this case, the barrier and wave packet widths bear the same ratio as those used in the recent study by Goldfarb et al. The

Figure 33: Probability Density for Transmitted Gaussian Wave Packet

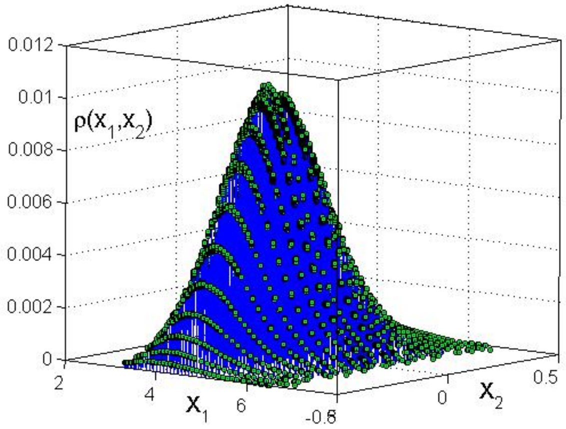

Probability densities (dots) at the trajectory positions for the transmitted wave packet. These trajectories propagate on the Gaussian potential surface for the arrival time $t_A = 1200$.

Figure 34: Thin and Thick Eckart Barriers Compared to initial Wave Packet width

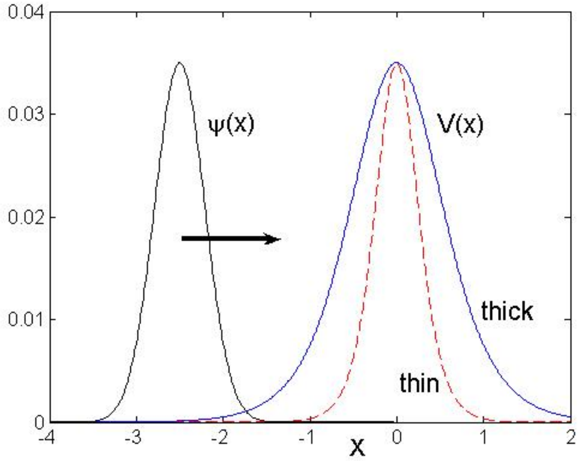

Absolute value of the initial wave function and the thin and thick Eckart barriers plotted along the real axis. The wave function has been scaled to have the same height as the potential barrier.

thick barrier is more ‘classical’ in the sense that less tunneling occurs at low scattering energies. In addition to the results described above for the thin Eckart barrier, we have used CVDPM(2) trajectories to study low-energy barrier transmission for the thick Eckart barrier multidimensional potential surface. For this case, the first pair of poles in the complex extended potential are far enough from the real axis so that complex trajectories can make it to the real plane in the transmitted region without forming a significant gap on the leading edge of the packet. The resulting transmitted packet looks similar to the one displayed for the Gaussian barrier in Figure 33, although the maximum density is about 60% of the value shown in this figure. In this case, the transmission probability from the trajectory calculation is about 95% of the exact value (0.00914).

G. Quantum Trajectory Results

The results reported so far have all been based upon CVDPM(2) complex-valued classical trajectories. We will now briefly explore some results obtained using the next higher order of DPM, namely CVDPM(3). In contrast to CVDPM(2) where there were 8 equations of motion to integrate for each trajectory, in CVDPM(3) there are now 12 equations; the additional 4 equations of motion are for the third order derivatives of the action function. An important feature is that each trajectory in now under the influence of both classical and quantum forces. An example of complex valued CVDPM n=2 and n=3 trajectories is shown in Figure 35 for motion on the thin Gaussian potential energy surface. Although launched from nearly the same point, the trajectories separate as they pass the barrier region near the center of the figure. As a result, different densities are transported to the transmitted region by these two trajectories.

Figure 35: Quantum Trajectories on the Gaussian Potential Surface

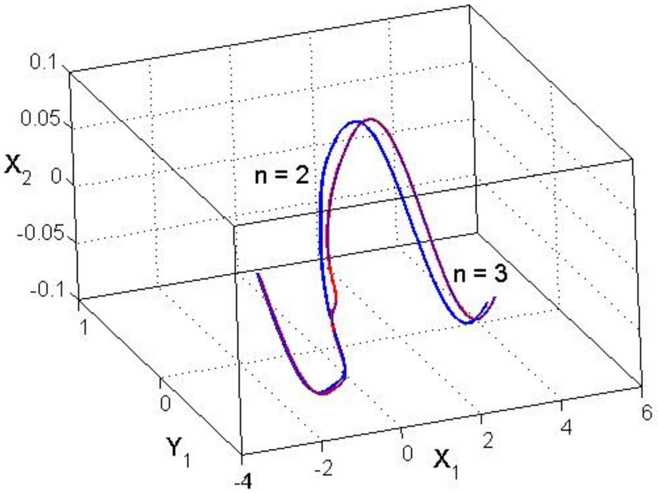

Quantum trajectories computed on the thin Gaussian potential energy surface: CVDPM(2) (blue curve); CVDPM(3) (red curve). These trajectories were launched with the initial vibrational amplitude $R = 0.1$ and they pass through the real product plane at the arrival time $t_A = 1200$. The propagation time was $t = 1300$ a.u.

Slices through the transmitted densities (the $x_2 = 0$ slice through the middle of the packet) are shown in Figs. 36 and 37 for the thick Eckart barrier and the intermediate width Gaussian barrier (the width parameter is $\beta = 4$). For the latter potential, the thickness is intermediate between the two barrier potentials shown in Fig. 34. For the thick Eckart barrier, where the first pair of poles is relatively far from the real axis, smooth densities were obtained for both orders of CVDPM (n=2 red dots, and n=3 blue dots) and these densities are in agreement with the exact density (blue curve). The only deviation is that the trajectory densities are slightly lower than the exact density on the backside of the transmitted packet. Transmitted densities were also computed for several barriers which were thinner than this barrier. An example is shown in Fig. 37 for the intermediate width Gaussian barrier. Unlike the previous example, the DPM results for n=2 and n=3 do not always agree well with each other. In addition, it is seen that the n=2 and n=3 densities near the maximum of the density slightly underestimate or overestimate the exact density, respectively. Although not shown here, there is even greater divergence for n=2 and n=3 densities when the barrier becomes thinner. The dependence of quantum trajectory results upon the barrier thickness is being investigated, but it appears that thin barriers accentuate inaccuracies in the DPM trajectories.

Figure 36: Probability densities computed on the thin Eckart Barrier

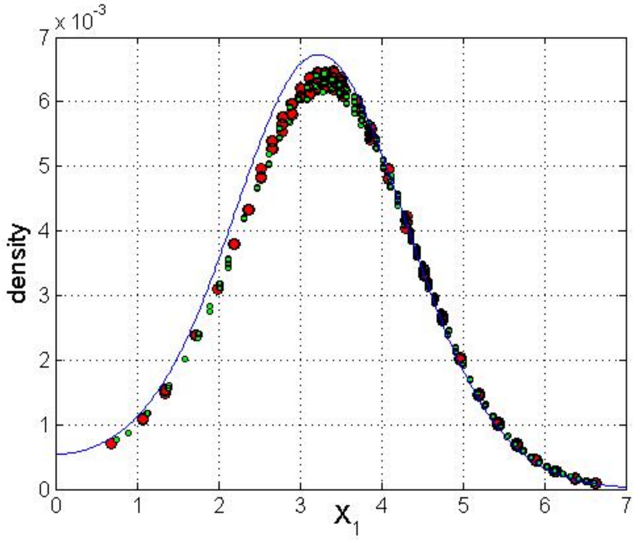

Probability densities computed for trajectories on the thick Eckart potential energy surface: CVDPM(2) results (large red dots); CVDPM(3) results (small green dots) . Exact results from a large fixed grid calculation are also shown (blue curve). These densities are shown along the $x_2 = 0$ slice through the transmitted wave packet.

Figure 37: Probability densities computed on the intermediate width Gaussian Barrier

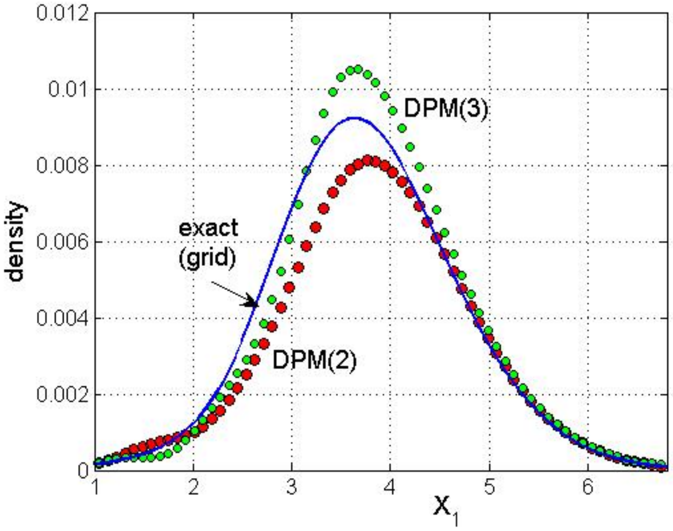

Probability densities computed for trajectories on the intermediate width Gaussian potential energy surface: polynomial fit to CVDPM(2) results (large red dots); fit to CVDPM(3) results (small green dots) . Exact results from a large fixed grid calculation are also shown (blue curve). These densities are shown along the $x_2 = 0$ slice through the transmitted wave packet.

V. Conclusions

A. Summary of Results

In this chapter, complex valued classical trajectories (2^{nd} order CVDPM), along which is transported approximate quantum phase information, were used to study low energy barrier transmission for a two degree of freedom system involving relatively thin barriers (compared with the width of the initial wave packet). The arrival time for trajectories to reach the transmitted (product) region was studied as a function of the initial coordinates of the trajectories. A swarm of trajectories launched from an isochrone[26], all reach the real valued subspace in the transmitted region at the same time. Results obtained using higher-order quantum trajectories (3^{rd} order CVDPM) were briefly described for both thick and thin barriers. The thin Eckart barrier presents problems because trajectories must diffract around poles in the complex extended potential surface which are relatively close to the real axis. However, for the Gaussian barrier (which has essential singularities far from the real axis) or the thick Eckart barrier (where the poles are relatively far from the real axis), the low-order CVDPM barrier transmission probabilities are in good agreement with exact (fixed-grid) results.

The benefits of running complex quantum trajectories are numerous. For example, good transmission probabilities are obtained for some potentials using low order DPM and even classical complex trajectories may give very good results[59,26]. In addition, new viewpoints may arise concerning quantum effects. For example, the work by Yang has provided new insights into stationary state one-dimensional barrier tunneling[64] and the origin of spin quantization[68]. There may also be disadvantages connected with the use of complex trajectories. For example, it may be computationally demanding to locate isochrones in barrier transmission problems. In addition, singularities in the complex-extension of the potential energy surface may present difficulties for the propagation of quantum trajectories.

The computational tack of locating isochrones is similar to the root search problem in semiclassical mechanics[90] and methods introduced there[91] may prove useful for this problem. The solution of two point boundary problems is generally handled with shooting methods and some of these techniques may also turn out to be useful[92]. A more detailed study of isochrones and barrier transmission probabilities for both thick thin barriers has is in publication[81], and the use of non-Lagrangian complex quantum trajectories[77] in barrier scattering problems will be explored in the next chapter.

Chapter 4: Complex Quantum Trajectories *sans* Isochrones: Arbitrary Lagrangian-Eulerian Trajectories in One Dimension

I. Introduction and Outline

A. Motivation

Previous chapters[26,75] have shown that Lagrangian CVDPMs may be difficult to use in practice due to the *isochrone* problem. In effect, one must search for the initial conditions on the quantum trajectories which will allow them to arrive on the real axis at a specified arrival time t_a, where they are detectable. The curve (or surface) of these initial conditions is known as an isochrone: any trajectory launched from a point on this curve is guaranteed to arrive on the real axis (or real subspace) at the time t_a. As an interesting example unrelated to quantum dynamics, the 2 hour drive-time isochrone to Heathrow Airport in London can be viewed[93]. Computation of the isochrone is reminiscent of the familiar "root-searching" problem from semi-classical dynamics[90,94].

CVDPM has many strengths, however. Increasing the order of CVDPM forces convergence toward a solution, and the convergence may be better than for Bohmian DPM[26]. CVDPM has been readily extended to higher-dimensional problems[75]; CVDPM has the promise to offer significant computational advantages over traditional methods—if but for the isochrone problem.

In order to address the isochrone problem, it will be necessary to exercise *complete control* over the trajectories (where they go and how fast they trek and thereby circumvent the isochrone search problem), and another set of dynamical approaches will be utilized, namely arbitrary Lagrangian-Eulerian (ALE) schemes. These schemes have a long history[95,96], having been introduced into classical fluid dynamics by Brackbill and by Hirt in the early 1970s. In these schemes, the trajectories are not fixed in space, nor do they move in Lagrangian fashion, driven by the gradient of the action. Control of the trajectories is incorporated by *defining* the velocity field, either before the dynamics is executed, or on-the-fly as the trajectories propagate. A byproduct of this approach is that the dynamics may be stabilized, so that longer propagation times may be achieved. The ALE methodology was first utilized in quantum trajectory calculations by Wyatt and coworkers[18-25] in 2003-2004. In addition, Kendrick and coworkers[43-45] have also used ALE methods to stabilize ensembles of quantum trajectories undergoing barrier scattering.

In this chapter, trajectory solutions to the CQHJE are presented in the *ALE* frame (which will be referred to as ALE/CVDPM). This serves to make the isochrone problem more tractable, as the isochrone curve, in effect, condenses to one (at most a very few) points in the complex plane. The ALE path through the complex plane, which can have an arbitrary velocity, can be explicited so as to avoid problem regions, such as poles in the complex potential energy. The simplest choice was made, namely constant velocity rectilinear trajectories.

B. Outline of Chapter

This chapter is organized as follows: Subsection II discusses the CVDPM and the equations-of-motion for ALE trajectories, subection III discusses the setup of the model problems as well as the numerical tools utilized. The Metastable Well and its extension to the complex plane is explored. Subsection IV presents computational results and analysis for both constant velocity rectilinear trajectories which originate in the complex plane and for complex trajectories which are confined to the real axis. Finally, in subsection V conclusions are presented.

II. Theory

A. Arbitrary Lagrangian-Eulerian Trajectory Equations

To obtain the equations-of-motion for CVDPM, one begins by substituting the *ansatz* $\psi(z,t) = \exp\left(iA(z,t)/\hbar\right)$, where $z = x + iy$ and $A(z,t)$ is the complex-valued action function, into the complex-extended TDSE. A single complex-valued equation for the action is obtained,

$$\frac{\partial A}{\partial t} + \frac{1}{2m} A_1^2 + Q_C + U = 0, \tag{4.1}$$

where U is the complex-extended potential. This equation is the complex-extended quantum Hamilton-Jacobi equation, expressed in the *Eulerian* frame. In all equations of motion, subscript notation is employed to denote partial differentiation with respect to *z*, $G_n = \partial^n G / \partial z^n$. In Equation (4.1), Q_c represents the complex-valued quantum potential (which is distinct from the Bohm quantum potential[71]) which has the form $Q_C = -\left(ih/\left(2m\right)\right) A_2$.

In order to obtain a trajectory solution to Equation (4.1), it is customary to place the equation in the *Lagrangian* frame. This is accomplished via the transformation

$$\frac{d}{dt} = \frac{\partial}{\partial t} + v \frac{d}{dz}, \tag{4.2}$$

where the flow velocity is $v_{Lag} = A_1 / m$ (the de Broglie guidance condition). In this study, however, we will utilize a hybrid approach between the Eulerian and Lagrangian frames; this is achieved by introducing any *arbitrary value* for the velocity v in equation (4.2). Inserting equation (4.2) into equation (4.1) gives the ALE equation-of-motion for the complex action function,

$$\frac{dA}{dt} = -\frac{1}{2m} A_1^2 - U + \frac{i\hbar}{2m} A_2 + vA_1. \tag{4.3}$$

This equation is solved simultaneously with the trajectory guidance equation, $dz(t)/dt = v(t)$. Note that for a Gaussian wave packet the initial quantum potential (third term on the right hand side of equation (4.3)) would be a constant.

B. Derivative Propagation Method

Note that the evaluation of equation (4.3) requires knowledge of A_1 and A_2 along the evolving trajectory. Approximate equations-of-motion for these spatial derivatives can be obtained by employing the DPM. Taking the first and second spatial derivatives of equation (4.1) and applying equation (4.2) gives two exact ALE equations for A_1 and A_2,

$$\frac{dA_1}{dt} = -\frac{1}{m} A_1 A_2 + \frac{i\hbar}{2m} A_3 - U_1 + vA_2, \tag{4.4}$$

and

$$\frac{dA_2}{dt} = -\frac{1}{m}\left(A_2^2 + A_1 A_3\right) + \frac{i\hbar}{2m} A_4 - U_2 + vA_3. \tag{4.5}$$

The exact ALE equation-of-motion for the spatial derivative of any order n can be obtained using the relation

$$\frac{dA_n}{dt} = -\frac{1}{2m}\left[\left(A_1^2\right)_n - i\hbar A_{2+n}\right] - U_n + vA_{1+n}. \tag{4.6}$$

Equations (4.4), (4.5) and (4.6) exhibit up-coupling to the next two higher-derivatives of A; the DPM equations-of-motion form an infinite hierarchy. No approximations have been made to this point.

In order to make progress, a truncation must be implemented so that a closed (albeit, approximate) set of equations can be solved. This is achieved by selecting an order n and setting all *higher* spatial derivatives of A equal to zero. Selecting n = 2, for example, yields a closed set of *approximate* equations,

$$\frac{dA}{dt} = -\frac{1}{2m}A_1^2 - U + \frac{i\hbar}{2m}A_2 + vA_1, \tag{4.7}$$

$$\frac{dA_1}{dt} = -\frac{1}{m}A_1A_2 - U_1 + vA_2, \tag{4.8}$$

and

$$\frac{dA_2}{dt} = -\frac{1}{m}A_2^2. \tag{4.9}$$

C. Integration of Flux

The quantity of interest in quantum barrier scattering calculations is the time-dependent transmission probability. In this study, the time-dependent probability on the real-axis was computed through the quantum-mechanical flux,

$$j(x,t) = \frac{\hbar}{2mi}\left(\psi^* \frac{d\psi}{dx} - \psi \frac{d\psi^*}{dx}\right) = \frac{\hbar}{m}\Im\left(\frac{i}{\hbar}A_1\psi^*\psi\right), \tag{4.10}$$

where ψ is determined by $\psi(x,t) = \exp\left(iA_0(x,t)/\hbar\right)$. The probability at point x at the arrival time t_a can be obtained through the time integral of the flux,

$$P(x,t_a) = \int_0^{t_a} j(x,t)dt. \tag{4.11}$$

The flux and probability are evaluated at a specific collection point. In this study, the origin was selected as the collection point.

III. Model Problems

A. Model Potentials

The initial wave packet on the real-axis is given by the Gaussian

$$\Psi(x) = \left(\frac{2\beta}{\pi}\right)^{\frac{1}{4}} \exp\left(-\beta\left(x-x_o\right)^2 + \frac{ip_o}{\hbar}\left(x-x_o\right)\right), \tag{4.12}$$

where the width parameter $\beta = 30\pi$, the center of the packet x_o = -0.7, the mass m = 30, and the initial momentum $p_o = \sqrt{2mE_0}$, where E_o is the average initial energy (which will range from 0 to 80). In this study, atomic units are used, and the parameters for the initial wave packet and Eckart potential are those employed by Tannor and co-workers[59]. Initial conditions for trajectories can be obtained via the analytic continuation of equation (11) into the complex plane ($x \rightarrow z$).

Complex-valued potentials can also be obtained through analytic continuation from the real-valued functions. In this study, three complex-extended potentials were employed. The first two potentials, the Eckart barrier, $V(z) = V_0 / \cosh^2\left(\alpha z\right)$, and the Gaussian barrier, $V(z) = V_o \exp\left(-\gamma z^2\right)$, have been previously studied and analyzed[22].

Briefly[87], the Eckart potential is classified as *meromorphic*, as it has a periodic series of isolated nodes located along the imaginary axis at $y = gi\pi/(2\alpha)$, where $g = \pm 1, \pm 2$, etc. and the Gaussian potential is classified as *holomorphic*, as it only has essential singularities at $z = \pm\infty$.

The third potential, the metastable well,

$$V(z) = \frac{V_0}{\varepsilon}\left[\frac{1}{2}m\omega^2\left(z - x_o\right)^2 - \frac{1}{3}\kappa\left(z - x_o\right)^3\right], \tag{4.13}$$

is shown along with an initial wave packet (for the real-valued problem) in Figure 38. It is interesting to note that this potential is a holomorphic function, as it has essential singularities located at $z = \pm\infty$. Parameters for the potentials are as follows: $V_o = 40$, $\alpha = 4.32$, $\gamma = 15.35$, $\varepsilon = 2.45$, $\omega = 1$, and $\kappa = 42.857$. All of the barriers have a maximum located at $x = 0$, $y = 0$ with a barrier momentum equal to 48.99 ($p = \sqrt{2mE}$). All barriers are considered to be "thick" barriers and for this case DPM is known to work well[26,75].

B. Numerical and Computational Methods

In these calculations, the implicit trapezoidal method was employed to integrate the set of CVDPM equations-of-motion. The trapezoidal method was chosen because it is known to handle stiff systems of equations well[87] and is easy to implement. A typical time step for integration was on the order of 10^{-2} to 10^{-3}. For comparison, "exact" barrier scattering probabilities were computed by applying standard second-order pseudo-spectral methods to the TDSE[9,10].

One of the main difficulties in implementing the CVDPM equations-of-motion in the Lagrangian frame is due to the *isochrone search problem*[26,59,75,81]. One must locate the isochrone for each arrival time of interest (meaning, multiple searches must be performed if one is interested in more than one arrival time), and in multiple dimensions this search can be time consuming. Implementing the CVDPM equations-of-motion in the ALE frame, however, allows one to replace the search for a curve with a search for one point (or possibly a very few). ALE methods allow one to control *where* the trajectory travels in the course of the computation; for example, it is desirable to avoid poles and singularities in the complex-plane and this can easily be done. In this study, a starting position $z_{initial}$, and a collection point on the real-axis, x_{obs} (which is the origin here), are selected. The velocity is arbitrarily determined for ALE trajectories; in this study, velocities were determined according to $v(t_a) = \left(x_{obs} - z_{initial}\right)/t_a$, where t_a is again the arrival time. By varying t_a, one can create a set of trajectories which follow a straight-line path (this path avoids all nodes and singularities) from $z_{initial}$ to x_{obs}, each of which has a *different* arrival time at the common observation point. Using the values $A_0(t_a), A_1(t_a)$, etc. transported along each trajectory, one can obtain the time-dependence of the flux for the complex probability fluid. Integration of the flux via equation (4.11) gives the time-dependent probability.

IV. Results

A. Rectilinear Constant Velocity Complex Trajectories

Figure 39 shows the absolute value of the complex-extended potential for the metastable well. Note that in the complex plane $\left|V(z)\right|$ forms a bowl-shaped structure with two wells. Lagrangian quantum trajectories for the metastable potential spiral out from the center of the initial wave packet (which is located at the minimum of the left-most well) and cross the real axis multiple times. In this study, however, ALE trajectories are only allowed to travel along the straight path shown in Figure 39. The

Figure 38: Real-Valued Initial Wave Packet and Metastable Well

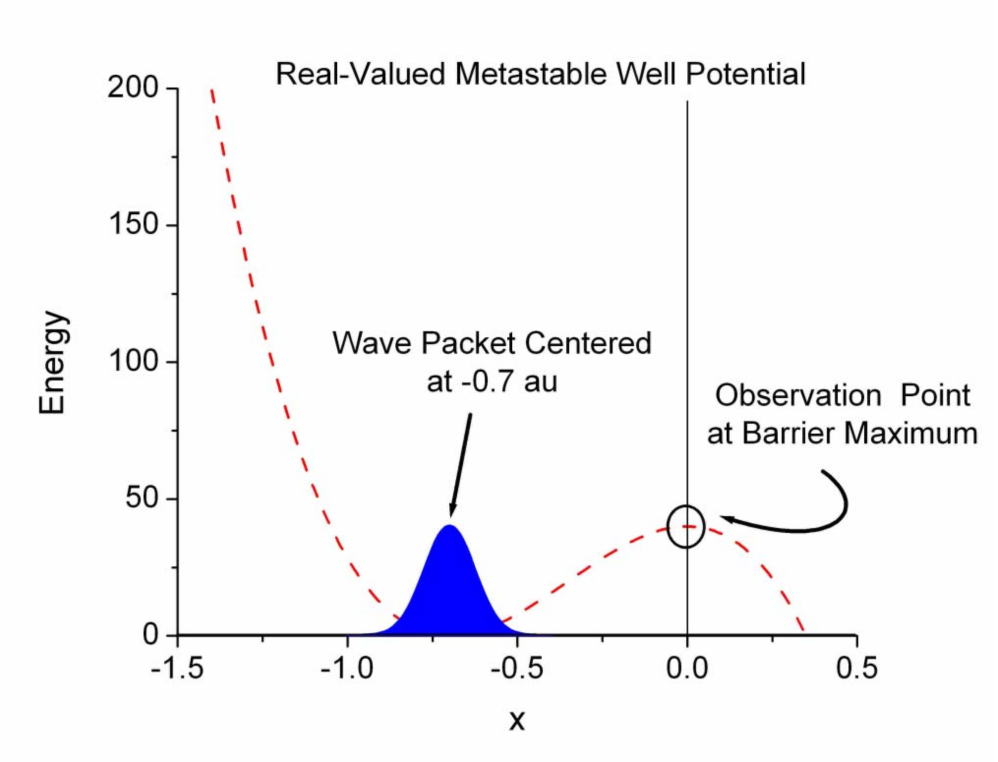

Real-valued metastable potential setup. The potential is shown by the dashed curve, and the initial wave packet by the solid curve. The observation point is also shown.

Figure 39: Absolute Value of the Complex-Extended Metastable Well Potential

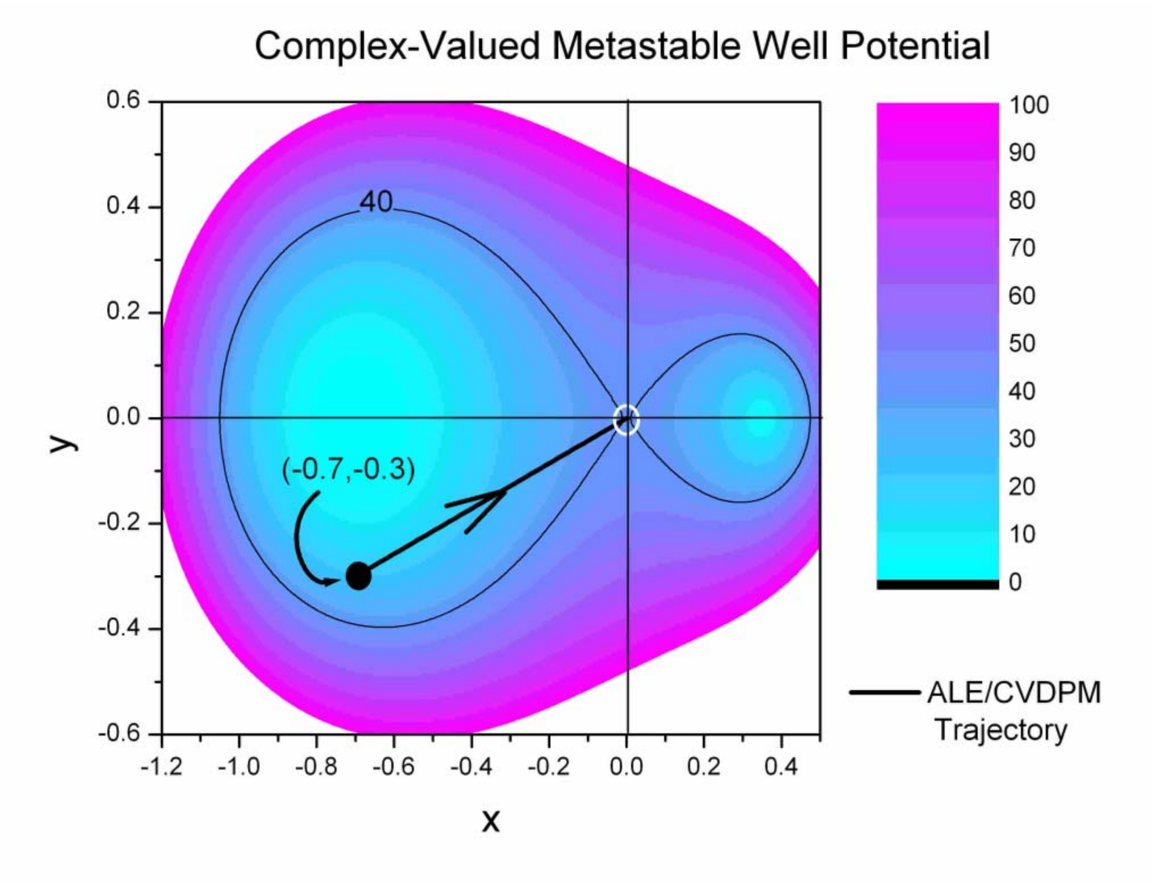

Absolute value of the complex-extended metastable potential. The contour representing the barrier height $E_o = 40$ is shown. The white circle denotes the observation point, and the ALE trajectory is represented by the solid line.

Observation point at $x_{obs} = (0,0)$ is also shown on the plot. This point is selected because it will allow computation of the time-dependent probability at any time *prior* to the final t_a ; this can be obtained by integrating the flux only to the time of interest.

In all calculations, the start point $z_{initial}$ can range from $x = -0.8$ to -0.7, while $y = -0.15$ to -0.4. Initial conditions for the three problems can be located within this area. One must do a manual search in order to find the appropriate "launch-point" (one that produces a smooth time-dependent flux with no unstable trajectories); however, for the potentials and energies investigated it was found that there was little variation in this starting position, and that once found for the lowest energy case, it required little refinement in order to obtain good transmission probabilities. There can be effects on the quality of the time-dependent flux if either the starting or the observation point are translated. We will return to this point later in this section. All calculations are performed for the arrival time of 1.5 au. The first launched trajectory permits calculation of the density at the observation point at $t = 0.05$; each subsequent trajectory will be launched with a decreased velocity such that its final time increases by 0.05 au, leading to a total of 31 trajectories being propagated for each initial wave packet energy (E_0) in order to cover the entire time interval of 1.5 au.

Figure 40 shows the time-dependent flux integral evaluated at $x_{obs} = (0, 0)$ for the deep-tunneling ($E_o = 0$) Eckart barrier scattering problem, while Figure 41 shows the same function for the high energy $E_o = 80$ problem. In both figures, the symbols represent the ALE/CVDPM result, while the continuous curve is the result as computed by the PSM. Notice that flux for $E_o = 0$ is about 10^{-6} of the flux when $E_o = 80$. Both of

Figure 40: Eckart Flux Integral for Deep Tunneling

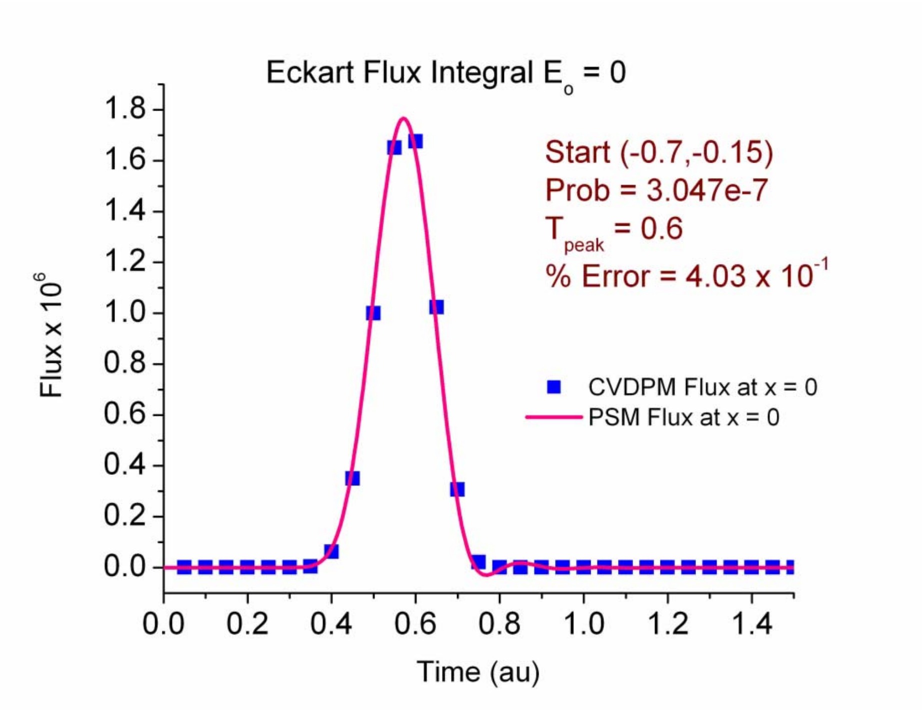

Calculated flux verses time for Eckart barriers for deep-tunneling, E_o = 0 case. The squares represent the value computed via ALE/CVDPM, the continuous curves by the PSM.

Figure 41: Eckart Flux Integral for High Energy Scattering

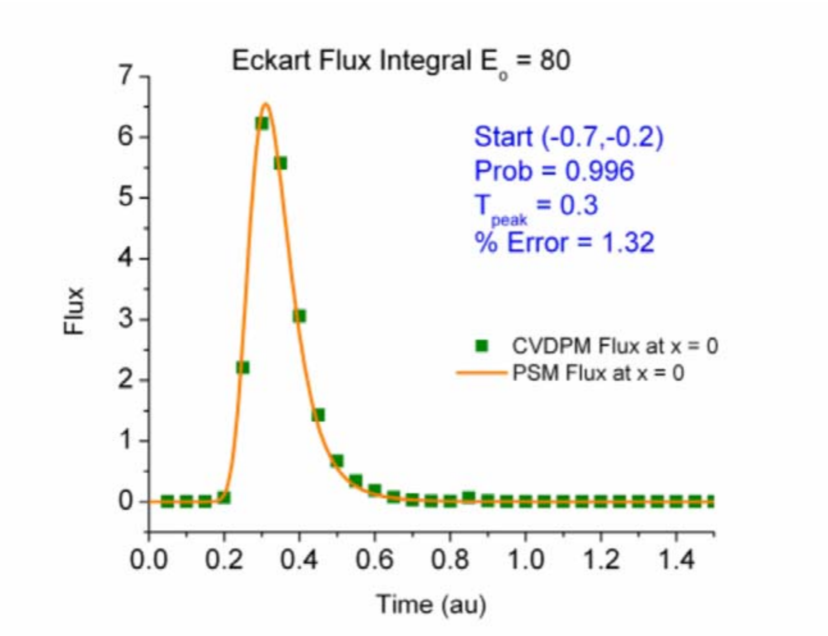

Calculated flux verses time for Eckart barriers for high-energy, E_o = 80 case. The squares represent the value computed via ALE/CVDPM, the continuous curves by the PSM.

These calculations were performed with CVDPM order 7. There is no algorithm for determining the best order of DPM for these types of calculations. Prior studies have shown that Lagrangian-frame CVDPM trajectories perform well at low-orders of DPM, while these calculations require higher-orders. A good rule of thumb to help in selecting an appropriate order of DPM is the polynomial smoothness of the potential energy surface. An infinitely smooth surface like the Gaussian or the Eckart will require a higher-order of DPM than one which can be represented by a low order polynomial. In addition, note that the deep-tunneling $E_o = 0$ case has a start point of (-0.7, -0.15) while the high energy $E_o = 80$ case has a nearby start point of (-0.7, -0.2). The maximum of the flux is recorded at $t = 0.6$ au for the $E_o = 0$ case, while it is recorded at $t = 0.3$ au for the $E_o = 80$ case. In both cases the error (computed by taking the percent error relative to the "exact" pseudo-spectral computation) is seen to be very low (less than about 1%).

Figure 42 shows time-dependent probabilities (see equation (4.11)) for the metastable well as computed by CVDPM orders 3 (circles), 4 (triangles), and 5 (squares) compared with the corresponding pseudo-spectral results (solid line) for the metastable potential over a range of initial wave packet energies. Figure 43 shows the same results for the Gaussian barrier but for orders 4 (stars), 5 (squares), 6 (circles) and 7 (triangles), while Figure 44 shows these results for the Eckart barrier for orders 5 (triangles), 6 (stars), and 7 (circles). Note in all cases that the results converge to the "exact" values obtained from the pseudo-spectral method. It is interesting to note that the orders required for "good" transmission probabilities utilizing ALE trajectories are significantly higher than the order required utilizing the Lagrangian frame (for both the Eckart and the Gaussian

Figure 42: CVDPM Results for Metastable Well Scattering

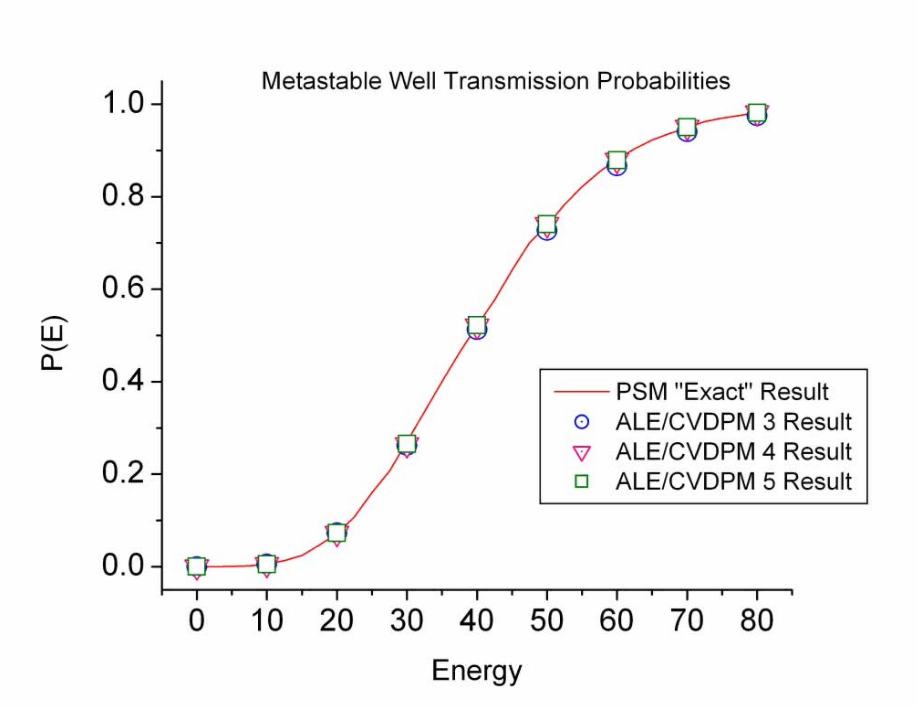

Integrated Flux for metastable well. The PSM results are represented by the solid lines, while the ALE/CVDPM results are denoted by symbols.

Figure 43: CVDPM Results for Gaussian Barrier Scattering

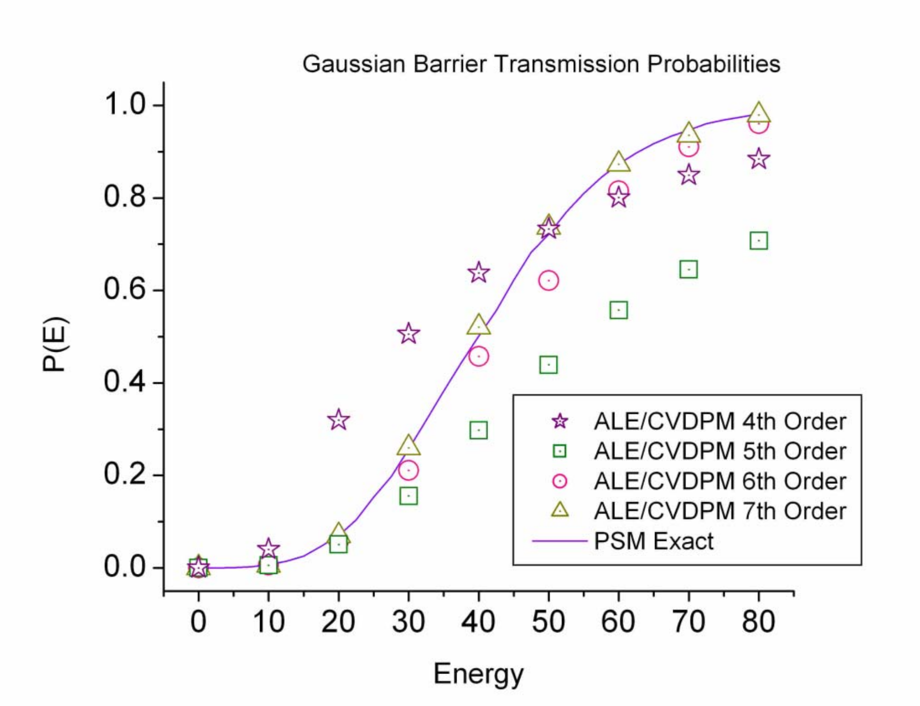

Integrated Fluxes for Gaussian barrier. The PSM results are represented by the solid lines, while the ALE/CVDPM results are denoted by symbols.

Figure 44: CVDPM Results for Eckart Barrier Scattering

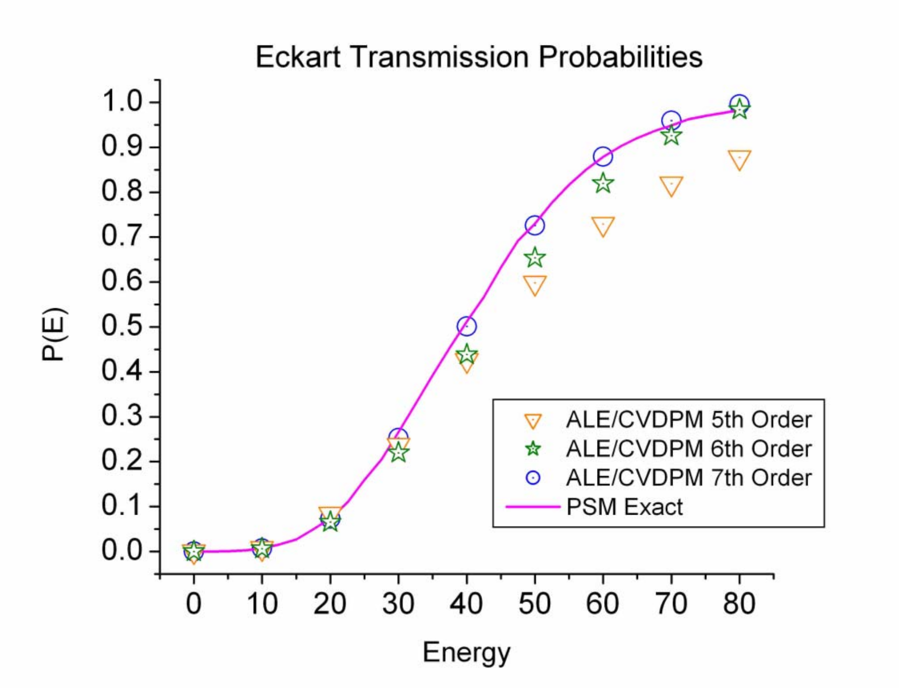

Integrated Fluxes for Eckart barrier. The PSM results are represented by the solid lines, while the ALE/CVDPM results are denoted by symbols.

Barriers, order 3 gives excellent transmission probabilities in the Lagrangian frame) when initializing the trajectory off of the real axis.

Figure 45 shows the relative errors in the computed transmission probabilities as compared to the PSM for all three potential surfaces (best cases) used in this study over the full range of energies examined. With exception of the results for $E_o < 20$, most results are found to be within 5% of the value computed via pseudo-spectral methods. In Fig. 46, the absolute error with respect to the PSM is shown logarithmically. These figures show that the ALE/CVDPM approach introduced in this study provides a good way of quickly estimating the quantum transmission probability for a variety of potential energy surfaces, as only 31 quantum trajectories were employed for the computation of the transmission probability at each energy.

B. Sensitivity of Initial Conditions and Collection Points

Figure 47 shows the sensitivity in the flux at the observation point with respect to changes in both $z_{initial}$ and x_{obs}. In this figure, the squares represent an optimal set of initial conditions and observation point: $z_{initial}$ = (-0.7, -0.15) and x_{obs} = (0, 0). The triangles represent the same $z_{initial}$ = (-0.7, –0.15) but a different x_{obs} = (0.22, 0). Finally, the circles represent a different $z_{initial}$ = (-0.75, -0.05) with the original collection point x_{obs} = (0, 0). Moving the collection point towards more positive values on the real axis has some effects upon the collected flux. First, the peak of the flux is seen to shift to later times, and the flux is broadened with respect to time. In addition, there are gaps in the collected flux in the areas denoted by the two boxes in Fig. 47: moving the collection point has the unintended consequence of introducing instabilities into the long-time behavior of the trajectories. Also, when one moves the collection point to more positive

Figure 45: Percent Error in Density for Three Potentials

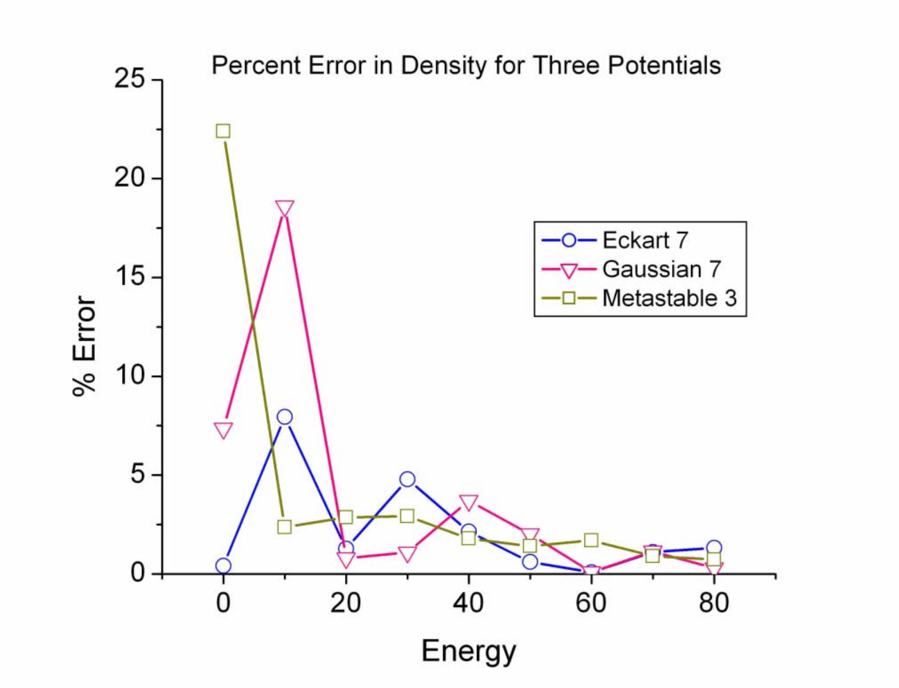

Energy dependence of Relative errors for the Eckart, Gaussian, and Metastable Potentials.

Figure 46: Absolute Error in Density for Three Potentials

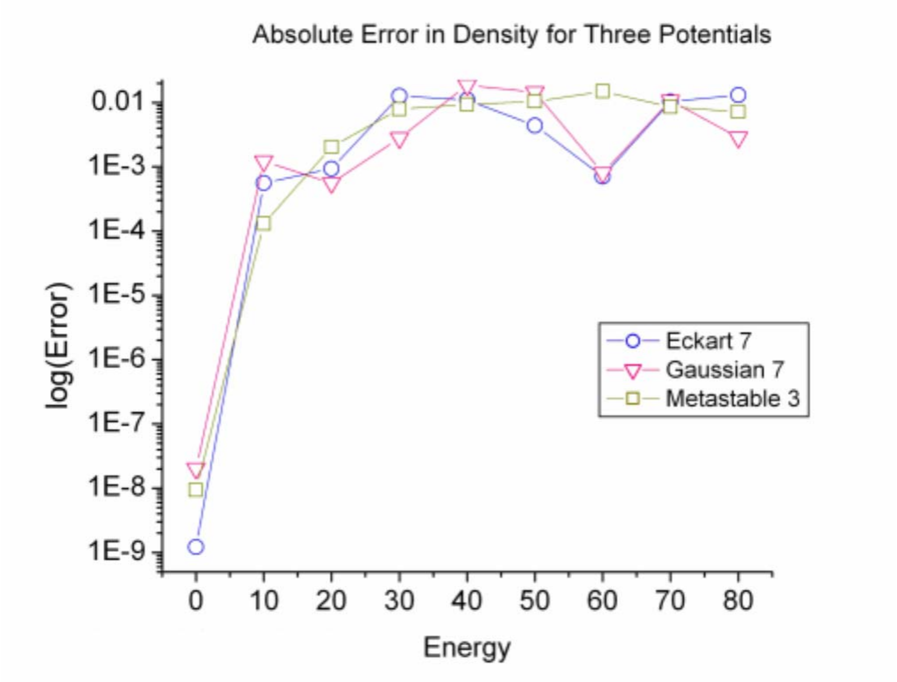

Energy dependence of Absolute errors for the Eckart, Gaussian, and Metastable Potentials.

Figure 47: Positional Variation in Fluxes

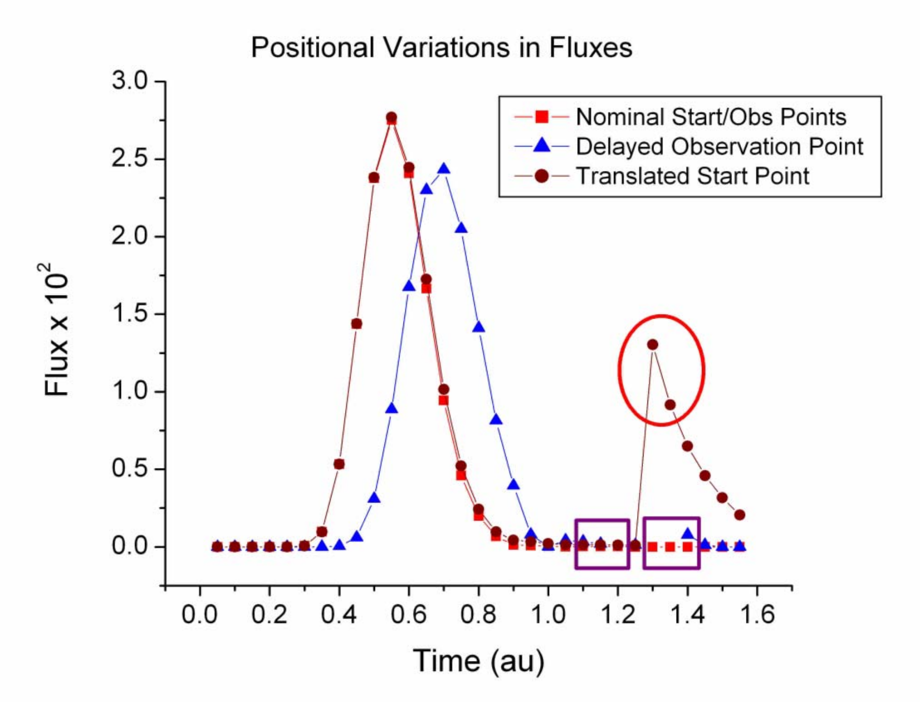

Sensitivity of flux integrals to changes in the start and collection points. Boxes show gap areas for delayed observation points; the circle shows a 'spike' in the transmitted flux which is most likely attributable to numerical imprecision.

values on the real axis one loses the ability to *easily* compute the time-dependent probability at any time prior to the final time, as the observation point will be well into the transmission region and will only record the flux of the complex probability fluid well after interaction with the barrier. If the observation point is moved far enough into the transmission region, for the specified arrival time the observation point may record no flux, as the transmitted wave packet may not have enough time to travel this far.

The effect of moving the starting point is also shown on Fig. 47. Note that the long-time behavior is impacted in this situation as well, as shown by the anomalous spike (near t = 1.4) denoted by the oval. Fortunately, these issues do not appear to have a significant effect on the final computed transmission probability, as long as one is careful to smooth out spikes and gaps in the collected flux prior to integration (each of the curves shown integrate to approximately the same probability). The cause of these numerical issues is not known at this point; it appears that there may be 'ideal' launch points which give trajectories exhibiting better numerical behavior than others (this might also be dependent upon the order of CVDPM utilized).

In Figure 47 it is seen that moving the start point towards the real axis yields the same transmission probability as a trajectory whose starting position is further off the real axis. The difference between these two cases lies in the long-time behavior of trajectories: starting at (-0.7, -0.3) was found to give a very smooth flux at all times of interest. Moving the starting position back towards the real axis can introduce anomalous spikes in the flux which must be removed by hand.

Currently, there is concern over the utilization of complex trajectory methods in that the analytic continuation of a potential from a *discrete* set of points on the real axis (as one would obtain from DFT calculations) poses an ill-defined numerical problem (in these studies the potential was analytically continued from a known function and its derivatives). This motivates us to see how ALE/CVDPM trajectories behave when they start at the center of the wave packet (here, x = -0.7) and are forced to propagate along the real axis. In this way, needed values of the potential energy surface can be obtained via interpolation while the derivatives of the potential can be obtained via simple, high-order finite differences.

C. Complex Trajectories on the Real Axis

Figure 48 shows the transmission probability in the Eckart barrier scattering problem for constant-velocity ALE/CVDPM trajectories which are initiated and forced to remain only on the real axis; this can be compared to off axis results in Fig. 44. The exact result as generated by pseudospectral methods is shown by the solid curve while CVDPM results are represented by circles (order 3), triangles (order 4), and stars (order 5). Note again that the results appear convergent as the order of CVDPM is increased, and that a lower order of approximation is required when compared to trajectories that start off the real axis (order 7 was needed to reproduce the exact result in the off-axis Eckart scattering case). The transmission probabilities for the metastable well computed via real axis confined ALE/CVDPM trajectories were in excellent agreement with the PSM calculation. It should be noted that confining ALE/CVDPM trajectories along the real-axis does *not* reduce these “complex” trajectories to real-valued Bohmian DPM trajectories. The action function *A(z)* is still a complex valued function, only evaluated

Figure 48: CVDPM/ALE Traj. Confined to Real Axis in Eckart Scattering

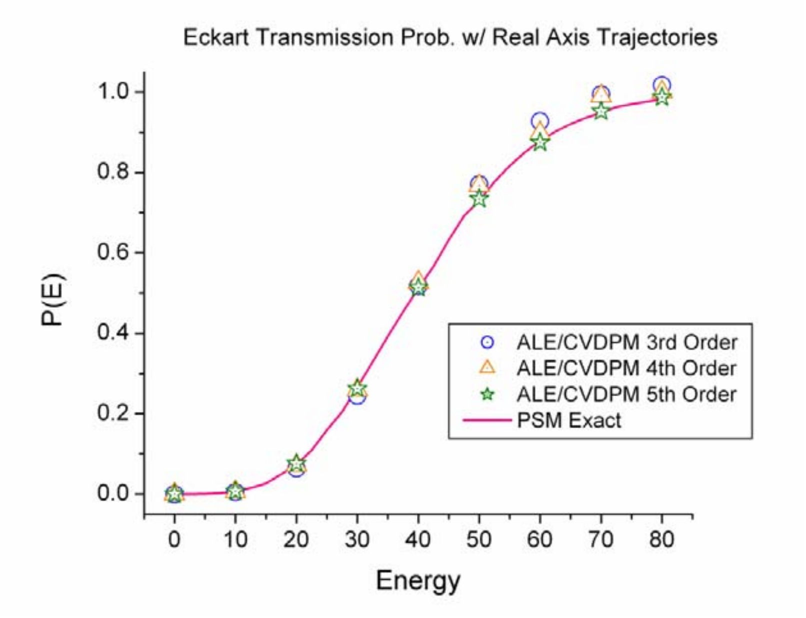

ALE/CVDPM integrated fluxes for the Eckart barrier using only constant velocity trajectories on the real axis. The exact result is denoted by a solid line, the ALE/CVDPM results by symbols.

along the real axis in this case. The momentum of the trajectories is real, as in the ALE framework the velocity of the trajectory is arbitrary and independent of gradients of the action (since both the initial and end points of the trajectories lie on the real axis we expect real velocity and consequently real momentum).

Confining the ALE/CVDPM trajectories to the real axis may reduce the order of approximation required to generate accurate results (a very promising development) but this comes at a price, however. It is possible for the computed fluxes in the Gaussian and Eckart barrier scattering cases for lower scattering energies (E = 10, 20 and 30) show spikes similar to those seen in Figure 47 at longer times ($t > 0.9$). However, when these spikes are removed by hand, the integration of the resulting function yields a probability that is very close to that obtained via PSM. It should be stated that for all energies examined, the peak of the flux is recorded well before any spikes arise in the flux, so the leading edge of the flux can be smoothed out with confidence. Not all energies were affected by these spikes. Extreme energies (very low and very high) performed exceedingly well, while moderate energies did have spikes that required hand removal.

V. Conclusions

A. Summary of Results

As discussed in chapter 2, one major difficulty with the use of Lagrangian-based complex-valued quantum trajectories is that it may require more computational effort to accurately locate isochrones than is required with more traditional methods of computing transmission probabilities. Also, the location of a single isochrone is specific for a particular arrival time; probabilities for other times require the determination of a new isochrone. As a way to circumvent both of the aforementioned problems, ALE-based CVDPM trajectories are presented for barrier scattering calculations. Through the use of arbitrary Lagrangian-Eulerian trajectories, one can specify start and observation points and exert absolute control over the path that the trajectory takes through the complex plane (to avoid poles, etc).

The advantages of ALE/CVDPM are numerous[26,75]. First, very few trajectories are required to accurately compute the transmission probability. Complex-valued trajectories are seen to be more accurate than their real-valued Bohmian counterparts at lower orders of DPM[26]. One of the reasons for this may be the forms of the quantum potentials in each case, as Goldfarb and co-workers have recently argued by this example: in Bohmian DPM, the initial quantum potential for a Gaussian wave packet is 'upside down' parabolic while equation (4.3) above shows that the quantum potential for a Gaussian wave packet in *complex* DPM is a constant. However, this does not account for the structure of the quantum potential in the Eckart or Gaussian scattering cases, when nodes may form in the reflected portion of the wave packet. This will be examined in further detail in the next chapter.

ALE/CVDPM trajectories are seen to be reasonably accurate, and they avoid the noxious isochrone problem. In addition, although complex-valued Lagrangian quantum trajectories have been successfully extended to two-dimensional barrier scattering problems[75], there may well be significant computational savings obtained through use of ALE/CVDPM trajectories when applied to multi-dimensional problems.

There are some difficulties in employing the ALE/CVDPM, among these are the selection of an appropriate starting point. Admittedly, it may take some searching in order to identify an appropriate launch point. However, once this point is located it does not change significantly over the energies studied. Even if a “bad” starting point is used, reasonable transmission probabilities can be obtained because numerical instabilities tend to appear at longer times in the flux calculation; these instabilities can easily be removed by excising the delinquent fluxes by hand, and the collected flux can then be extrapolated over missing data.

ALE/CVDPM trajectories have been shown to faithfully reproduce transmission probabilities with starting positions *both on and off the real axis*. It is not known why the accuracy of some late-time trajectories has a sensitive dependence on the starting position, but this does not appear detrimental to the method. The ability to confine trajectories to the real axis is a positive development, as potential energy surfaces as generated by DFT methods could conceivably be used without the odious process of numerical analytic continuation.

It should be noted that Tannor and co-workers have presented a method[76] (termed ZEVCA) which is similar in spirit to the work presented in this study. However, a distinct disadvantage of their method is that the initial wave packet and the potential must *initially* overlap significantly in order to provide initial conditions for “trajectories” which will be used to construct the wave packet. The method presented in this study does not suffer the same disadvantage, as the wave packet can be started ostensibly as far from the barrier as one would like.

Chapter 5: Recent Work, Future Directions, and Conclusions

I. Recent Work

A. Numerical Analytic Continuation

Much recent attention has been devoted to extending the CVDPM(n) to problems of interest. One of the main deficiencies in the method concerns the use of potentials which are discrete, real-valued potentials (as one would obtain through DFT). Also, without an analytic formula how does one obtain the derivatives of the potentials which appear in the equations of motion for CVDPM(n)? There are methods for performing this operation, known as Numerical Analytic Continuation. A brief overview of each method will now be presented.

Hass, Velický and Ehrenreich[97] proposed a method by which one can numerically extend a function from a line of constant y in the complex plane back to the real axis in 1983. The motivation for doing this was to avoid a pole in the complex plane during the integration of a Green's function. The method (which is valid for functions which are analytic in the upper half plane), repeatedly utilizes a Taylor series expansion around points which have already been determined. The result of their expansion is equation (5.1), which is used to generate the first row of points from the already known data points.

$$F_{n,m-1} = \frac{5}{2}F_{n,m} + \frac{1}{12}\left(F_{n-2,m} + F_{n+2,m} - 10F_{n-1,m} - 10F_{n+1,m}\right) + \frac{i}{6}\left(F_{n+2,m} - F_{n-2,m} - 5F_{n+1,m} + 5F_{n-1,m}\right), \tag{5.1}$$

Equation (5.1) is accurate to 4th order, however, it is seen that this equation requires terms from 2 data points away from the point of calculation. This means that for each slice one takes into the complex plane, four data points (two on the left, two on the right) will be lost with each application.

In order to cope with the lost data points in equation (5.1), the authors proposed equation (5.2) to continue the numerical extension of the function beyond the first slice.

$$F_{n,m-1} = 4F_{n,m} - F_{n,m+1} - F_{n-1,m} - F_{n+1,m}. \tag{5.2}$$

Equation (5.2) is accurate to 3rd order, however, one loses only two data points with each slice, rather than the four with equation (5.1) (see Figure 49). This method will be referred to as the Finite Difference (FD) method in the rest of this chapter. Eschrig, Richter and Velický subsequently published an error analysis[98] of the scheme in 1986.

Gray and Kaplan[99] proposed an alternative method for computing the numerical extension of Green's functions into the open half-plane. By employing the Cauchy condition[87] for analytic functions, shown in equation (5.3),

$$\oint_C g(z)dz = 0, \tag{5.3}$$

they were able to derive equation (5.4), which is termed the Cauchy Method in this chapter,

$$F_{n,m-1} = F_{n,m} + \frac{i}{2}\left(F_{n-1,m} - F_{n+1,m}\right). \tag{5.4}$$

The Cauchy Method is only 2nd order accurate, and one still loses two data points with each additional slice one goes into the complex plane. However, Gray and Kaplan are able to provide comparative error analyses for both the Finite Difference method and the Cauchy Method. The results of their analyses are very enlightening; they are able to show that the Cauchy Method is numerically more stable than the Finite Difference

Figure 49: Numerical Extension Methods

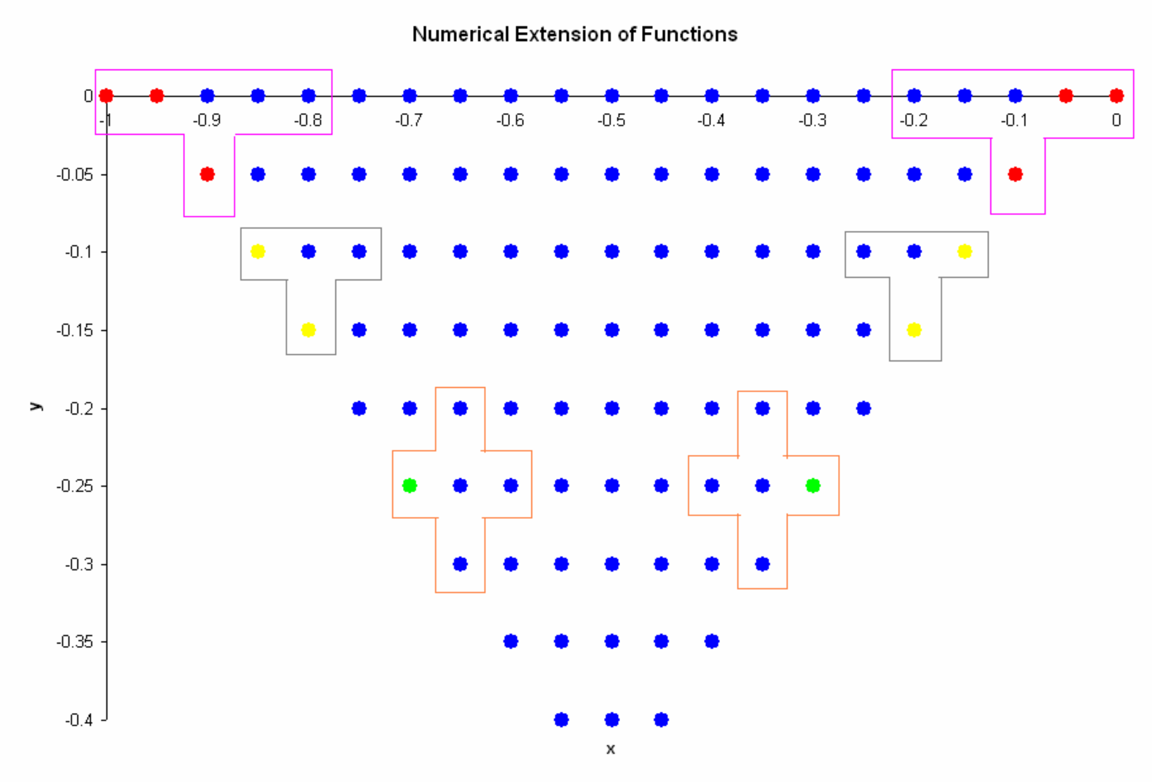

4th Order Finite Difference technique (lavender box) and the lost four data points (in red). Also shown is the 3rd Order Finite Difference technique (gray box) with lost two data points (in yellow) for subsequent slices. Finally, the Cauchy Method (orange cross) and the lost two data points (in green).

method. For example, if there is no error in the initial data, with a spacing $\Delta x = 0.3$ you can obtain ~20 slices with the Finite Difference method and ~50 with the Cauchy Method. In order to make the Cauchy Method competitive with the Finite Difference method with respect to accuracy, Gray and Kaplan provide an extrapolation technique that provides an estimation of the error, which can be used to improve the accuracy of the method.

Another method that we have employed in our recent work but without great success is based upon Fast Fourier Transforms and was proposed in 1996 by Natoli, Cohen and Fornberg[100] for the same Green's function problem as discussed above. They proposed equation (5.5),

$$G(x,0) = \frac{1}{2\pi} FFT^{-1}\left[e^{\frac{-k^2}{k_0^2}} e^{|k||y|} FFT\left[G(x',|y|) \right] \right], \tag{5.5}$$

where the term $e^{|k||y|}$ can be interpreted as the "update" to the next slice in the complex plane, and the term $e^{\frac{-k^2}{k_0^2}}$ is a dampening term that serves to stabilize the method. Miller and Thomas discussed numerical extension of functions in regards to semi-classical methods in 1972. They report to have had good success with Padè Approximants[101, 102], but we have not yet examined this method of numerical extension.

B. Numerical Analytic Continuation for Potentials

The motivation of this work is to extend a discrete potential energy surface defined on the real axis into the complex plane. Also, for the CVDPM(n) to be employed, not only must the potential be evaluated at each point in the trajectory's path, but the derivatives must also be computed as well. To study the accuracy of the methods discussed in Subsection A above and the effect of applying difference operators in order to compute derivatives, we will extend the discretized real-valued Eckart and Gaussian potentials into the complex plane.

Figure 50 shows the relative error of the numeric extension of the Eckart surface given in chapter 2, with contours given at 1% and 5% error. The numerical extension was performed with the Differencing Method (equations (5.1) and (5.2)) with a spacing between data points $\Delta x = 0.03$. The error is computed relative to the exact numerically extended potential equation (2.37). Note the location of the pole at $x \sim -0.35i$ in Figures 3, 4, and 50. The solid line on Figure 50 shows the path taken by the constant velocity rectilinear CVDPM(n) trajectory discussed in chapter 4. It can be seen that the potential is reproduced very well in areas where the function is analytic, and that for the majority of the trajectory's path it will encounter a numerically extended potential which is in error from the exact result by less than 1%.

Figure 51 shows the relative error of the numeric extension of the Gaussian surface given in chapter 2, with contours given at 1%, 5%, and 12%. The numerical extension was performed with the same methods and parameters as discussed for Figure 50, with the error computed relative to the exact potential, equation (2.38). Again, the path of the constant velocity rectilinear trajectory from chapter 4 is depicted. In this case, the greatest error in the function lies not on the imaginary axis as with the Eckart barrier, but towards more negative values of x. Note that at the trajectory's starting location $z_o = (-0.7,-0.3)$ lies on the 12% error contour, but that as the trajectory heads towards the collection point at the origin the error in the potential drops appreciably.

Figure 50: NAC of Eckart Potential

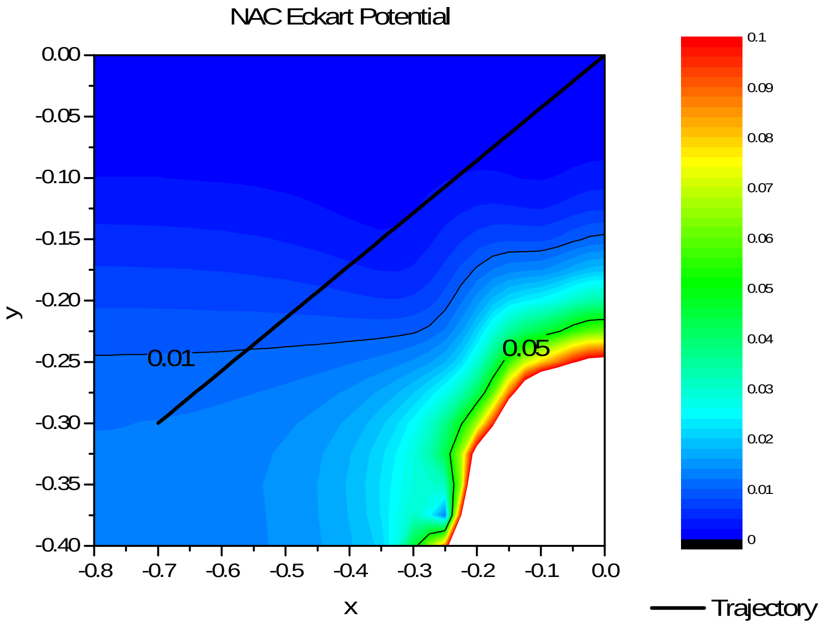

Numerically extended Eckart potential using FD technique. The path of the constant velocity rectilinear trajectory discussed in chapter 4 is shown by the thick black line, while contours of 1% and 5% relative error are shown. Note the pole near *z* ~ -0.35i, where the function is no longer analytic.

Figure 51: NAC of Gaussian Potential

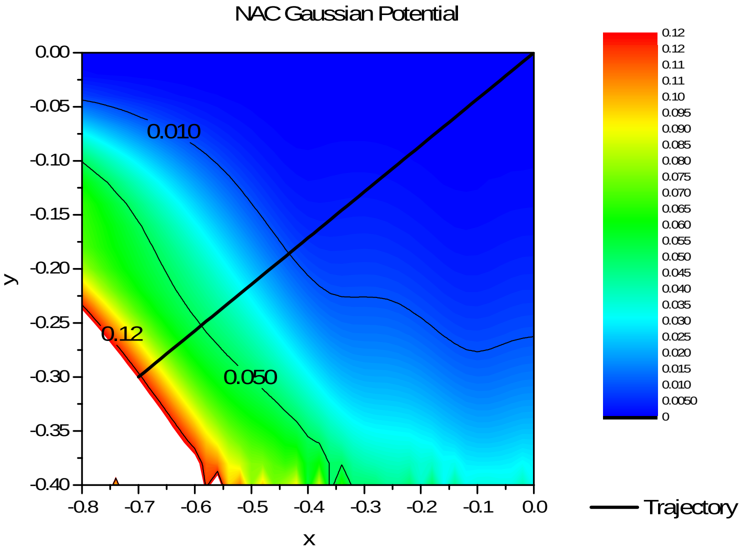

Numerically extended Gaussian potential using FD technique. The path of the constant velocity rectilinear trajectory discussed in chapter 4 is shown by the thick black line, while contours of 1%, 5% and 12% relative error are shown. The essential singularity in this function is found at $z = \pm\infty$.

It was found that the quickest and easiest way to obtain the derivatives of the numerically extended potentials was to apply the appropriate difference operator to obtain the numerical derivative of the real-valued potential. For example, in order to obtain the third derivative of the numerically extended Eckart potential, an eighth order finite difference scheme was employed to find the third derivative of real-valued data points. This was then extended into the complex plane via the Finite Difference method. Figure 52 shows the error in this numerically extended potential, with respect to the exact analytic extension, with error contours shown at 1% and 5%. Note that the accuracy of the numerically extended potential in the region around the node at z = -0.35i has gotten worse when compared to Figure 50. Again, the ALECVDPM(n) trajectory path is shown and it is noted that this trajectory will remain in regions of the numerically extended potential which are quite accurate.

Figure 53 shows the seventh derivative of the numerically extended Eckart potential, completed via the same methods and parameters discussed above. The seventh derivative is shown for this case, as in chapter 4 it was seen that ALECVDPM(7) gave very good barrier transmission probabilities with this starting condition, and it is the highest level of approximation needed. Note that the trajectory skirts very inaccurate regions of the potential, but there are two additional features which require noting. First, the accuracy of the region around the node has gotten worse, as expected. Secondly, the accuracy of the numerically extended potential is seen to be very inaccurate at the edge of the continuation, from y = -0.35 to -0.4. This is fully accounted for by the error analysis presented by Gray and Kaplan. As one takes higher order numerical derivatives of the given data on the real axis, error is being introduced into what was originally exact data. This error is magnified by the Finite Difference continuation (which is only 3rd order accurate overall), leading to numerical breakdown at larger values of y. To mitigate this effect we used very high finite difference formulas in the computation of numerical derivatives.

Figure 52: NAC of Third Derivative of Eckart Potential

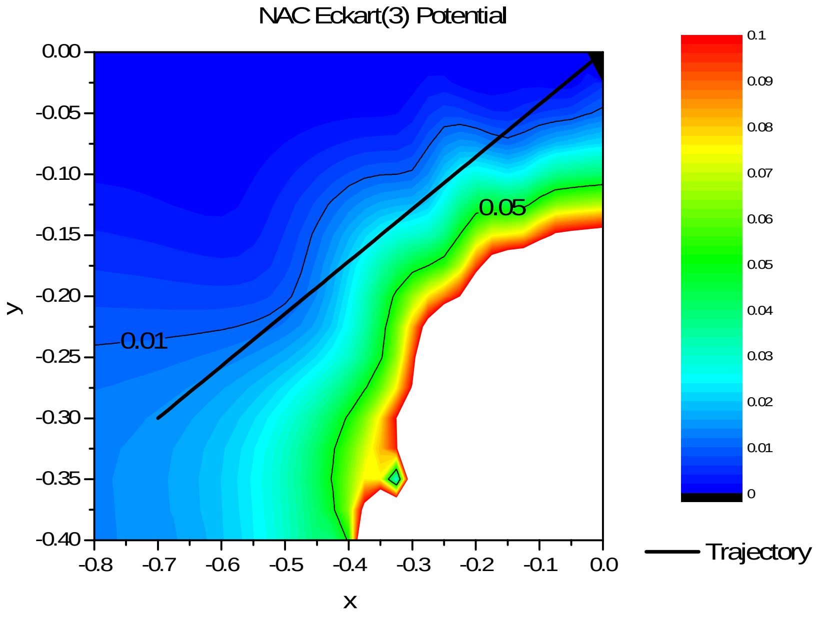

Numerically extended third spatial derivative of the Eckart potential using (8th order numerical derivatives) FD technique. The path of the constant velocity rectilinear trajectory discussed in chapter 4 is shown by the thick black line, while contours of 1% and 5% relative error are shown. Note the larger area of failure for the method in the vicinity of the pole as compared to Figure 49.

Figure 53: NAC of Seventh Derivative of Eckart Potential

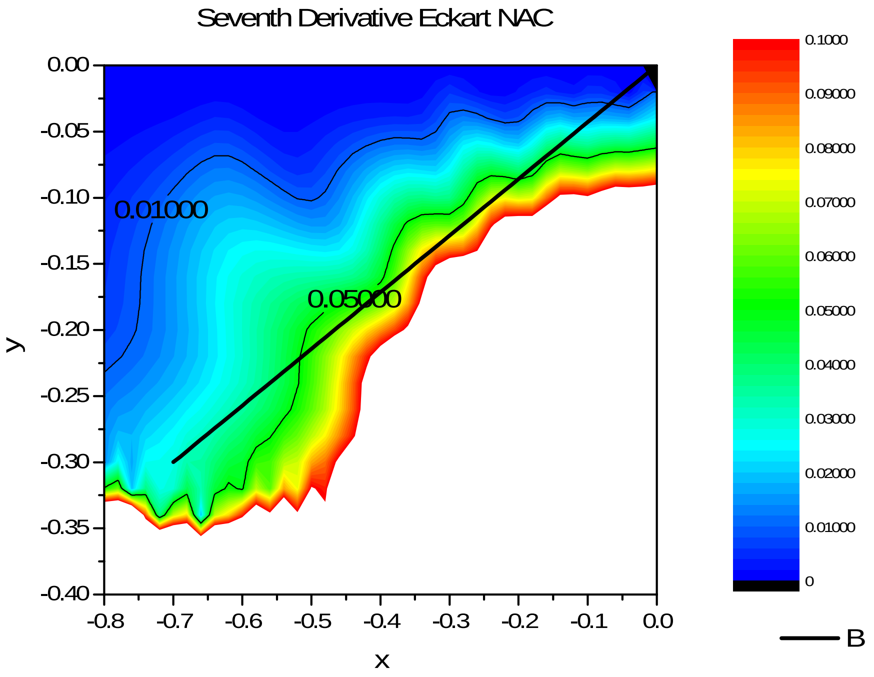

Numerically extended seventh spatial derivative of the Eckart potential (8th order numerical derivatives) using FD technique. The path of the constant velocity rectilinear trajectory discussed in chapter 4 is shown by the thick black line, while contours of 1% and 5% relative error are shown. Note the failure of the method not only near the pole but also at slices $z < -0.35i$. This is due to numerical errors introduced to the FD scheme through the approximation of derivatives with differences.

C. Numerical Analytic Continuation for ALECVDPM(n)

In this section, the use of numerically extended potentials in barrier scattering calculations is explored with the rectilinear constant velocity trajectory models presented in chapter 4. For these barrier scattering problems, discrete points and numerical derivatives sampled from the Metastable Well, Eckart and Gaussian barriers at regular intervals $\Delta x = 0.3$ were each numerically extended into the complex plane using the Cauchy Method as described by Gray and Kaplan. As discussed in their paper, the Cauchy Method is numerically more stable than the Finite Difference Method, though it is a less accurate method (2nd order overall). Here, too, this method was selected for these studies for its better numerical stability. A regular grid from x = -0.8 to 0. and y = -0.4 to 0. with $\Delta x = \Delta y = 0.3$ was initialized where each point in the grid contained the coordinate z and the n derivatives of the potential necessary for ALECVDPM(n). Each of these potential derivatives was checked for acceptable accuracy. An important issue in the implementation of this method is potential surface sampling. We chose a very simple method that worked very well. A simple average of the potential derivative values of the four closest grid points to the current position of the trajectory was taken. This sampling was done at each time step update and only lengthened computational time by 2 minutes.

Figure 54 shows the transmission probabilities for the metastable well problem for exact PSM (pink curve), ALECVDPM(3) with analytically derived potentials (blue squares) and complex extended potentials (green circles). Because the metastable potential is polynomic, nodes will only appear at $z = \pm \infty$. The numeric extension of this potential is very accurate relative to the analytic potential. The results are very good; the

Figure 54: ALECVDPM(n) Trajectories with NAC Metastable Well

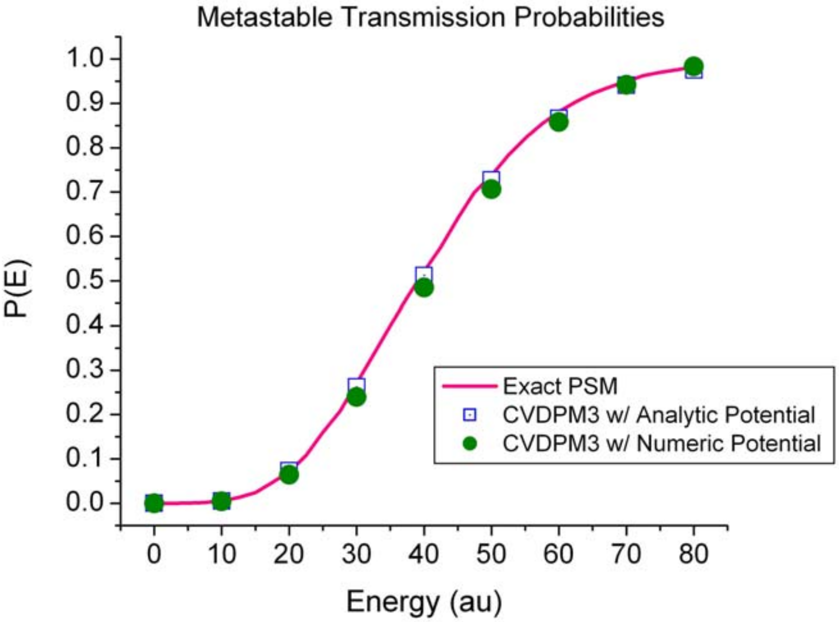

Integrated Flux for metastable well for the exact PSM (solid pink line), ALECVDPM(3) trajectories with analytic potential (blue squares), and ALECVDPM(3) trajectories with a numerical potential (Cauchy extension, green circles). These trajectories follow the path shown in Figure 50.

Figure 55: ALECVDPM(n) Trajectories with NAC Eckart Potential

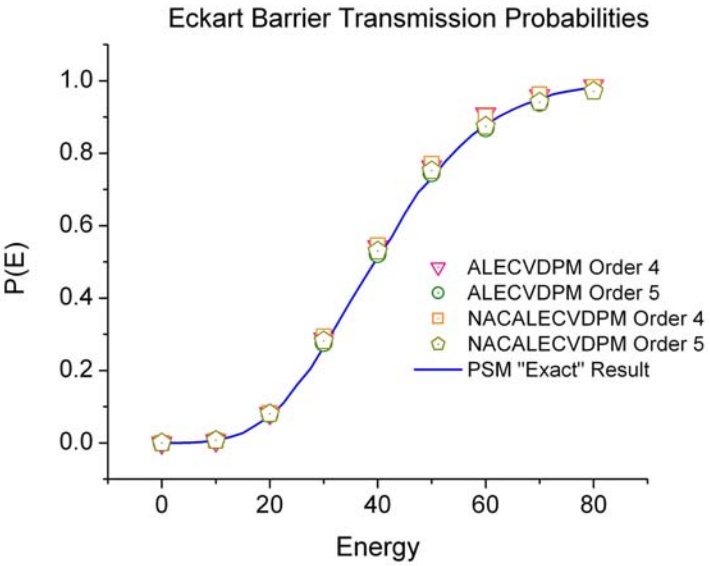

Integrated Flux for Eckart barrier transmission for the exact PSM (solid blue line), ALECVDPM(4) (pink triangles) and ALECVDPM(5) (green circles) trajectories with analytic potential and ALECVDPM(4) (orange squares) and ALECVDPM(5) (gold circles) trajectories with a numerical potential (Cauchy extension). These trajectories follow the path shown in Figure 50.

Figure 56: ALECVDPM(n) Trajectories with NAC Gaussian Potential

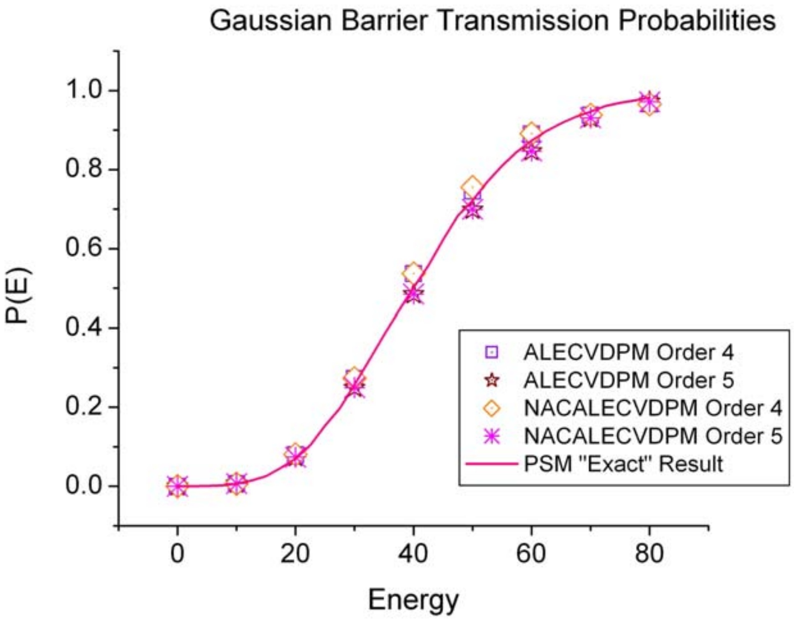

Integrated Flux for Gaussian barrier transmission for the exact PSM (solid pink line), ALECVDPM(4) (lavender squares) and ALECVDPM(5) (purple stars) trajectories with analytic potential and ALECVDPM(4) (orange circles) and ALECVDPM(5) (fuchsia stars) trajectories with a numerical potential (Cauchy extension). These trajectories follow the path shown in Figure 50.

results obtained using the numerically extended potential slightly underestimate the transmission probabilities for E = 30, 40, 50, and 60 a.u., but otherwise the results are good.

Figure 55 shows the results for the Eckart barrier scattering problem with exact PSM (solid blue line), ALECVDPM(4) (pink triangles) and ALECVDPM(5) (green circles) trajectories with analytic potential derivatives and ALECVDPM(4) (orange squares) and ALECVDPM(5) (gold circles) trajectories with numerical potential derivatives. The results are again seen to be very good. Figure 56 shows similar results for the Gaussian barrier scattering problem with exact PSM (solid pink line), ALECVDPM(4) (lavender squares) and ALECVDPM(5) (purple stars) trajectories with analytic potential derivatives and ALECVDPM(4) (orange circles) and ALECVDPM(5) (fuchsia stars) trajectories with a numerical potential derivatives. In both these cases ALECVDPM(4) slightly overestimates the transmission probability, while ALECVDPM(5) is nearly exact. Note, however, that ALECVDPM(4) for both analytic and numerical potential derivatives *both* overestimate the transmission probability while ALECVDPM(5) for both analytic and numerical potential derivatives both give excellent probabilities (though the results slightly underestimate the exact result).

D. NAC for Quantum Potential

These numerical extension methods can be applied to reconstruct the complex quantum potential for barrier reflection problems. In Bohmian Mechanics, nodes in the wave packet correspond to very large negative values of the quantum potential, as shown

Figure 57: Reflected Wave Packet from Eckart Barrier, with Nodes

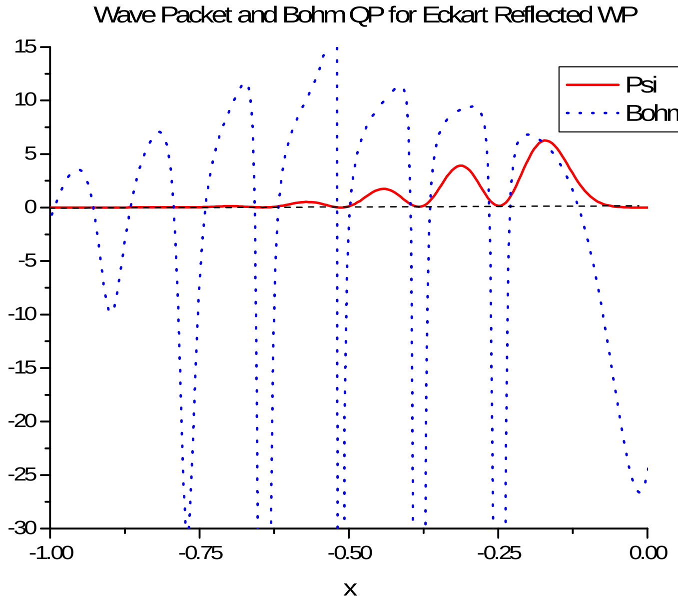

Reflected wave packet density from Eckart Barrier scattering t_a = 0.9 au (solid red line) and associated (real) Bohmian Quantum Potential (dashed blue curve). Note how the QP tends to very low values at regions where nodes develop in the wave packet.

Figure 58: Bohm and Complex QP for Eckart Barrier Reflection

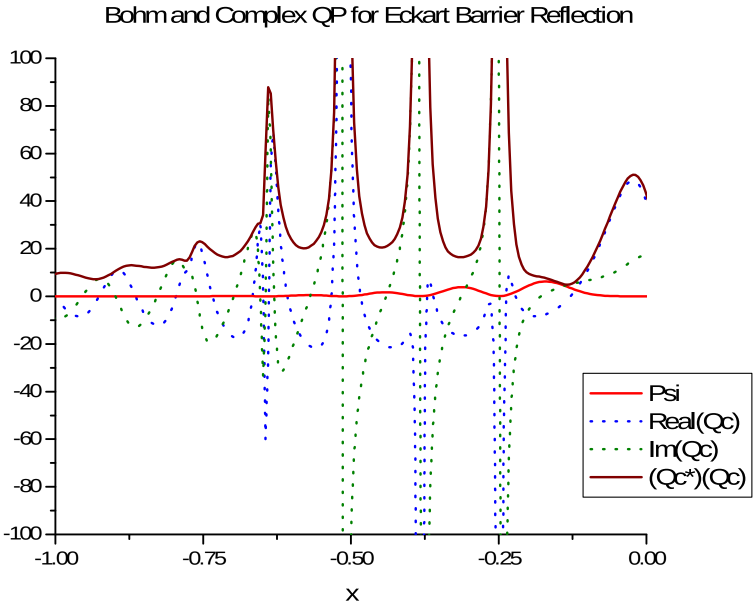

Reflected wave packet density from Eckart Barrier scattering t_a = 0.9 au (solid red line) and associated Real part (dashed blue line), Imaginary part (dashed green line), and absolute value (solid brown line) of the Complex Quantum Potential (dashed blue curve).

in Figure 57. In this example, the pseudo-spectral method is used to compute the reflected wave packet in the Eckart barrier scattering problem for the time t = 0.9 a.u. The Bohmian quantum potential can be computed via equation (1.6). Figure 58 shows the real, imaginary and absolute value of the complex quantum potential (on the real axis) for the same problem. The complex quantum potential has some interesting features. On the real axis, the imaginary portion of the complex potential can be seen to behave like a tangent function, as seen between x = -0.5 to -0.325. The absolute value of the complex potential is similar in magnitude to the Bohmian quantum potential, but opposite in sign.

From the values of the Bohmian quantum potential (via equation (5.6), where $\rho(x,t) = |\psi(x,t)|^2$) and the real and imaginary values of the complex quantum potential on the real axis (via equation (5.7)), one can employ the Cauchy Method to extend these potentials into the complex plane.

$$Q_B(x,t) = -\frac{\hbar^2}{2m}\left[\frac{\rho''(x,t)}{2\rho(x,t)} - \left(\frac{\rho'(x,t)}{2\rho(x,t)}\right)^2\right] \tag{5.6}$$

$$Q_C(x,t) = \frac{\hbar^2}{2m}\left(\frac{\psi''(x,t)}{\psi(x,t)} - \left(\frac{\psi'(x,t)}{\psi(x,t)}\right)^2\right) \tag{5.7}$$

Figures 59, 60, 61, and 62 show the real part of the Bohmian QP, the imaginary part of the Bohmian QP, the real part of the complex QP, and the imaginary part of the complex QP respectively. The numerical extensions show that the potentials are similar in magnitude (contrary to the claims by Tannor and co-workers), albeit opposite in sign.

Figure 59: Real Part of the Bohmian Quantum Potential

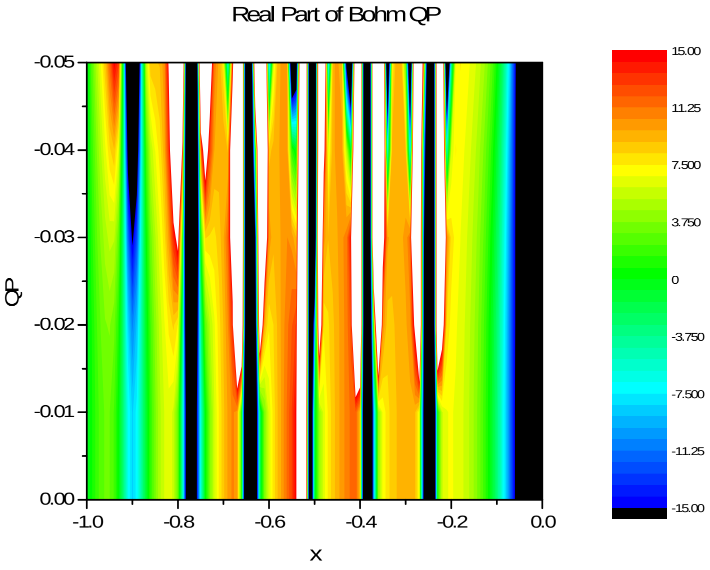

Real Part of the Numerical Analytic Extension (Cauchy method) of the Bohmian Quantum Potential for the example shown in Figs. 57 and 58.

Figure 60: Imaginary Part of the Bohmian Quantum Potential

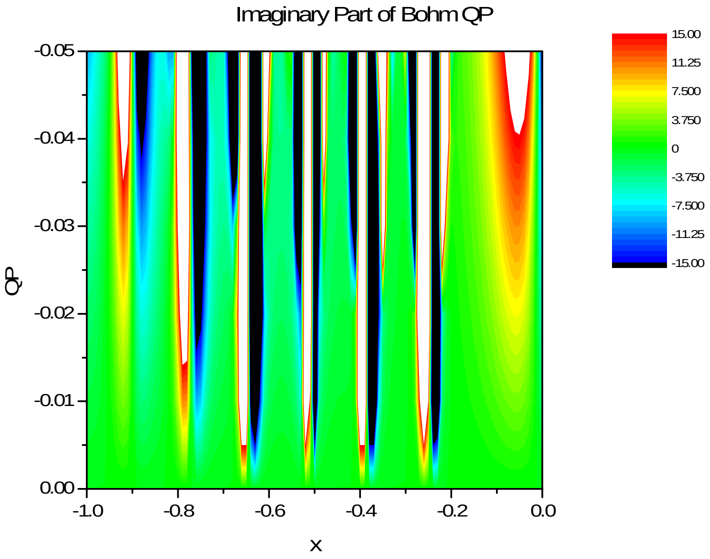

Imaginary Part of the Numerical Analytic Extension (Cauchy method) of the Bohmian Quantum Potential for the example shown in Figs. 57 and 58.

Figure 61: Real Part of the Complex Quantum Potential

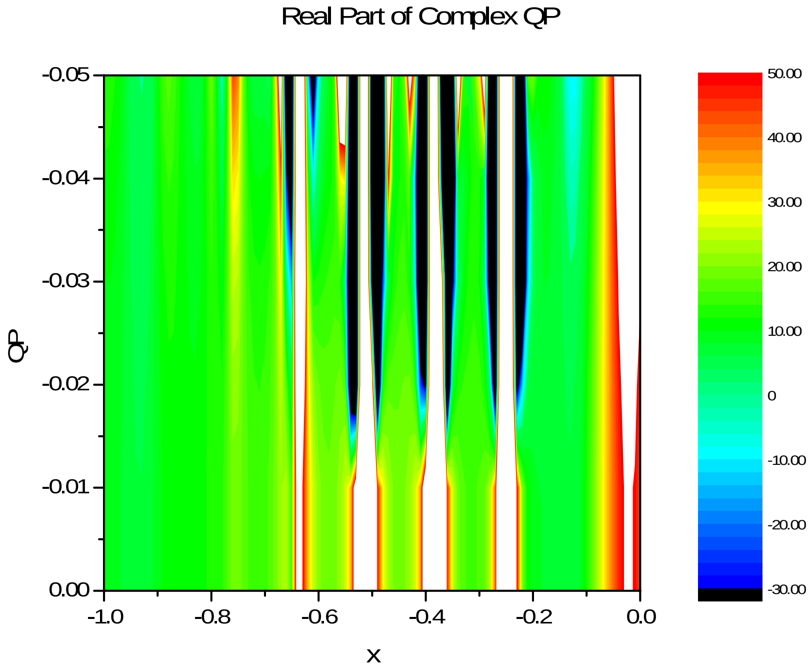

Real Part of the Numerical Analytic Extension (Cauchy method) of the Complex Quantum Potential for the example shown in Figs. 57 and 58.

Figure 62: Imaginary Part of the Complex Quantum Potential

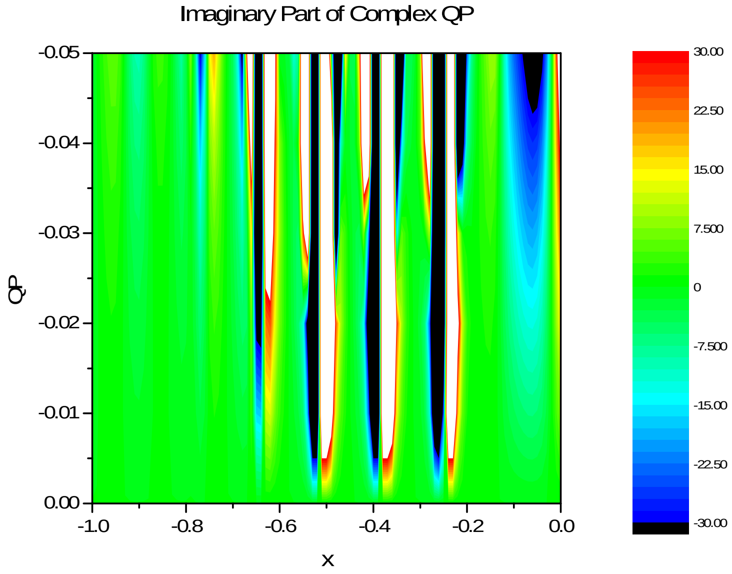

Imaginary Part of the Numerical Analytic Extension (Cauchy method) of the Complex Quantum Potential for the example shown in Figs. 57 and 58.

The figures presented above show that there are regions in the quantum potential that take on extreme values (especially on the real axis), but out in the complex plane there are regions where the complex quantum potential is equal to 0. Lagrangian trajectories travel at a velocity that is proportional to the gradient of the action field. We hypothesized that perhaps these Lagrangian trajectories travel in these regions of low quantum potential in the complex plane (and are not subject to the large quantum force on the real axis). In order to demonstrate this, we located a few reflected trajectories in the Eckart barrier scattering problem presented above. In Figures 63 and 64 five Lagrangian trajectories are shown (pink triangles) for both the real and imaginary parts of the complex quantum potential at t = 0.8 a.u (for arrival time t_a = 1.5 a.u.). The location of these stable trajectories seem to coincide with regions of low quantum potential, at least for this time.

Figures 65 and 66 show the real and imaginary parts of the complex quantum potential for the same problem as in Figures 63 and 64 except for t = 1.0 a.u. The same trend is noted in these plots as seen in the earlier figures, however, one trajectory in Figure 66 is found to be in a region of large quantum potential at x = -0.4. There remains much work to be done in this area, as other potentials need to be explored as well as other times in the evolution of the wave packet. Tentatively, however, it does not appear that the complex quantum potential is a *not* a smooth, low-magnitude potential (as compared to the classical complex potential) but is very complex and contains regions large in magnitude. It also does not seem to be dissimilar to the Bohmian quantum potential.

However, it may be that Lagrangian complex quantum trajectories travel in regions of low quantum potential off the real axis.

Figure 63: Real Part QP w/ Lagrangian Trajectories at t = 0.8 au

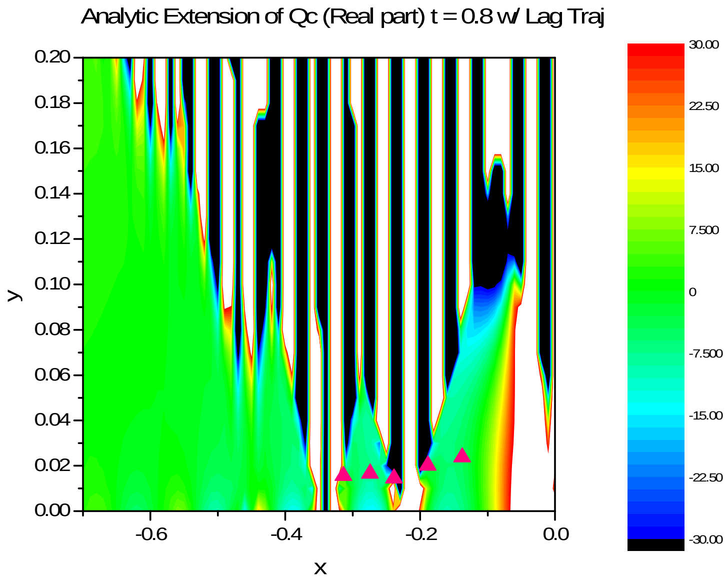

Real Part of the Numerical Analytic Extension (Cauchy method) of the Complex Quantum Potential for Eckart barrier reflection at t_a = 0.8 au. Some Lagrangian Trajectories for this process are shown as pink triangles.

Figure 64: Imaginary Part QP w/ Lagrangian Trajectories at t = 0.8 au

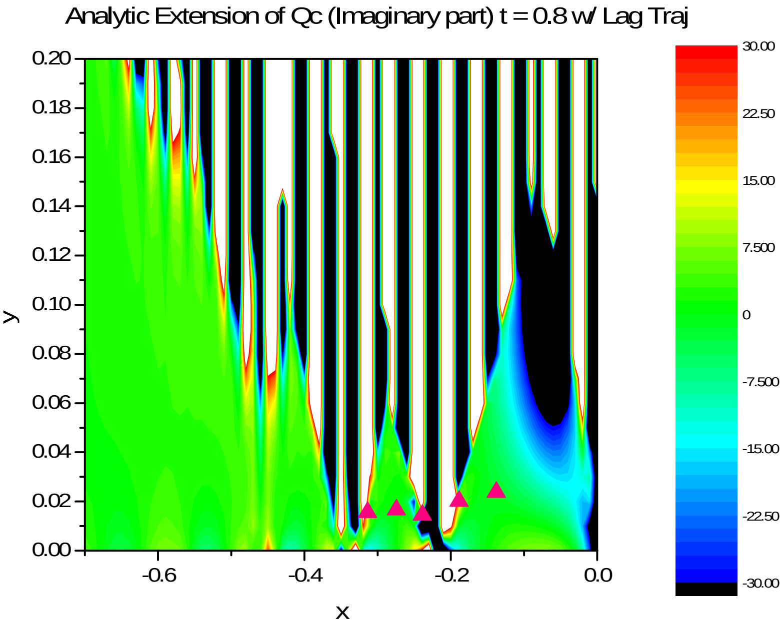

Imaginary Part of the Numerical Analytic Extension (Cauchy method) of the Complex Quantum Potential for Eckart barrier reflection at $t_a = 0.8$ au. Some Lagrangian Trajectories for this process are shown as pink triangles.

Figure 65: Real Part QP w/ Lagrangian Trajectories at t = 1.0 au

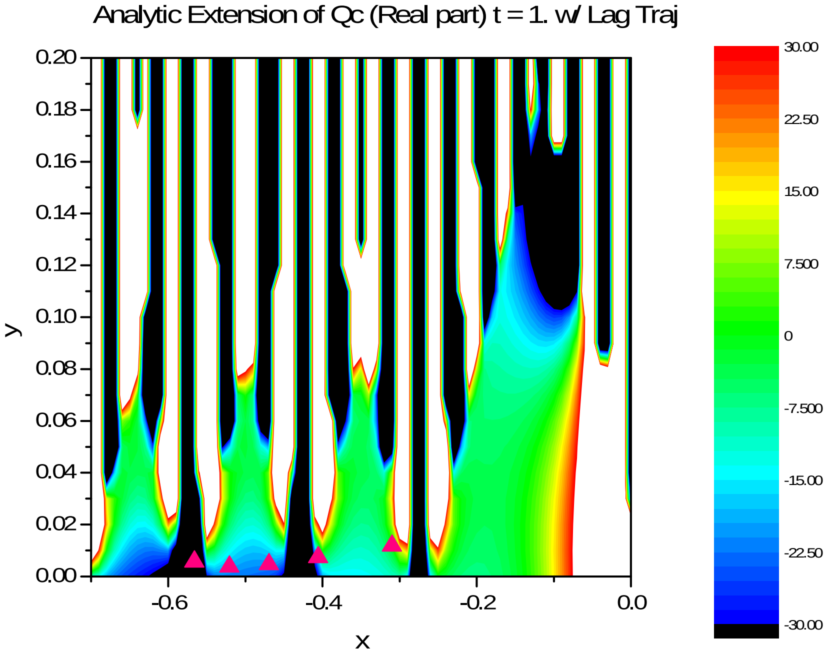

Real Part of the Numerical Analytic Extension (Cauchy method) of the Complex Quantum Potential for Eckart barrier reflection at t_a = 1.0 au. Some Lagrangian Trajectories for this process are shown as pink triangles.

Figure 66: Imaginary Part QP w/ Lagrangian Trajectories at t = 1.0 au

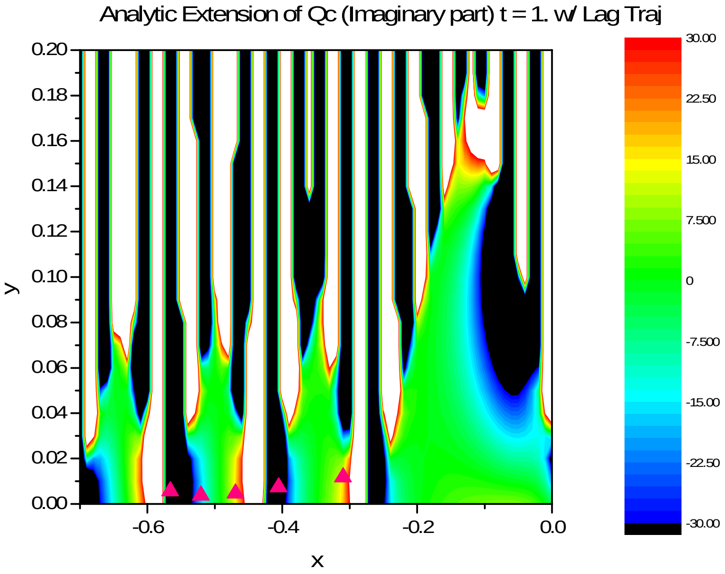

Imaginary Part of the Numerical Analytic Extension (Cauchy method) of the Complex Quantum Potential for Eckart barrier reflection at t_a = 1.0 au. Some Lagrangian Trajectories for this process are shown as pink triangles.

II. Future Directions and Conclusions

A. Isochrone Branches and Reflected Wave Packets

Recent work by David and Wyatt[81] has revealed that the isochrone isn't just a single curve in the complex plane (for a one-dimensional problem) but a series of branches for reflection. Goldfarb and co-workers[79] have recently introduced the idea that complex quantum trajectory may in fact *cross* in space-time, unlike their Bohmian counterparts, which are forbidden to cross. This has led to an interesting development in which reflected wave packets are reconstructed from data that arrive on the real-axis at the same arrival time yet launch from two or more *distinct* isochrones through a simple linear combination of the actions along each of the trajectories. The nodes in the evolving wave packet are reconstructed through this linear combination. Though no definitive algorithm has been provided which can reproduce the reflected wave packet with any given order of CVDPM(n), recent results have indicated that for low orders of DPM very accurate reflected wave packets can be obtained for thin barrier scattering problems.

Future directions in this area include understanding how to reconstruct the wave packet from different isochrone branches and different orders of CVDPM(n). Also, what role do the different isochrone branches play and how do they behave as the order of CVDPM(n) is increased? The introduction of ALECVDPM(n) methods to barrier reflection also presents an interesting set of problems. Since only one initial point is selected, how could one expect to recover wave packet nodes with only one trajectory when clearly Goldfarb's work shows a linear combination of two or more is needed to accurately predict the reflection probability.

B. Future Directions

Further studies are in progress concerning the behavior of CVDPM(n) trajectories in thick versus thin barrier scattering problems, as well as more detailed analysis of isochrones[81]. In particular, it is not known why isochrones exhibit branching, or even what algorithm should be employed in creating linear combinations of wave packets. The idea of trajectory crossing (which is forbidden in Bohmian Mechanics) is an enticing avenue of exploration. Further analyses into the behavior of complex quantum trajectories (such as analysis of forces both quantum and classical) have yet to be completed.

Anticipated extensions of CVDPM(n) include collinear reactive scattering and extension of Wigner trajectories[25] to barrier scattering problems in complex phase space, as well as further generalization of the method to make it applicable to a wider range of barrier scattering (transmission and reflection) problems. It is hoped that further examination of the behavior of complex quantum trajectories will lead to robust and accurate methods for quickly computing transmission probabilities in quantum mechanical barrier scattering problems.

Future work on the ALECVDPM(n) includes extension to the two-dimensional problems presented in chapter 3 (currently underway), analysis and improvement of the numerics, and further studies on different types of potential energy surfaces. Future work on Numerical Analytic Continuation includes the use of Padè approximant[101,102] in generating complex extensions of functions, further analysis of the complex quantum potential in barrier reflection, and eventually to collinear scattering as the two-dimensional ALECVDPM(n) and Numerical Analytic Continuation projects converge.

C. Conclusions

In this dissertation CVDPM(n) is analyzed for potential benefits over RVDPM(n) in barrier scattering transmission problems. Excellent results are obtained for low orders of DPM in the Eckart and Gaussian barrier scattering problems[26,75,77] when the trajectories are moved off the real axis. The concept of an *isochrone* is introduced and analyzed. In order to explore problems of interest to chemical physicists, CVDPM(n) was extended to two-dimensional barrier scattering problems[75] with one translational (Eckart or Gaussian) and one vibrational degree of freedom. Again, excellent transmission probabilities were obtained for low orders of DPM. A model for two dimensional isochrones is presented.

In order to address the isochrone problem, ALECVDPM(n) is introduced. Arbitrary Lagrangian-Eulerian methods[77] allow complete control over trajectory position, so features such as nodes can be avoided in the propagation. ALECVDPM(n) trajectories are shown to give excellent transmission probabilities in the Metastable Well, Eckart and Gaussian barrier scattering problems, whether the trajectory initiates in the complex plane or on the real axis. In order to address another weakness in complex quantum trajectory methods, numerical analytic continuation techniques are introduced to extend discrete real-valued potentials into the complex plane. ALECVDPM(n) trajectories are shown to reproduce transmission probabilities excellently with numerically extended potential derivatives as well as the analytic derivatives.

These numerical extension techniques have also been used to explore further aspects of CVDPM(n). For example, the complex quantum potential can be reconstructed from the density on the real axis (as obtained from PSM calculations). It is hoped that examination of the reflected wave packet (and its associated nodes) will yield insight into the isochrone branch problem as well as to why complex quantum trajectory methods yield better results for both barrier transmission and reflection problems at lower orders of approximation than their real-valued counterparts. Further studies include extension of the ALECVDPM(n) method to two-dimensional problems, collinear reactive scattering, or perhaps even to thermal rate constants.

Appendix A: Correspondence Between RVDPM(n) and CVDPM(n)

In this appendix, correspondence between the equations of motion for RVDPM(n) and CVDPM(n) trajectories will be explored. The guiding principle is that, on the real axis, the equations for CVDPM(n) should be identical to the equations provided by RVDPM(n). Equations (2.1) and (2.25) describe the same wave function on the real axis, hence, the arguments in the exponents should be equal,

$$C(x,t)+\frac{i}{\hbar}S(x,t)=\frac{i}{h}A(x,t). \tag{A.1}$$

The complex action *A(z,t)* can be decomposed into real and imaginary parts,

$$A(z,t)=F(z,t)+iG(z,t). \tag{A.2}$$

Substituting equation (A.2) into equation (A.1) yields the following equations relating the real-valued *C(x,t)* and *S(x,t)* functions to their CVDPM(n) counterparts on the real axis:

$$F(x,t)=S(x,t), \tag{A.3}$$

and

$$G(x,t)=-\hbar C(x,t). \tag{A.4}$$

Equations (A.3) and (A.4) are worth noting. They show that real component of the complex-valued *A(z,t)* can be identified with the *S(x,t)* function from RVDPM(n). The imaginary component of *A(z,t)* is seen to be proportional to the *C*-amplitude in RVDPM(n). Note, however, that these relationships are valid only on the real axis.

Substituting equation (A.2) into equation (2.26) and decomposing the analytically-extended potential *U* into real and imaginary parts $U(z) = U_R(z) + iU_I(z)$, where U_R, U_I are real-valued functions, gives

$$F_t + iG_t = -U_R - \frac{1}{2m}\left(F_1^2 + 2iF_1G_1 - G_1^2\right) + \frac{i\hbar}{2m}\left(F_2 + iG_2\right) - iU_I, \tag{A.5}$$

where all derivatives are taken with respect to the complex coordinate *z*. Separating equation (A.5) into real and imaginary parts and substituting equations (A.3) and (A.4) yields two coupled equations,

$$\frac{\partial F(z,t)}{\partial t} = -\frac{1}{2m}F_1^2 - U_R - \frac{\hbar}{2m}G_2 + \frac{1}{2m}G_1^2, \tag{A.6}$$

and

$$\frac{\partial G(z,t)}{\partial t} = -\frac{1}{2m}\left[-\hbar F_2 + 2F_1G_1\right] - U_I. \tag{A.7}$$

These equations can be transformed into the Lagrangian frame through the use of equation (2.6). These transformed equations become

$$\frac{dF(z,t)}{dt} = \frac{1}{2m}F_1^2 - U_R - \frac{\hbar}{2m}G_2 + \frac{1}{2m}G_1^2, \tag{A.8}$$

and

$$\frac{dG(z,t)}{dt} = \frac{\hbar}{2m}F_2 - U_I. \tag{A.9}$$

In order to make progress, the behavior of equations (A.6) through (A.9) on the real axis must be examined. On the real axis, $U_I = 0$, and U_R will be equal to *V*, the real-valued potential. Employing equations (A.3) and (A.4) in equations (A.6) through (A.9) will generate the appropriate equations on the real axis. This is seen to make the Eulerian equations for *S*, equations (A.6) and (2.2), equivalent. Likewise, equations (A.7) and (2.4) will also be equal. The Lagrangian equations (A.8) and (A.9) are also shown to yield the RVDPM(n) equations on the real axis.

A similar analysis can be carried through for the first two orders of CVDPM(n). Eulerian equations for S_1 and C_1 can be derived from the CVDPM(1) equation, equation (2.30), in the same manner as outlined above. Again, two coupled equations are obtained, which have the form

$$\frac{\partial F_1}{\partial t} = -\frac{1}{m} F_1 F_2 - U_{R,1} - \frac{\hbar}{2m} G_3 + \frac{1}{m} G_1 G_2, \tag{A.10}$$

and

$$\frac{\partial G_1}{\partial t} = -\frac{1}{2m}\left[-\hbar F_3 + 2F_2 G_1 + 2F_1 G_2\right] - U_{I,1}. \tag{A.11}$$

Lagrangian versions of eqs (A.10) and (A.11) are

$$\frac{dF_1}{dt} = -U_{R,1} - \frac{\hbar}{2m} G_3 + \frac{1}{m} G_1 G_2, \tag{A.12}$$

and

$$\frac{dG_1}{dt} = -\frac{1}{2m}\left[-\hbar F_3 + 2F_2 G_1\right] - U_{I,1}. \tag{A.13}$$

Evaluating the equations on the real axis generates equations (both Eulerian and Lagrangian) which are equivalent to the RVDPM(2) equations.

An analysis of CVDPM(2) equations shows the same trend repeating, and one can derive Lagrangian equations for any order of CVDPM(n) by using the following equations,

$$\frac{dG_n}{dt} = -\frac{1}{2m}\left[-\hbar F_{2+n} + 2(G_1 F_1)_n\right] + \frac{1}{m} F_n G_{1+n} - U_{I,n}, \tag{A.14}$$

and

$$\frac{dF_n}{dt} = -\frac{1}{2m}\left(F_1^2\right)_n + \frac{1}{2m}\left[-\hbar G_{2+n} + (G_1^2)_n\right] - U_{R,n} + \frac{1}{m}F_1F_{1+n}. \tag{A.15}$$

As for CVDPM(0) and CVDPM(1), the only difference between RVDPM(n) equations and the equations derived from CVDPM(n) is the term of the form $U_{I,\,n}/\hbar$ appearing in the C_n equations and the replacement of V_n by $U_{R,n}$ in the S_n equations. Equations (A.14) and (A.15) reduce to eqs (2.18) and (2.19), respectively on the real axis. Thus, all equations of CVDPM(n) correspond to those of RVDPM(n) on the real axis, as required. ALE equations of motion can be obtained by setting v to any value desired (excepting the Lagrangian velocity).

Bibliography

1. D. Bohm, *Quantum Theory* (Dover, New York, 1989).
2. D. Bohm, Phys. Rev. **85**, 166 (1952).
3. D. Bohm, Phys. Rev. **85**, 180 (1952).
4. E. Madelung, Z. Phys. **40**, 322 (1926).
5. L. de Broglie, J. Physique **8**, 225 (1927).
6. P. Holland, Annals of Physics **315**, 505 (2005).
7. P. Holland, *The quantum theory of motion : an account of the de Broglie-Bohm causal interpretation of quantum mechanics* (Cambridge University Press, Cambridge, England; New York, NY, 1993).
8. R. E. Wyatt, *Quantum Dynamics with Trajectories* (Springer, New York, 2005).
9. J. Z. H. Zhang, *Theory and application of quantum molecular dynamics*. (World Scientific, Singapore ; River Edge, NJ, 1999).
10. D. J. Tannor, *Introduction to quantum mechanics : a time-dependent perspective*. (University Science Books, Sausalito, CA, 2006).
11. C. L. Lopreore and R. E. Wyatt, Phys. Rev. Lett. **82**, 5190 (1999).
12. D. Babyuk and R. E. Wyatt, Chem. Phys. Lett. **400**, 145 (2004).
13. D. Babyuk and R. E. Wyatt, J. Chem. Phys. **121**, 9230 (2004).
14. D. Babyuk and R. E. Wyatt, Phys. Rev. E. **73**, 10 (2006).
15. D. Babyuk and R. E. Wyatt, J. Chem. Phys. **124**, 7 (2006).

16. D. Babyuk and R. E. Wyatt, J. Chem. Phys. **125**, 7 (2006).

17. F. S. Mayor, A. Askar, and H. A. Rabitz, Phys. Rev. Lett. **82**, 5190 (1999).

18. C. J. Trahan, K. Hughes, and R. E. Wyatt, J. Chem. Phys. **118**, 9911 (2003).

19. C. J. Trahan and R. E. Wyatt, J. Chem. Phys. **119**, 7017 (2003).

20. C. J. Trahan and R. E. Wyatt, Chem. Phys. Lett. **385**, 280 (2004).

21. K. H. Hughes and R. E. Wyatt, Journal of Chemical Physics **120** (9), 4089 (2004).

22. K. H. Hughes, J. Chem. Phys. **122**, 11 (2005).

23. E. R. Bittner, J. Chem. Phys. **119**, 1358 (2004).

24. C. J. Trahan, R. E. Wyatt, and B. Poirier, J. Chem. Phys. **122**, 164104 (2005).

25. B. A. Rowland and R. E. Wyatt, Chem. Phys. Lett. **426**, 209 (2006).

26. B. A. Rowland and R. E. Wyatt, J. of Phys. Chem. A **111,** 10234 (2007).

27. D. McQuarrie, *Statistical Mechanics* (Harper and Row, New York, 1976).

28. H. Corben and P. Stehle, *Classical Mechanics* (Dover, New York, 1977).

29. J. E. Moyal, Proc. Cambridge Philos. Soc. **45**, 99 (1949).

30. A. O. Caldeira and A. J. Leggett, Physica A **121**, 587 (1983).

31. H. A. Kramers, Physica (Utretch) **7**, 284 (1940).

32. G. Billing and K. Mikkelsen, *Introduction to Molecular Dynamics and Chemical Kinetics* (John Wiley, Hoboken, NJ, 1996).

33. E. P. Wigner, Phys. Rev. **40**, 749 (1932).

34. E. R. Bittner, J. Chem. Phys. **119**, 1358 (2003).

35. E. Heller, J. Chem. Phys. **62**, 1544 (1975).

36. D. Shalashilin and M. Child, J. Chem. Phys. **113**, 10028 (2000).

37. D. Shalashilin and M. Child, J. Chem. Phys. **114**, 9296 (2001).

38. D. Shalashilin and M. Child, J. Chem. Phys. **115**, 5367 (2001).

39. T. Martinez and M. Ben-Nun, J. Chem. Phys. **100**, 7884 (1996).

40. M. Ben-Nun and T. Martinez, J. Chem. Phys. **108**, 7244 (1998).

41. M. Ben-Nun and T. Martinez, J. Phys. Chem. **112**, 6113 (2000).

42. S. Swada, R. Heater, B. Jackson, and H. Metiu, J. Chem. Phys. **83**, 3009 (1985).

43. B. K. Kendrick, J. Chem. Phys. **119**, 5805 (2003).

44. D. K. Pauler and B. K. Kendrick, J. Chem. Phys. **120**, 603 (2004).

45. D. K. Pauler and B. K. Kendrick, J. Chem. Phys. **121**, 2471 (2004).

46. B. Poirier, J. Chem. Phys. **121**, 4501 (2004).

47. C. Trahan and B. Poirier, J. Chem. Phys. **124**, 14 (2006).

48. C. Trahan and B. Poirier, J. Chem. Phys. **124**, 18 (2006).

49. V. A. Rassolov and S. Garashchuk, J. Chem. Phys. **120**, 6815 (2004).

50. S. Garashchuk and V. A. Rassolov, J. Chem. Phys. **121**, 8711 (2004).

51. V. A. Rassolov and S. Garashchuk, Phys. Rev. A **71**, 10 (2005).

52. T. Takabayasi, Prog. Theor. Phys. **11**, 341 (1954).

53. I. Burghardt and L. S. Cederbaum, J. Chem. Phys. **115**, 10303 (2001).

54. I. Burghardt and L. S. Cederbaum, J. Chem. Phys. **115**, 10312 (2001).

55. I. Burghardt, K. B. Moller, G. Parlant, L. S. Cederbaum, and E. Bittner, Int. J. Quantum Chem. **100**, 1153 (2004).

56. E. C. Kemble, Phys. Rev. **48**, 549 (1935).

57. M. V. Berry and K. E. Mount, Rep. Prog. Phys. **35**, 315 (1972).

58. D. Huber and E. J. Heller, J. Chem. Phys. **87**, 5302 (1987).

59. Y. Goldfarb, I. Degani, and D. J. Tannor, J. Chem. Phys. **125**, 231103 (2006).

60. D. B. Cook, *Probability and Schrödinger's Mechanics* (World Scientific, River Edge, NJ, 2002).

61. M. V. John, Found. Phys. Lett. **15**, 329 (2002).

62. C.-D. Yang, Chaos, Solit. and Fract. **30**, 342 (2006).

63. C.-D. Yang, Chaos, Solit. and Fract. **32**, 312 (2006).

64. C.-D. Yang, Annal. Phys. **319**, 399 (2005).

65. C.-D. Yang, Int. J. Quantum Chem. **106**, 1620 (2006).

66. C.-D. Yang, Chaos, Solit. and Fract. **30**, 41 (2006).

67. C.-D. Yang, Annal. Phys. **319**, 444 (2005).

68. C.-D. Yang, Chaos, Solit. and Fract. **30**, 342 (2006).

69. C.-D. Yang, Chaos, Solit. and Fract. **32**, 312 (2007).

70. C. C. Chou and R. E. Wyatt, J. Chem. Phys. **125**, 10 (2006).

71. C. C. Chou and R. E. Wyatt, Phys. Rev. E **74**, 9, 2006.

72. C. C. Chou and R. E. Wyatt, Int. J. Quantum Chem, submitted.

73. M. Boiron and M. Lombardi, J. Chem. Phys. **108**, 3431 (1998).

74. C. C. Chou and R. E. Wyatt, Phys. Rev. A **76**, Article No. 012115 (2007).

75. R. E. Wyatt and B. A. Rowland, J. Chem. Phys. **127,** 044103 (2007).

76. Y. Goldfarb, I. Degani and D. J. Tannor, *arXiv.org*, arXiv: 0705.2132v1 (2007).

77. B. A. Rowland and R. E. Wyatt, J. Chem. Phys., in press (2007).

78. Y. Goldfarb, J. Schiff and D. J. Tannor, J. Phys. Chem. A **111**, 10416 (2007).

79. Y. Goldfarb and D. J. Tannor, *arXiv.org*, arXiv: 0706.3507v1 (2007).

80. Y. Goldfarb, J. Schiff and D. J. Tannor, *arXiv.org*, arXiv: 0707.0117v1 (2007).

81. J. K. David and R. E. Wyatt, J. Chem. Phys., in press (2007).

82. S. Garashchuk and V. A. Rassolov, Chem. Phys. Lett. **364**, 562 (2002).

83. D. Huber, E. J. Heller and R. G. Littlejohn, J. Chem. Phys. **89**, 2003 (1988).

84. M. A. M. de Aguiar, M. Baranger, L. Jaubert, F. Parisio and A. D. Ribeiro, J. Phys. A—Math and Gen. **38**, 4645 (2005).

85. G. B. Arfken and H. J. Weber, *Mathematical Methods for Physicists* (Harcourt/Academic Press, San Digeo, 2001).

86. Y. K. Kwok, *Applied Complex Variables for Scientists and Engineers* (University Press, Cambridge, England; New York, 2002).

87. M. H. Holmes, *Introduction to Numerical Methods in Differential Equations* (Springer, New York, 2007).

88. W. H. Hundsdorfer, and J. G. Verwer, *Numerical Solution of Time-Dependent Advection-Diffusion-Reaction Equations* (Springer, Berlin; New York, 2003).

89. L. F. Shampine and M. E. Hosea, Appl. Numer. Math **20**, 21 (1996).

90. J. H. Van Vleck, Proc. Natl. Acad. Sci. **14**, 178 (1928).

91. C. W. McCurdy and W. H. Miller, J. Chem. Phys. **73**, 3191 (1980).

92. W. H. Press, S. A. Teukolsky, W. T. Vetterling, and B. P. Flannery, *Numerical Recipes* (Cambridge University Press, New York, 1992).

93. www.caa.co.uk/docs/5/ergdocs/heathrowisochrone_note.pdf, accessed June 28, 2007.

94. W. H. Miller, Journal of Chemical Physics **53**, 1949, 3578 (1970).

95. J. U. Brackbill and W. E. Pracht, J. Comp. Phys. **13**, 455 (1973).

96. C. W. Hirt, A. A. Amsden, and J. L. Cook, J. Comp. Phys. **14**, 227 (1974).

97. K. Hass, B. Velický and H. Ehrenreich, Phys. Rev. B **29**, 3697 (1983).

98. H. Eschrig, R. Richter and B. Velický, J. Phys. C.: Solid State Phys. **19**, 7173 (1986).

99. L. Gray and T. Kaplan, J. Phys. A.: Math. Gen. **19**, 1555 (1986).

100. V. Natoll, M. Cohen and B. Fornberg, J. Comp. Phys. **126**, 99 (1996).

101. W. Miller and T. George, J. Chem. Phys. **56**, 5668 (1972).

102. G. A. Baker and J. L. Gammel (eds.), *The Padè Approximant in Theoretical Physics* (Academic, New York, 1970).

Vita

Bradley Allen Rowland was born in Gainesville, Texas on September 18, 1979, the son of Jimmy Kirk Rowland and Peggy Lynn Conner Rowland. After completing his work at Callisburg High School, Gainesville, Texas, in 1998 he entered Texas A&M University in College Station, Texas. He received two Bachelor of Science degrees from Texas A&M University in May 2002. In January 2003 he entered the Graduate School of The University of Texas at Austin. He received a Master of Arts degree from the University of Texas at Austin in August 2005.

Permanent Address: 164 CR 143, Whitesboro, Texas 76273

This dissertation was typed by the author.